

# Ultralow-Loss Silica Resonators and Waveguides on a Silicon Chip

Thesis by  
Tong Chen

In Partial Fulfillment of the Requirements  
for the Degree of  
Doctor of Philosophy



California Institute of Technology  
Pasadena, California

2013  
(Defended February 7, 2013)

© 2013

Tong Chen

All Rights Reserved

For my family, who offered me unconditional love and support throughout the course of my life.

# Acknowledgements

Looking back at my years at Caltech, I have immensely enjoyed this most challenging and rewarding experience here. This institute offered me great freedom and a creative environment to explore not only the outside world but also my own interests. I would like to extend my gratitude to all those who made my life at campus rewarding and enjoyable.

Firstly, I would like to sincerely thank my advisor, Professor Kerry Vahala, for giving me a wonderful research opportunity and supporting me throughout my graduate studies at Caltech. In spite of his busy schedule, Kerry was always flexible for individual meetings and offering insightful advice and zealous guidance. His brilliance, creativity, optimism, and enthusiasm provided the perfect role model for me. His visionary research ideas encouraged me to exceed my limitations and achieve goals beyond my ability. In addition to that scientific side, he also offered me invaluable advice in managing my projects and planning my career. Also, he had always had patience for the many, sometimes quite extended, trips to China I took during my dissertation. I cannot think of a way to return the favor, except to strive to become a better researcher.

I am deeply indebted to my former advisors, Professor Qi Ouyang and Professor Chao Tang, for supporting and motivating me to explore and pursue the right path ever since my undergraduate years at Peking University. They exhibited a superb example of dedication, strictness, and generosity, and guided me from the very beginning in my research journey.

It is my great fortune to have the world's most eminent scholars as my thesis and candidacy committee members—Professor Oskar Painter, Professor Harry Atwater, and Professor Keith Schwab. It is a great honor to have such a group of brilliant scientists on my committee. I appreciate their comments and invaluable advice on my research at Caltech.

Many members of the Vahala group, past and present, have helped me tremendously throughout my journey. I acknowledge my intelligent colleagues who taught me, and offered suggestions, or even their time to help me—Dr. Hansuek Lee, Dr. Tao Lu, Dr. Eric

Ostby, Dr. Mani Hossein-Zadeh, Dr. Ivan Grudin, and Dr. Hossein Rokhsari. They are knowledgeable and helpful, and guided me through important steps in my research. I have greatly benefited from the advanced fabrication skills that my colleague Dr. Hansuek Lee taught me. He also made innumerable contributions to the progression of this thesis. I have enjoyed spending time with him due to his enthusiasm, persistence and kindness. Dr. Tao Lu and I spent hours together and generously collaborated on the bio-sensing project. I owe many thanks to Dr. Ivan Grudin, with whom I worked closely on several projects. Ivan impressed me with his unflinching passion for science and incredible skills in experiments. I am very thankful for his advice and mentorship. Special thanks goes to Rosalie Rowe and Cecilia Gamboa, who have been extremely helpful in day-to-day administrative matters.

I have deeply enjoyed having the privilege to spend my five years at this unique institute. A complete list of my friends is not possible, although I would like to thank as many as I can. Many thanks to Dr. Yao Sha, Dr. Jie Cheng, and Dr. Xin Guo for helping me get accustomed to the life here in Pasadena. My graduate school years here would be a lot more difficult without your help. It was a great pleasure to work with Yu Zhao, Bin Zhang, Dr. Xi Zhang, Dr. Wendian Shi, Na Li, Na Hu, and Shuo Han at the Caltech Chinese Association. Dr. Jie Cheng, Dr. Liming Wang, and Xiao Liu explored the world of management consulting with me. Dr. Jinghao Huang shared interest in quantitative finance. Tian Lan, Ruizhe Wang, and Xiaofei Chang shared many laughs, cold pints, and lopsided defeats with me in GSC basketball games. Dinners with Dr. Hongchao Zhou, Maolin Ci, Jingjing Huang, Sinan Zhao, Shiyang Song and, Shijia (Wendy) Chen are always full of fun. There are also many people outside Caltech who explored the beauty of nature with me over the years. I immensely enjoyed the time spent with Dr. Qingtao Chen, Dr. Yi Zhang, Lu Li, Yuchi Che, Wei Qin and many other friends from the University of Southern California in hiking and road trips.

My old friends from Peking University are always my good source of encouragement and inspiration, as well as entertainment. Dr. Su Chen, Jiabin Wang, and Dr. Wenjun Qiu have provided me with update feeds about old friends at Wall Street and interview tips. Dr. Si Li has always been there to listen to my many frustrations with graduate school and has been a welcome reservoir of support and entertainment.

Finally, I give the deepest gratitude to my family for their unconditional support and love. My parents, Zheng Chen and Jingfang Wang, always give me the freedom to chart my

own course and respected all my choices. They have provided the most encouragement and endless devotion throughout my entire life. I am also blessed by my girlfriend Hao Wang, who has enriched my life in every aspect in the last few years. I thank her for all the love and support. We have learned and will continue to grow together and to nurture, support, and encourage each other for our better future. Thanks to her for all the sacrifices she has made for us.

*Tong Chen*

*January, 2013*

*Pasadena, California,*

*The United States of America*

# Abstract

Compared to fiber optic systems, on-chip optical devices provide reasonable optical performance and mechanical stability in a smaller footprint and at a lower cost. Such devices, including resonators and waveguides, have been applied in diverse areas of scientific research, including quantum information, nonlinear optics, cavity optomechanics, telecommunications, biodetection, rotation sensing, high-stability microwave oscillators, and all-optical signal processing. As performance demands on these applications increase, resonators and waveguides with ultralow propagation loss become critical.

In this thesis, we first demonstrate a new resonator with a record Q factor of 875 million for on-chip devices. The fabrication of our device avoids the requirement for a specialized processing step, which in microtoroid resonators has made it difficult to control their size and achieve millimeter- and centimeter-scale diameters. Attaining these sizes is important in applications such as microcombs. The resonators not only set a new benchmark for the Q factor on a chip, but also provide, for the first time, full compatibility of this important device class with conventional semiconductor processing.

Meanwhile, we demonstrate a monolithic waveguide as long as 27 m (39 m optical path length), and featuring broadband loss rate values of  $(0.08 \pm 0.01)$  dB/m measured over 7 m by optical backscattering. Resonator measurements show a further reduction of loss to 0.037 dB/m, close to that of optical fibers when first considered a viable technology. Scaling this waveguide to integrated spans exceeding 250 m and attenuation rates below 0.01 dB/m is discussed. This chip-based waveguide and resonator improve shock resistance, and afford the possibility of integration for system-on-a-chip functionality.

We finally demonstrate a highly sensitive nanoparticle and virus detection method by using a thermal-stabilized reference interferometer in conjunction with an ultrahigh-Q microcavity. Sensitivity is sufficient to resolve shifts caused by binding of individual nanobeads in solution down to a record radius of 12.5 nm, a size approaching that of single protein

molecules. A histogram of wavelength shift versus nanoparticle radius shows that particle size can be inferred from shift maxima.

# Contents

<b>Acknowledgements</b>	<b>iv</b>
<b>Abstract</b>	<b>vii</b>
<b>List of Figures</b>	<b>xiii</b>
<b>List of Tables</b>	<b>xxiii</b>
<b>List of Publications</b>	<b>xxiv</b>
<b>1 Introduction</b>	<b>1</b>
1.1 Optical microresonators . . . . .	1
1.2 Optical waveguides . . . . .	2
1.3 Thesis outline . . . . .	2
<b>2 Optical Microresonators and Their Basis</b>	<b>4</b>
2.1 Whispering-gallery mode . . . . .	4
2.2 Quality factor . . . . .	6
2.2.1 Scanning measurements . . . . .	7
2.2.2 Cavity ring-down measurements . . . . .	8
2.3 Optical loss in optical microresonators . . . . .	10
2.3.1 Intrinsic material loss ( $Q_{mat}$ ) . . . . .	10
2.3.2 Surface scattering loss ( $Q_{ss}$ ) . . . . .	10
2.3.3 Surface absorption loss ( $Q_{sa}$ ) . . . . .	11
2.3.4 Whispering gallery loss ( $Q_{wgm}$ ) . . . . .	12
2.4 Mode volume . . . . .	13
2.5 Tapered fiber coupling . . . . .	13

2.5.1	Tapered fiber fabrication . . . . .	13
2.5.2	Characterization of tapered fiber . . . . .	14
2.5.3	Coupling-of-modes formalism . . . . .	14
2.5.4	Coupling coefficients and $Q_{ext}$ (the coupling quality factor) . . . . .	16
2.6	Summary . . . . .	18
<b>3</b>	<b>Thermal Stress in Silica-on-Silicon Wedge Resonators</b>	<b>19</b>
3.1	Introduction . . . . .	19
3.2	Experimental results . . . . .	20
3.3	Finite element model . . . . .	21
3.4	Analytic model . . . . .	23
3.5	Summary . . . . .	28
<b>4</b>	<b>Chemically Etched Ultrahigh-Q Wedge Resonator</b>	<b>29</b>
4.1	Introduction . . . . .	29
4.2	Device fabrication . . . . .	30
4.3	Device characterization . . . . .	33
4.3.1	Optical Q-factor measurements . . . . .	33
4.3.2	Precise size control of the resonators . . . . .	39
4.3.3	Stimulated Brillouin lasers . . . . .	39
4.4	Discussion . . . . .	42
<b>5</b>	<b>Ultralow-Loss Silica Spiral Waveguide</b>	<b>44</b>
5.1	Introduction . . . . .	44
5.2	Fabrication process and waveguide structure . . . . .	46
5.3	Backscatter characterization of single-spiral delay lines . . . . .	48
5.4	Backscatter characterization of cascaded-spiral delay lines . . . . .	53
5.4.1	27 meter spiral delay lines . . . . .	53
5.4.2	More testing on cascaded-spiral delay lines . . . . .	56
5.4.3	Loss spectrum . . . . .	56
5.5	Loss analysis . . . . .	59
5.5.1	Waveguide loss analysis . . . . .	59
5.5.2	S-bend (hand off) loss analysis . . . . .	62

5.6	Optical buffer demonstration . . . . .	63
5.7	Theory of direct measurements of $n_2$ of the spiral waveguide . . . . .	65
5.7.1	Kerr effect nonlinearity . . . . .	65
5.7.2	Measurements via self-phase modulation (SPM) . . . . .	66
5.7.3	Measurements via four-wave mixing (FWM) . . . . .	69
5.8	Discussion . . . . .	70
<b>6</b>	<b>Low Optical Loss Adiabatic Connections in Waveguides</b>	<b>72</b>
6.1	Introduction . . . . .	72
6.2	Design algorithm . . . . .	74
6.2.1	Overview . . . . .	74
6.2.2	S-bend design . . . . .	77
6.3	Experimental verification . . . . .	81
6.3.1	Spiral waveguide measurements . . . . .	82
6.3.2	Resonators measurements . . . . .	85
6.3.3	Loss analysis . . . . .	86
6.4	Summary . . . . .	86
<b>7</b>	<b>Designs of Ultralow-Loss Spiral Waveguides</b>	<b>88</b>
7.1	Introduction . . . . .	88
7.2	Design principles and implementations of spiral waveguides . . . . .	89
7.2.1	Archimedean spirals . . . . .	89
7.2.2	S-bend connection waveguide . . . . .	93
7.2.3	Tapering of waveguide . . . . .	96
7.2.4	Connection and input/output waveguide . . . . .	99
7.2.5	Buffering patterns . . . . .	100
7.3	Summary . . . . .	102
<b>8</b>	<b>High-Sensitivity Nanoparticle Detection Using Optical Microcavities</b>	<b>103</b>
8.1	Introduction . . . . .	103
8.2	Reactive mechanism wavelength shift . . . . .	104
8.2.1	Perturbation theory . . . . .	104
8.2.2	Estimation of the reactive shift by proteins or virus . . . . .	105

8.3	Experimental results: reactive shift . . . . .	106
8.3.1	Experiment setup . . . . .	106
8.3.2	Polystyrene nanobeads detection . . . . .	108
8.3.3	Influenza A virion detection . . . . .	111
8.4	Thermo-optic effect wavelength shift . . . . .	111
8.4.1	Derivation of thermo-optic wavelength shift . . . . .	111
8.4.2	Estimation of absorption cross section . . . . .	115
8.5	Summary . . . . .	118
<b>Bibliography</b>		<b>119</b>

# List of Figures

2.1	Finite element simulation results of mode intensity profiles in resonators with 7.5 mm diameter, 10 $\mu\text{m}$ oxide thickness, and $21^\circ$ wedge angle . . . . .	6
2.2	The measured optical spectrum of a device featuring a Q factor of 750 million. The black data are concurrent scans from an interferometer used to calibrate the resonant linewidth. The FSR of the Mach-Zehnder interferometer here is 7.75 MHz. . . . .	8
2.3	Ring-down measurement of cavity Q. The intensity decay in time is fit to an exponential decay function. Subfigure (a) and (b) are extracted from (c), which shows the transmission, upon gating-off the laser. . . . .	9
3.1	(a) SEM image of an unbuckled silica disk (500 $\mu\text{m}$ diameter and 2 $\mu\text{m}$ oxide thickness) resonator on a silicon pillar. The undercut is about 55 $\mu\text{m}$ . (b)–(f) Top-view microscope images of resonators (500 $\mu\text{m}$ diameter and 2 $\mu\text{m}$ oxide thickness) with different buckled oxide configurations. The undercuts of these devices are 70 $\mu\text{m}$ , 120 $\mu\text{m}$ , 155 $\mu\text{m}$ , 185 $\mu\text{m}$ , and 225 $\mu\text{m}$ , respectively. (g) Spectral scan for the resonator in panel (a). The measured linewidth corresponds to an optical Q factor of 37 million. The red curve gives a Lorentzian fitting of the experimental transmission and the cyan line shows a sinusoidal fitting of the interferometer output. (h)–(i) Finite element simulation results of resonators (500 $\mu\text{m}$ diameter and 2 $\mu\text{m}$ oxide thickness) showing different buckling configurations. The undercut of these devices matches those in the panels (b)–(f). . . . .	20

3.2	Plot of the order parameter (Eq. (3.1)) versus the change in temperature relative to the growth temperature. A second-order phase transition is apparent at a critical temperature difference ( $\Delta T_c$ ). Above this value, the disk buckles and features a crown pattern with several nodes. On the other hand, the silica layer bends uniformly down when $\Delta T$ is smaller than the critical value. In this FEM simulation, the resonator has diameter $500 \mu\text{m}$ , thickness $2 \mu\text{m}$ , and undercut $70 \mu\text{m}$ . . . . .	22
3.3	An SEM image of top (upper panel) and side (lower panel) view of silica bridge fabricated on a silicon chip. Due to the thermal stress, the bridge bends up. The cantilever has length of $1 \text{ mm}$ and width from $2 \mu\text{m}$ to $12 \mu\text{m}$ . The measured vertical deflection ( $43 \mu\text{m}$ ) agrees with the simulation result ( $46.1 \mu\text{m}$ ). . . . .	24
3.4	The relation between normalized critical temperature difference ( $\Delta\alpha\Delta T b^2/t^2$ ) and parameter $\rho = a/b$ for configurations with different numbers of nodes (see legend) in the silica/silicon system. Insets show examples from experiments of the buckled configurations with $\rho = 0.52$ , 10 nodes, and $\rho = 0.26$ , 6 nodes (See Fig. 3.1). . . . .	26
3.5	The threshold of undercut parameter ( $\xi = 1 - a/b$ ) for buckling. For each thickness, the left side of curve defines a region in which the disk resonators do not buckle. . . . .	28
4.1	The comparisons among current available high-Q factor resonators. . . . .	30
4.2	Micrographs and mode renderings of the wedge resonator from top and side views. <b>(a)</b> An optical micrograph shows a top view of a 1-mm-diameter wedge resonator. <b>(b)</b> A scanning electron micrograph shows the side-view of a resonator. The insets here give slightly magnified micrographs of resonators in which the wedge angle is 12 degrees (upper inset) and 27 degrees (lower inset). The small circle shows the approximate location of the taper during measurements. <b>(c)</b> A rendering shows calculated fundamental-mode intensity profiles in 10 degree and 30 degree wedge angle resonators at two wavelengths. As a guide, the center-of-motion of the mode is provided to illustrate how the wedge profile introduces normal dispersion that is larger for smaller wedge angles. . . . .	31

4.3	The fabrication procedure of disk resonators . . . . .	32
4.4	Data plot showing the effect of etch time on appearance of the “foot” region in etching of a 10- $\mu$ m-thick silica layer. The foot region is a separate etch front produced by wet etch of silica that is empirically observed to adversely affect the optical Q factor. The data show that by control of the etch time the “foot” region can be eliminated. The upper-left inset is an image of the foot region and the lower right inset shows the foot region eliminated by increase of the wet etch time. . . . .	34
4.5	Data showing the measured Q factor plotted versus resonator diameter with oxide thickness as a parameter. Multiple devices were measured for each data point, however, the dispersion in Q values was typically low so that error bars are not shown and only the average Q value device is shown. For example, the average Q data (red points) are taken from the following set where each Q value represents a distinct device: $D \approx 7.5$ mm, $Q \approx 799$ M, 875 M; $D \approx 3$ mm, $Q \approx 326$ M, 331 M, 367 M; $D \approx 1$ mm, $Q \approx 169$ M, 174 M; $D \approx 0.5$ mm, $Q \approx 88$ M, 91 M. The solid lines show the predicted Q factor from a model that accounts for surface-roughness-induced scattering loss and also material loss (fitting gives a material Q of 2.5 billion). The r.m.s. roughness is measured using an AFM (see Methods section for values). The red data points correspond to a wedge angle of 27 degrees. All other data are obtained using a wedge angle of approximately 10 degrees. The inset shows a spectral scan for the case of a record Q factor of 875 million. In this spectrum, the resonator is undercoupled so that the linewidth is close to the intrinsic value. However, both critical coupling and strong over-coupling are also possible by adjusting the air gap between the taper and the resonator. The sinusoidal curve accompanying the spectrum is a calibration scan performed using a fiber interferometer. . . . .	35
4.6	Broad spectral scan over 3 free spectral ranges (FSR) of a 3-mm-diameter resonator. . . . .	36

4.7	Plot of measured free spectral range (FSR) versus the target design-value resonator diameter on a lithographic mask. The plot shows one device at each size and five different sizes. The r.m.s. variance is 2.4 MHz (relative variance of less than 1:4,500). The inset shows the FSR data measured on four devices having the same target FSR. An improved variance of 0.45 MHz is obtained (a relative variance of 1:20,000). . . . .	37
4.8	Optical Q versus diameter for three distinct wedge angles showing the systematic improvement of Q value with increasing wedge angle . . . . .	38
4.9	Illustration of tuning control of the SBL devices. <b>(a)</b> SBL threshold is measured as a function of pump wavelength using four slightly different resonator diameters. FSRs are indicated in the legend. <b>(b)</b> Illustration of the control of the SBS gain with the change of FSR and pump wavelength. <b>(c)</b> Spectrum of Brillouin laser output showing pump laser (lower peak) and laser output (higher peak). The pump wave appears weaker because the laser emission occurs along the opposite direction to the pump wave. . . . .	40
5.1	An SEM micrograph showing a cross section of the spiral delay line. <b>(a)</b> Silicon pillars support thermal oxide structures, the outer edge of which guides the optical mode. <b>(b)</b> Close-up view of oxide edge that is formed using a non-optimized etch. Two etch fronts are apparent along with roughening of the oxide surface. <b>(c)</b> Close-up view of oxide edge that is formed using an optimized etch. Etch duration has been increased to eliminate one of the etch fronts, resulting in a smooth edge. <b>(d)</b> The finite element simulation of the fundamental optical mode propagating inside the waveguide. Scale bars: <b>(a)</b> 100 $\mu\text{m}$ ; <b>(b)</b> 0.5 $\mu\text{m}$ ; <b>(c)</b> 0.5 $\mu\text{m}$ ; <b>(d)</b> 8 $\mu\text{m}$ . . . . .	47
5.2	Optical backscattering measurement setup. Optical fiber and index-matching oil are used for end-fire coupling. . . . .	49

- 5.3 Optical micrographs and backscatter reflectometer data for a single spiral and a monolithic spiral cascade. **(a)** An optical micrograph of a 7 m physical path length, counter-clockwise spiral. This spiral has a diameter of 4.3 cm. **(b)** Optical backscatter reflectometer measurement of the spiral waveguide shown in panel **(a)**. On account of the return path, the backscatter decay rate is increased by twofold. The blue curve is a fit to the backscatter level, while the green curve gives a fit to the local backscatter decay rate, and the red curve uses a model to infer the actual local waveguide attenuation, which is approximately 0.08 dB/m over most of the spiral. The upper axis gives the radius from center while the lower axis gives the physical path length. **(c)** Optical micrograph of a cascaded, four-spiral waveguide having a physical path length of 27 m. The input port is in the upper left of the image, and the waveguides connecting neighboring spiral delays are visible. The entire chip is 9.5 cm × 9.5 cm and consists of four, separately exposed and stitched lithography fields. **(d)** Optical backscatter reflectometer measurement of the spiral waveguide delay line shown in panel **(c)**. The periodic singularities (blue circles) in the backscatter signal correspond to the optical wave transiting the inner adiabatic coupling region of each spiral. Other discontinuities (green squares) in back-scatter occur when the optical wave transfers between the spirals and result from higher-order transverse modes being mode filtered. The inset to panel **(d)** is a magnified view of the adiabatic coupling section, which is approximately 1 mm in diameter. Scale bars: **(a)** 1 cm; **(c)** 2 cm; **(d)** 500 μm . . . . . 50
- 5.4 The calibration of spiral waveguide attenuation. The naive linear fitting in the upper panel gives an underestimated 0.05 dB/m loss. In contrast, the lower panel shows a more precise local attenuation rate calibrated based on Eq.(5.4). 51
- 5.5 The connection loss between cascade spirals can be improved via a local etching which increases the silicon undercut at the connection from 70 μm to 85 μm. 54

5.6	Analysis of waveguide loss and adiabatic coupler insertion loss using backscatter data. Green data points are generated by taking the ratio of backscatter signals at symmetrically offset distances away from the adiabatic coupler in spiral 3 of Fig. 5.3(c). The intercept reveals the insertion loss of the coupler as given by a range of possible values falling within a confidence interval. The fitted line (red solid line) slope of about 0.1 dB/m provides a measure of the waveguide attenuation rate and is in reasonable agreement with the spiral in Fig. 5.3(a). The dotted read lines provide the 95% confidence interval. . . . .	55
5.7	The optical images of cascade spirals consist of 2( <b>a</b> ), 4( <b>b</b> ), and 6( <b>c</b> ) individual spirals. The total delay of spirals are 6.7 m, 3.6 m, and 1.6 m, respectively. . .	57
5.8	Optical backscatter reflectometer measurements of various cascade spiral waveguides shown in Fig. 5.7 . . . . .	58
5.9	The wavelength dependence of waveguide loss. The loss is measured with backscattering reflectometry over a wavelength range of 1528 to 1608 nm in a 7-m-long spiral waveguide. The minimum loss measured is $(0.05 \pm 0.015)$ dB/m near a wavelength of 1595 nm. The values plotted have been calibrated for spiral curvature using Eq. (5.5). A measurement window of 5 nm is applied [1, 2]. Error bars are included on each point and have been computed by standard deviation of three independent measurements. . . . .	60
5.10	Bending loss data plotted versus the bending diameter. The blue squares are data points obtained from Q measurement on resonators of varying diameters. The black curve is a fit to the data using roughness data provided in the text and obtained using an AFM. The principle source of roughness is the lower interface and an estimate of the bending loss in case this surface can be smoothed to the level of the upper surface is provided as the red curve. The inset shows a modified version of the spiral design in which a waveguide ridge is created so as to provide both interior and exterior guiding in the spiral. The two, color-graded regions give the mode intensity profile. . . . .	61
5.11	Comparison of backscattering trace between S-bend hand off and Archimedean part of spiral waveguide. . . . .	63

5.12 Demonstration of the spiral waveguide in the function of data delay as might occur in an optical buffer. **(a)** Experimental setup used to test a 13.5 m long cascaded spiral in the function of a buffer for a 2.5 Gb/s data stream. Beginning in the upper left of the panel, a single-frequency laser source is modulated to create a pseudorandom bit stream. The bit stream is amplified and coupled into the spiral delay line. Subsequent to the delay, the signal is attenuated, detected, and displayed on an oscilloscope to generate eye patterns. Polarization controllers are also used to launch signals on either the TE or TM mode of the delay line. **(b)** Eye patterns generated with the 13.5 m spiral delay replaced by a fiber optical cable. **(c)** Eye patterns generated with the data stream buffered in the 13.5 m spiral delay. The eye patterns of the detected input and output data streams were averaged over 10 s with no visible degradation or change in the structure of the eye pattern. . . . . 64

6.1 An illustration of the generic connection design problem. Waveguides A and B are shown linked by the connection waveguide (dashed). To create a low insertion loss, coupling to higher-order modes must be reduced at the connecting points as well as through out the transition. The inset shows the curvature ( $\kappa$ ) versus path length,  $z$ . . . . . 74

6.2 Conformal mapping between a bent waveguide and a straight waveguide. The transverse refractive index,  $n(x, y)$ , of the curved waveguide is mapped to  $n_{eq}^2(u, v, z) = n^2(u, v)e^{2u\kappa(z)}$  for a straight guide. . . . . 75

6.3 The optimal S-bend design that minimizes mode coupling between clockwise and counter-clockwise Archimedean spiral waveguides. A jump from  $0.5\pi$  to  $-0.5\pi$  of the tangent vector in the upper right panel is due to the convention that the tangent vector is defined as  $[-0.5\pi, 0.5\pi]$  (for example, a tangent vector of  $0.6\pi$  is considered as  $0.6\pi - \pi = -0.4\pi$ ). The geometry property is still continuous. . . . . 79

- 6.4 (a) Optical micrograph of a spiral waveguide having a physical path length of 7 meters. The input port is in the upper left of the image, and there are two small spirals at the input and output ports (not resolved in the backscatter trace of panel (c)). The entire chip is  $4.5\text{ cm} \times 4.5\text{ cm}$ . (b) A magnified view of the adiabatic coupling section (approximately 1 mm in diameter). Light brown regions are silicon (under oxide or exposed) while darker brown regions along the border of the light brown are silica that has been undercut by dry etching. Very dark brown border regions are also silica but have a wedge profile. For further details see Ref. [3]. (c) Optical backscatter reflectometer measurement of the spiral waveguide. Besides occasional random noise spikes that we believe are associated with small dust particles on the surface of the waveguide, the major singularities in the backscatter signal correspond to the input facet, the optical wave transiting the inner adiabatic coupling region of the spiral and the output facet. The inset shows a close-in view of the adiabatic coupler region (*i.e.*, peak of the singularity). There is no apparent drop in signal within this region. (d) Analysis of the adiabatic coupler insertion loss using backscatter data. Data points are generated by taking the ratio of backscatter signals at symmetrically offset distances away from the adiabatic coupler in (a). The intercept reveals the insertion loss of the S connection as given by a range of possible values falling within a confidence interval determined by linear regression. . . . . 81
- 6.5 The S-connection intercept (see Fig. 6.4(d)) measured with backscattering reflectometry over a wavelength range from 1536 to 1598 nm in a 1-meter-long spiral waveguide. A measurement window of 10 nm is applied. The error bars are obtained from three independent measurements. . . . . 83
- 6.6 (a) A high-spatial-resolution, backscatter trace of an unsuccessful S-bend design based on a conventional clothoid curve design. About 2.5 dB insertion loss was measured using the OBR measurement technique. (b) Micrograph of the clothoid curve S connection. . . . . 84

6.7	(a) An optical micrograph of a resonator with two connectors. This resonator has a round-trip length of 1.5 cm. Buffer patterns are introduced to achieve the uniform etching via loading effect. (b) A spectral scan for the case of a Q factor of $8 \times 10^6$ . . . . .	85
7.1	An example of spiral waveguide design. (a) A MATLAB-generated spiral waveguide design consists of two individual spirals. The surrounding red patterns are buffering patterns. (b) A zoom-in view of the center of spiral waveguide pattern. The red patterns in the center are buffering patterns to reduce the loading near the S-bend connection. . . . .	90
7.2	An SEM image showing a cross section of the Archimedean part of a spiral waveguide. $w$ is the width of the waveguide; $g$ is the separation between two neighbor waveguides; $u$ is the silicon undercut; and $p$ is the width of the supporting silicon pillar. . . . .	91
7.3	The total time delay achieved by a single-spiral waveguide with different outer radius and pitch sizes ( $w + g$ ) . . . . .	92
7.4	Desired undercut to avoid interaction between optical field and silicon pillar for oxide thickness 6 $\mu\text{m}$ and 12 $\mu\text{m}$ and wedge angle $14^\circ$ , $27^\circ$ , $45^\circ$ . . . . .	93
7.5	A microscope image of S-bend connection suffered from cracks. The black arrow indicates the position of crack. . . . .	95
7.6	Loss measurements results of S-bend connection with various sizes ( $A$ ) . . . . .	96
7.7	Chance of presenting cracks of S-bend connection with various sizes ( $A$ ) . . . . .	97
7.8	Examples of Hill function $H_{n,d}(x)$ . . . . .	98
7.9	An example of tapered waveguide design. (a) A microscope image of tapering waveguide near the center of spiral. (b) A plot shows the width of waveguide in the tapering region . . . . .	98
7.10	Loss measurement results of S-bend connection with various tapering rates ( $d$ ). The structure measured here has the same S-bend connection design with $A = 500 \mu\text{m}$ . . . . .	99

- 7.11 An example of establishing connections between two individual spirals. The blue curves outline two identical individual spirals to be connected. The red waveguide starts at  $(x_0, y_0)$  and ends at  $(x_1, y_1)$ . The black curve starts at and ends  $(2x_1 - x_0, y_0)$  at  $(x_1, y_1)$ . . . . . 101
- 8.1 Experimental setup for nanoparticle and biomolecule detection using a temperature-stabilized reference interferometer. The output of a tunable laser is split into two branches by a 90/10 coupler. One branch is coupled into/out of a microtoroid resonator in an aqueous environment. The other branch is coupled into a reference interferometer to monitor the laser optical frequency in real time. Immersion of the reference interferometer in an ice-water bath provides long-term frequency stability. (Inset) SEM micrograph of a  $R = 25$  nm bead binding on the surface of a microtoroid . . . . . 107
- 8.2 Resonant wavelength data from nanobead detection measurements. **(a)** Resonance wavelength shift vs. time for binding of  $R = 50$  nm (red),  $R = 25$  nm (blue), and  $R = 12.5$  nm (green) polystyrene nanobeads. In  $R = 12.5$  nm bead experiments, the shift of the split-resonance center wavelength (Inset I) as well as the shift of longer-wavelength resonance (Inset II) are presented. For comparison, the gray trace is the same data run as the red trace, but using the conventional sweep voltage method. **(b)** Histogram of measured binding-induced step sizes for beads of radius  $R = 12.5$  nm (green), 25 nm (blue), and 50 nm (red). The squares are the predicted maximum shift from a finite element calculation. Error bars give  $\sqrt{2}\sigma$  where  $\sigma$  is the standard deviation of 10 measured points before the measured step. Inset shows a magnified view for the 12.5 nm bead data. . . . . 109
- 8.3 **(a)** Resonance wavelength shift (scan A) and splitting frequency shift (scan B) of a microtoroid immersed in a 1 pM InfA solution. Many steps are visible in scan A, including a step of  $8.4 \pm 0.3$  fm (magnified within Inset I). The same event is detected as a split frequency shift in scan B (magnified within Inset II). A histogram of measured, resonance wavelength-shift steps is provided in (b) and includes a maximum wavelength step of 11.3 fm (displayed within the inset of (b)). . . . . 112

# List of Tables

5.1	Loss characterization of 27 m cascade spiral waveguides in Fig. 5.3(c) . . . . .	54
5.2	Loss characterization of cascade spiral waveguides shown in Fig. 5.7 . . . . .	59
8.1	Perturbation brought by proteins. The frequency shifts are estimated based on a microtoroid with major diameter 80 $\mu\text{m}$ and minor diameter 6 $\mu\text{m}$ with a fundamental whispering gallery mode at 680 nm wavelength. . . . .	105
8.2	The estimated frequency (wavelength) shift caused by an InfA viron ( $\lambda \approx 680 \text{ nm}$ ). . . . .	106
8.3	Complex refractive index (RI) of polystyrene and water at $\lambda_0 = 680 \text{ nm}$ . . .	117
8.4	The scattering and absorption cross section of polystyrene beads suspended in water at $\lambda_0 = 680 \text{ nm}$ . . . . .	117
8.5	The reactive and thermo-optic shift induced by polystyrene and silica beads attaching to the surface of microtoroids ( $\lambda_0 = 680 \text{ nm}$ ). In the calculation, we assume loaded Q factor of 100 million and coupled power of 1 $\mu\text{W}$ . The dimension of toroid is set to have major diameter 85 $\mu\text{m}$ and minor diameter 15 $\mu\text{m}$ . . . . .	117
8.6	The reactive and thermo-optic shift induced by polystyrene and silica beads attaching to the surface of microtoroids ( $\lambda_0 = 680 \text{ nm}$ ). In the calculation, we assume loaded Q factor of 100 million and coupled power of 1 mW. The dimension of toroid is set to have major diameter 85 $\mu\text{m}$ and minor diameter 15 $\mu\text{m}$ . . . . .	118

# List of Publications

Portions of this thesis have been drawn from the following publications:

1. Hansuek Lee, **Tong Chen**, Jiang Li, Oskar Painter, and Kerry J. Vahala, Ultra-low-loss optical delay line on a silicon chip. *Nature Communications*, **3**:doi:10.1038/ncomms1876 (2012)
2. **Tong Chen**, Hansuek Lee, Jiang Li, and Kerry J. Vahala, A general design algorithm for low optical loss adiabatic connections in waveguides. *Optics Express*, **20**, 22819–22829 (2012)
3. Hansuek Lee\*, **Tong Chen**\*, Jiang Li\*, Ki Youl Yang, Seokmin Jeon, Oskar Painter, and Kerry J. Vahala, Chemically etched ultrahigh-Q wedge-resonator on a silicon chip. *Nature Photonics*, **6**, 369–373 (2013) \*These authors contributed equally to this work.
4. **Tong Chen**, Hansuek Lee, and Kerry J. Vahala, Thermal stress in silica-on-silicon disk resonators. *Applied Physics Letters*, **102**, 031113 (2013)
5. Tao Lu\*, Hansuek Lee\*, **Tong Chen**, Steven Herchak, Ji-Hun Kim, Scott E. Fraser, Richard C. Flagan, and Kerry J. Vahala, High sensitivity nanoparticle detection using optical microcavities. *Proceedings of the National Academy of Sciences*, **108**, 5976–5979 (2011) \*These authors contributed equally to this work.
6. **Tong Chen**, Hansuek Lee, and Kerry J. Vahala, Design and characterization of whispering-gallery spiral waveguides. *Optics Express*, *submitted* (2013)
7. Ivan Grudinin\*, Hansuek Lee\*, **Tong Chen**, and Kerry J. Vahala, Compensation of thermal nonlinearity effect in optical resonators. *Optics Express*, **19**, 7365–7372 (2011) \*These authors contributed equally to this work.
8. Tao Lu\*, Hansuek Lee\*, **Tong Chen**, and Steven Herchak, Fast nano particle and single molecule detection with an ultra-narrow-linewidth microlaser. *Nature Communications*, *submitted* (2013) \*These authors contributed equally to this work.

9. Jiang Li\*, Hansuek Lee\*, **Tong Chen**, and Kerry J. Vahala, Characterization of a high coherence, Brillouin microcavity laser on silicon. *Optics Express*, **20**, 20170–20180 (2012) \*These authors contributed equally to this work.

10. Jiang Li, Hansuek Lee, **Tong Chen**, and Kerry J. Vahala, Low-pump-power, low-phase-noise, and microwave to millimeter-wave repetition rate operation in microcombs. *Physical Review Letters*, **109**, 233901 (2012)

# Chapter 1

## Introduction

### 1.1 Optical microresonators

There has been intense interest in optical microresonators for some time. They are finding application in an increasingly diverse set of subjects including: cavity QED, nonlinear optics, communications, frequency microcombs, and biodetection [4-8]. Cavity Q factor is a prominent consideration in most applications, and efforts have therefore been directed towards realization of high-Q, chip-based devices. Due to its ultralow-transmission losses in the optical communication band (1550 nm), fused silica is a great dielectric material candidate for solid microcavities. Various geometries of silica resonators have been investigated, including microdisks with Q above  $10^7$  [9], microtoroids with Q above  $10^8$  [10], and even to microspheres at the top of fused silica fiber with Q even higher. Braginsky and Ilchenko pioneered the study of ultrahigh-Q microspheres [11]. Silica microspheres with Q as high as  $8 \times 10^9$  were then demonstrated by Gorodesky [12] and Vernooy [13], close to the intrinsic material loss of silica. Among these devices, microtoroid resonators have offered a unique combination of ultrahigh-Q performance ( $Q > 100$  million) in an extremely compact, silicon-chip-based structure [10]. Light within the optical microtoroid is confined by total internal reflection near the cavity perimeter, and the corresponding modes have been called “whispering-gallery” modes. Nonetheless, the silica reflow step that is required to fabricate these devices, presents limitations on precise control of device size and shape, as well as resonator placement near other photonic devices. Also, attaining ultrahigh Q in a millimeter-to-centimeter range that cannot be easily accessed using microtoroids (on account of limitations of the reflow process) is important for realization of microwave-rate free spectral range in certain nonlinear sources, microcomb [5], and potentially for rotation

sensing [14].

## 1.2 Optical waveguides

Light propagation through an optical fiber causes a long, non-resonant (true) time delay used in numerous applications such as rotation sensing, radio frequency photonics, high-stability microwave oscillators, and all-optical signal processing [14–20]. In contrast to how it is deployed in optical communication systems, fiber is coiled in these applications to reduce footprint. This is a configuration better suited for a chip-based waveguide that would improve shock resistance, and afford the possibility of integration for system-on-a-chip functionality. Yet, there is a multi-order-of-magnitude gap between the loss of optical fiber and chip-based photonic waveguides. The lowest attenuation rates are obtained for a silica-based or silica-clad guide and there has been interest in the practical limits of optical loss in such structures [21–23]. For a pure silica core waveguide [23] the state-of-the-art does not reflect fundamental material limits, but is instead set by interface roughness on the waveguide itself. The question of reducing optical loss in photonic circuits has been considered for some time.

## 1.3 Thesis outline

This thesis presents the development of on-chip ultralow-loss optical resonators and waveguides. We aim to demonstrate on-chip, semiconductor-compatible, ultralow-loss optical resonators and waveguides for various photonic applications. **Chapter 2** starts with the fundamentals of the optical microresonators, their loss source, and experimental testing approaches.

**Chapter 3** explores and solves the thermal stress induced buckling issue in scaling the disk resonator to millimeter-to-centimeter size [24]. The thermal expansion mismatch of thermal-grown silica on a silicon wafer is well known to induce compressive stress upon cooling from the growth temperature to room temperature. The resulting strain is most apparent when undercutting silica to create cantilever or bridging structures. We investi-

gate how this stress impacts silica disk structures by comparison of measurements with both a finite element and an analytical model. The disk structures studied are also whispering gallery optical resonators and proper control of stress is critical to obtain high-Q resonances. Based on our analysis, thicker oxide layers and proper control of undercut enable ultrahigh optical performance and mechanical stability. Then, in **Chapter 4**, we demonstrate the first, on-chip microcavity that provides ultrahigh-Q performance without the need for a re-flow step. Q factors as high as 875 million are measured. The resonators have a distinctive wedge shape and their process flow uses only standard semiconductor methods beginning with oxide on silicon.

**Chapter 5** demonstrates a monolithic waveguide as long as 27 m (39 m optical path length), and featuring broadband loss rate values of  $(0.08 \pm 0.01)$  dB/m measured over 7 m by optical backscatter [3]. Resonator measurements show a further reduction of loss to 0.037 dB/m, close to that of optical fibers when they were first considered a viable technology. Scaling this waveguide to integrated spans exceeding 250 m and attenuation rates below 0.01 dB/m is discussed. In designing the “S-bend” of a whispering-gallery spiral waveguide, we propose, in **Chapter 6**, a variational approach to design adiabatic waveguide connections with minimal intermodal coupling [25]. The final design “S-bend” is optimized with approximately 0.025 dB insertion loss. Compared to other approaches, our algorithm requires less fabrication resolution and is able to minimize the transition loss over a broadband spectrum. The method can be applied to a wide range of turns and connections and has the advantage of handling connections with arbitrary boundary conditions. **Chapter 7** address the general design issue in generating the photomasks for an ultralow-loss optical waveguide. The optical loss is carefully controlled across the whole waveguide. The design guidance in this chapter provide great flexibility in generating photomasks for various waveguide structures.

**Chapter 8** discusses application of optical microresonators in bio-sensing [7]. We demonstrate a highly sensitive nanoparticle and virus detection method by using a thermal-stabilized reference interferometer in conjunction with an ultrahigh-Q microcavity. Sensitivity is sufficient to resolve shifts caused by binding of individual nanobeads in solution down to a record radius of 12.5 nm, a size approaching that of single protein molecules. Also, thermal-optic effect in nano/bio-sensing is theoretically investigated and discussed.

## Chapter 2

# Optical Microresonators and Their Basis

Microresonators (microcavities) are resonators in which one or more of the spatial dimensions assumes the size of a few wavelengths of light or smaller. Optical microresonators confine light to small volumes and are already indispensable for a wide range of applications and studies [4] due to their small optical mode volume and high quality factor (Q). In this chapter, the basis of optical microresonators will be reviewed to offer a brief introduction on the basic properties.

### 2.1 Whispering-gallery mode

Whispering-gallery waves were originally introduced for the case of St Paul's Cathedral circa 1878 by Lord Rayleigh for sound waves propagating close to the cylindrical wall. Besides acoustic ones, whispering-gallery waves also exist for light. Whispering-gallery mode resonances correspond to light that is trapped in circular orbits just within the surface of the microresonators. Intuitively, the propagation of the lightwave can be understood in geometrical optics. For example, we have considered a cylindrical resonator of radius  $R$  and refractive index  $n$  surrounded by an environment of refractive index 1. If the path taken by the whispering-gallery mode during a roundtrip within the cavity is a multiple of the wavelength ( $\lambda$ ) then a resonance occurs. The resonance condition is given by

$$2\pi n_{eff}R = m\lambda \tag{2.1}$$

where  $m$  is an azimuthal mode number, and  $n_{eff}$  is the effective mode index. Nowadays, the whispering-gallery resonators have cylindrical, spherical, spheroidal/toroidal, ring, and other shapes and topologies [4]. The analytical expressions for the disk [9, 26] and toroid [10] mode structure are not possible because only one coordinate of the wave equation is separable. The two-dimensional Helmholtz equation must be solved numerically. Start with Maxwell's equations

$$\nabla \times (\nabla \times \vec{E}(\vec{r})) + \frac{\epsilon(\vec{r})}{c^2} \frac{\partial^2 \vec{E}}{\partial t^2} = 0. \quad (2.2)$$

For an optical mode with frequency  $\omega$ , we have a corresponding Helmholtz equation in Coulomb gauge:

$$(\nabla^2 + \mu\epsilon\omega^2)\vec{E} = (\nabla^2 + \frac{\omega^2 n^2}{c^2})\vec{E} = 0 \quad (2.3)$$

where  $c$  is the speed of light in the vacuum and we have assumed that the refractive index is homogeneous. The whispering-gallery mode in microresonators can be classified into transverse-electric (TE) modes or transverse-magnetic (TM) modes. In TE modes, the electric field is transverse to the propagation direction. Similarly, in TM modes, the magnetic field is transverse to the propagation direction. All the remaining field components can be expressed in terms of only one field component ( $H_\phi$  for TE modes and  $E_\phi$  for TM modes), simplifying the problem to a scalar Helmholtz equation for one field component. Taking TM modes as an example, we have

$$\left[ \left( \frac{\partial^2}{\partial r^2} + \frac{1}{r} \frac{\partial}{\partial r} \right) + \frac{1}{r^2} \frac{\partial^2}{\partial \psi^2} + \frac{\partial^2}{\partial z^2} + \frac{\omega^2 n^2}{c^2} \right] E_\phi = 0. \quad (2.4)$$

Due to the periodic condition the TE and TM modes can be expressed as:

$$\begin{aligned} E_\phi(r, z, \phi) &= E_\phi(r, z) \cdot \exp(m\phi - \omega t) \\ H_\phi(r, z, \phi) &= H_\phi(r, z) \cdot \exp(m\phi - \omega t) \end{aligned} \quad (2.5)$$

where  $m$  is the angular mode number. Here, because of the rotational symmetry of our resonators, it is natural to choose cylindrical coordinates for the modeling. The Helmholtz

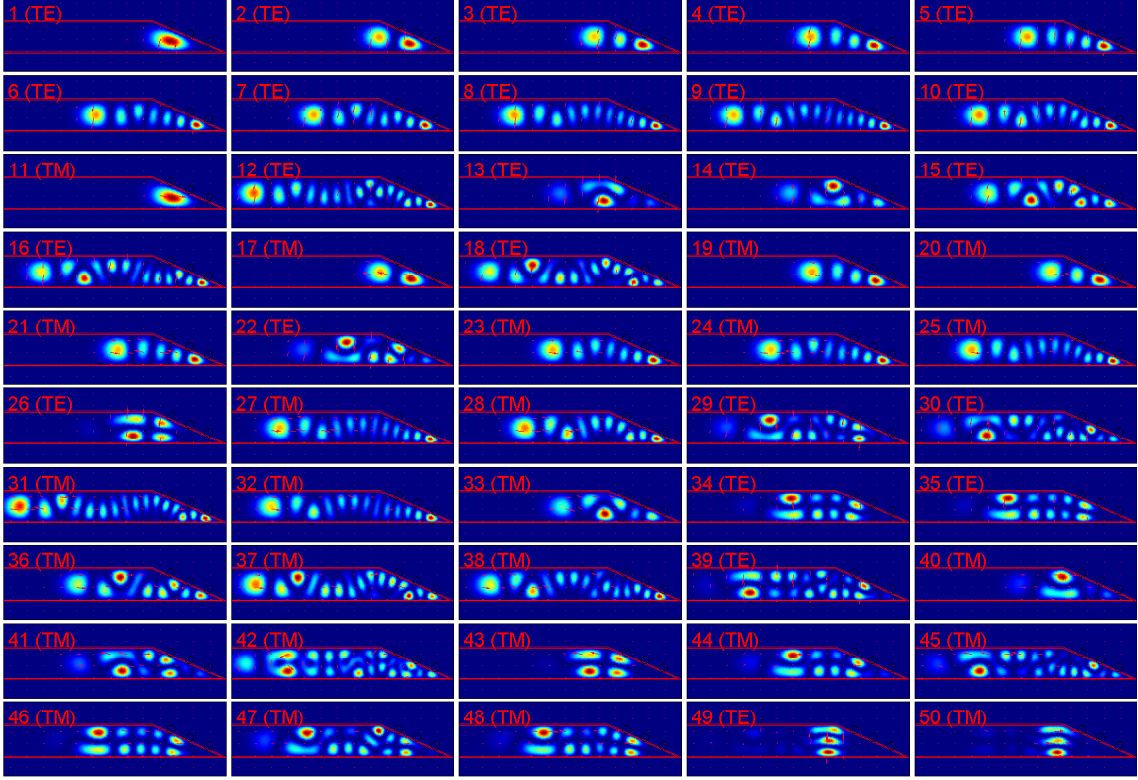


Figure 2.1: Finite element simulation results of mode intensity profiles in resonators with 7.5 mm diameter, 10  $\mu\text{m}$  oxide thickness, and 21 $^\circ$  wedge angle

for TM modes, for example, is

$$\left(\frac{\partial}{\partial r} \frac{1}{r} \frac{\partial}{\partial r} + r \frac{\partial^2}{\partial z^2}\right) E_\phi(r, z) + \left(\frac{\omega^2 n^2}{c^2} - \frac{m^2}{r^2}\right) r E_\phi(r, z). \quad (2.6)$$

The whispering-gallery mode profiles and eigenfrequency can be then calculated by via finite element simulation [27]. Figure 2.1 shows an example of calculated transverse modes for a resonator with 7.5 mm diameter, 10  $\mu\text{m}$  oxide thickness, and 21 $^\circ$  wedge angle.

## 2.2 Quality factor

The concept of quality (Q) factor is universal and is applied to numerous resonating systems. It quantifies how under-damped an oscillator or resonator is, or equivalently, characterizes a resonator's bandwidth relative to its center frequency. Indeed, Q factor is the most commonly quoted specification of a microresonator and even built into the name given to

ultrahigh-Q (UHQ) microresonators. The general definition of the Q factor is

$$Q = 2\pi \cdot \frac{\text{Energy stored}}{\text{Energy loss per cycle}} \quad (2.7)$$

In particular, the optical performance of microresonators can be evaluated by the optical Q factor of their resonances, which can be expressed in terms of the linewidth of the cavity resonance.

$$Q = \frac{\lambda}{\Delta\lambda} \approx \frac{\omega}{\Delta\omega} \quad (2.8)$$

where  $\omega(\lambda)$  is the resonance frequency (wavelength) and  $\Delta\omega(\Delta\lambda)$  is the full-width at half-maximum of the resonance lineshape. Equivalently, the frequency dependent definition of Q is

$$Q(\omega) = \omega \cdot \frac{\text{Maximum Energy Stored}}{\text{Power Loss}} = \omega\tau \quad (2.9)$$

where  $\tau$  is the cavity photon life time. These two definitions of Q offer two distinct approaches for experimental measurements of the intrinsic Q factor of microcavities.

### 2.2.1 Scanning measurements

The simplest measurement of resonator Q is based on the measurement of its linewidth. During the measurements, the tunable laser wavelength is linearly scanned at 2–10 Hz. The injected optical power is kept low ( $P < 1 \mu\text{W}$ ) to avoid thermal broadening of the cavity linewidth [28]. The lightwave is coupled into the resonator via a tapered fiber. Its transmission is measured by a photo-detector and captured by an oscilloscope. The resonator linewidth is then determined by fitting the resonance lineshape to a Lorentzian function. To accurately calibrate the laser scan in this measurement, a portion of the laser output was also monitored after transmission through a calibrated Mach-Zehnder interferometer with a free spectral range (FSR) of 5–10 MHz. Figure 2.2 presents a spectral scan obtained on a device with a Q factor of 750 million.

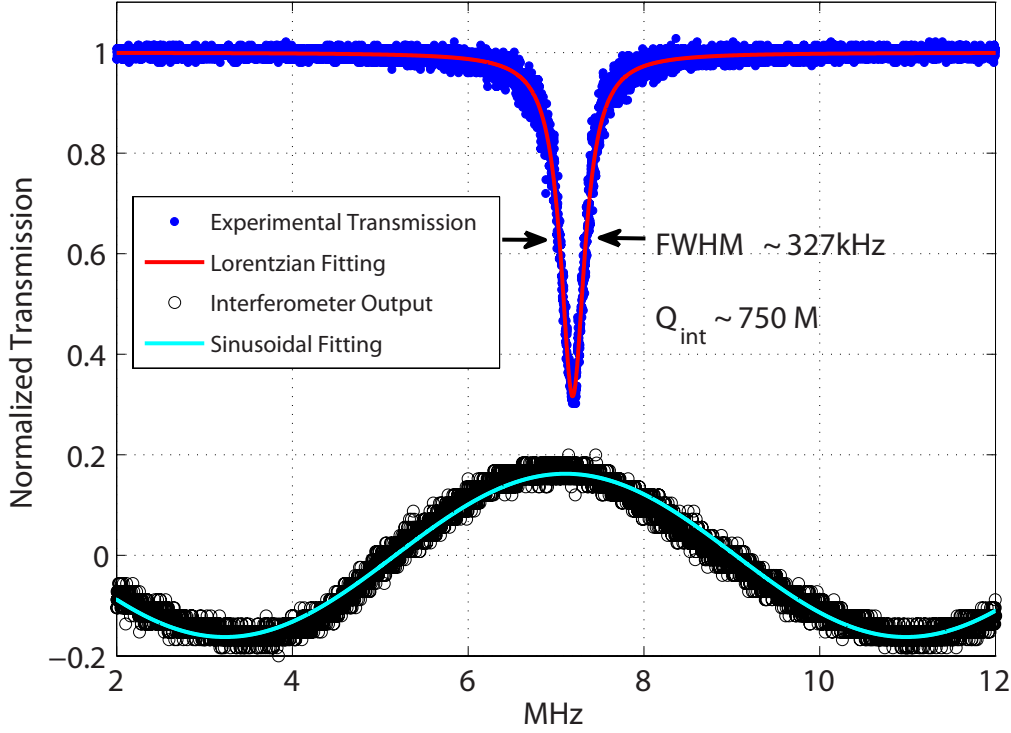


Figure 2.2: The measured optical spectrum of a device featuring a Q factor of 750 million. The black data are concurrent scans from an interferometer used to calibrate the resonant linewidth. The FSR of the Mach-Zehnder interferometer here is 7.75 MHz.

### 2.2.2 Cavity ring-down measurements

Alternatively, from its definition in Eq. (2.9), the Q factor can be accurately determined by cavity ring-down measurements, which allows direct recording of the photon lifetime in the time domain. This approach is immune to the thermal broadening [28] effects and the transient effects which are associated with scanning over a cavity resonance, and constitute a systematic error in the measurement of the cavity Q factor. During the ring-down measurements, the laser wavelength is scanned in time and coupled into the resonator via a tapered fiber. At  $t = 0$ , the laser excitation is gated off via a high-speed, external phase modulator. Afterwards, the taper output power is due entirely to the exponential decay of energy stored in the resonator. The critical decay signal is then

$$A(t) = \left(\frac{2\tau_{ex}}{\tau_0 + \tau_{ex}}\right)^2 A(t=0) e^{-(t+\Delta t)\left(\frac{1}{\tau_{cir}}\right)} \quad (2.10)$$

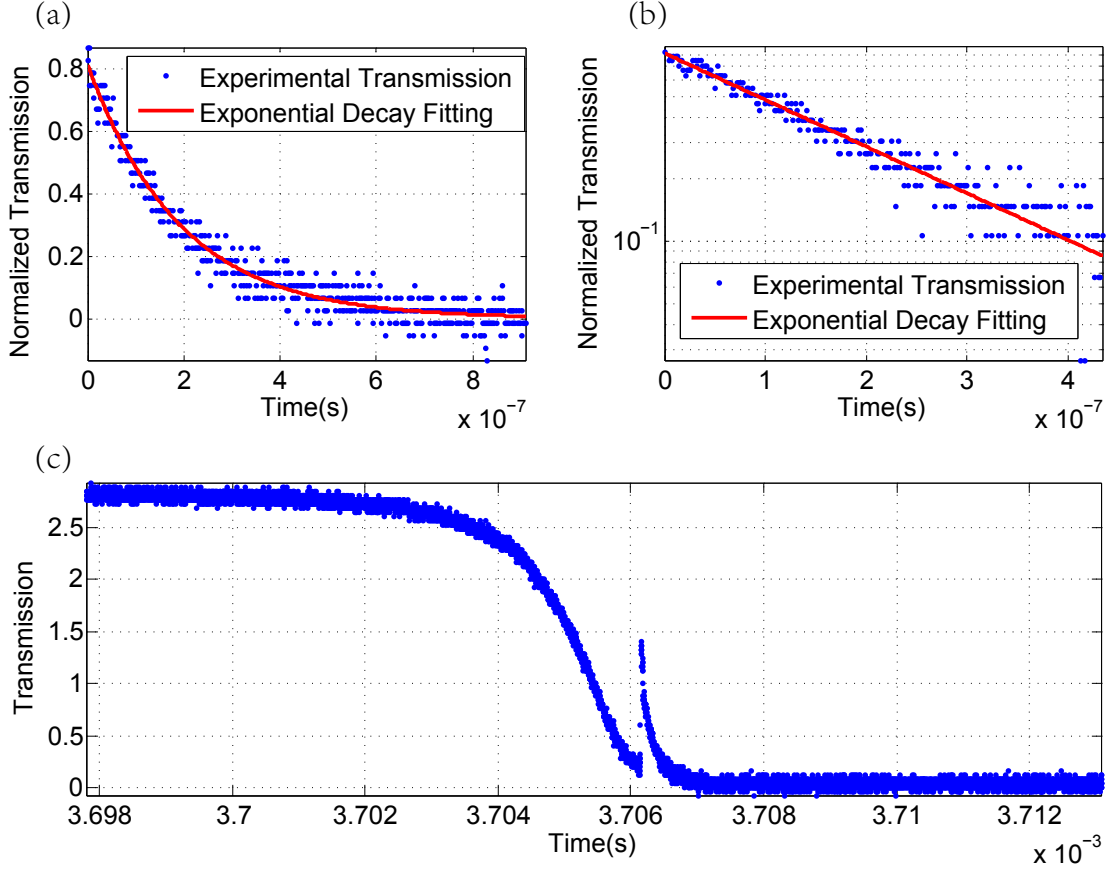


Figure 2.3: Ring-down measurement of cavity Q. The intensity decay in time is fit to an exponential decay function. Subfigure (a) and (b) are extracted from (c), which shows the transmission, upon gating-off the laser.

where  $\Delta t$  is the laser gated off delay. The time trace of taper output power is recorded using a high-speed photo-detector and oscilloscope (see Fig. 2.3(c)). The cavity lifetime is measured by fitting an exponential to the taper transmission. Fig. 2.3(a)–(c) shows an example of ring-down measurement. To calibrate the intrinsic life-time ( $t_0$ ) of the resonator, we then account for taper loading ( $t_{ext} = \frac{Q_{ext}}{\omega}$ ).

$$t_0 = t_{cir} + t_{ext} \quad (2.11)$$

where  $Q_{ext}$  is the external Q factor resulting from coupling to the output and  $\omega$  is the optical angular frequency.

## 2.3 Optical loss in optical microresonators

In the case of a microresonators, the total Q factor results of several loss contributions: intrinsic material loss (both absorption and scattering), surface scattering loss, surface absorption loss (e.g., due to the presence of adsorbed water), whispering gallery loss, and external coupling loss. Therefore, the total (loaded) Q factor of a microresonator depends on the dissipation mechanisms above

$$\frac{1}{Q} = \frac{1}{Q_{mat}} + \frac{1}{Q_{ss}} + \frac{1}{Q_{sa}} + \frac{1}{Q_{wgm}} + \frac{1}{Q_{ext}} = \frac{1}{Q_0} + \frac{1}{Q_{ext}} \quad (2.12)$$

where  $Q$  is the total Q factor,  $Q_{mat}$  is the Q factor by the material loss,  $Q_{ss}$  is the Q factor by the surface scattering,  $Q_{sa}$  is the Q factor due to surface absorption,  $Q_{wgm}$  is the Q factor due to whispering gallery loss,  $Q_0$  is the intrinsic Q factor, and  $Q_{ext}$  is the external Q factor resulting from coupling to the output waveguide or taper fiber. Among these, the intrinsic Q factor ( $Q_0$ ) is the most commonly cited measure of optical performance of microresonators.

### 2.3.1 Intrinsic material loss ( $Q_{mat}$ )

The microcavities discussed in this thesis are made of silica, which has a large transparency window including the visible and near infrared wavelengths. It exhibits very low absorption losses. For fused silica with very low  $OH^-$ , at its maximum transmission ( $\lambda = 1550$  nm), the intrinsic attenuation loss is  $\alpha = 0.2$  dB/km, which includes intrinsic absorption and Rayleigh scattering in silica. If translated into a material-absorption-limited Q, it would be

$$Q_{mat} = \frac{2\pi n}{\lambda \alpha} \approx 1.3 \times 10^{11} \quad (2.13)$$

However, this value is significantly higher than any Q factor achieved experimentally. Other loss mechanisms set practical limitations on Q factor in applications.

### 2.3.2 Surface scattering loss ( $Q_{ss}$ )

For most of the work presented here, surface roughness scattering has set a natural limitation on Q factor. It results from surface scattering induced by the roughness of the cavity surface. It is often modeled by index perturbations,  $\delta\epsilon$ , on the etched sidewall surfaces [29–32].

These index perturbations are sourced approximately by the unperturbed field solutions  $\vec{E}^0$  to create polarization currents

$$\vec{J} = i\omega\delta\epsilon\vec{E}^0 \quad (2.14)$$

where  $\delta\epsilon$  is the index perturbation and  $\omega$  is the angular frequency of the light. The polarization currents drive new electromagnetic fields which radiate into space. Optical losses due to the perturbations can be calculated from the far-field solutions set up by  $\vec{J}$ . From this, the far-field radiation as well as the corresponding loss can be evaluated. Assuming that the roughness profiles at top, bottom, and sidewall interfaces are mutually uncorrelated, the scattering loss  $\alpha_{sc}$  is given by [29, 30]

$$\alpha_{sc} = \sum_{interface} \oint (\vec{S}_i \cdot \vec{r}) \tilde{C}(\beta - n_1 k_0) dS \quad (2.15)$$

where  $\vec{S}_i$  is the Poynting vector generated by the equivalent volume density,  $\beta$  is the propagation constant,  $k_0$  is the wave number, and  $\tilde{C}$  is the Fourier transform of the autocorrelation function of the surface roughness profile.

### 2.3.3 Surface absorption loss ( $Q_{sa}$ )

Surface absorption loss in the microresonators is predominated from a water layer [33]. Although the thermal oxide layer is annealed at high temperature, residual  $OH^-$  can remain and cause significant loss in microresonators. Meanwhile, since normal air has 20–30% relative humidity, water adsorption onto microresonators tested in air is unavoidable. Near infrared light excites vibration of the rotational symmetry of the  $OH^-$  group inside the silica. Gorodetsky demonstrates that water adsorption onto the surface of a 750  $\mu\text{m}$  diameter microsphere causes a reduction in cavity Q [12]. Immediately after the microsphere is fabricated, a fast decrease of the cavity lifetime is observed within two minutes. The intrinsic Q of the microsphere drops from  $8 \times 10^9$  to  $1 \times 10^9$  within an hour. The optical Q can be partially recovered by baking at  $400^\circ\text{C}$ , indicating that water adsorption onto the microsphere surface is the source of limitation for maximum Q in microresonators. Meanwhile, it remains clear that etching locally damages the lattice allowing for the incorporation of various lattice impurities and defects.

Suppose the local surface absorption coefficient to be  $\gamma_{sa}(\vec{r})$ , the absorption energy is

$$\Delta W_{sa} = \int \gamma_{sa}(\vec{r}) \epsilon(\vec{r}) |\vec{E}(\vec{r})|^2 dV \quad (2.16)$$

It is a common practice to approximate  $\gamma_{sa}(\vec{r})$  to be assume that the loss rate is a constant in a reconstruction depth  $\zeta$  and zero elsewhere. Further assuming that  $\zeta$  is much smaller than the decay length of electrical field.

$$\Delta W_{sa} = \gamma_{sa} \zeta \int_s \epsilon(\vec{r}) |E(\vec{r})|^2 ds \quad (2.17)$$

where the integration covers the entire surface of the resonator. We can write the surface-absorption quality factor

$$Q_{sa} = \frac{4\pi \int \epsilon(\vec{r}) |\vec{E}(\vec{r})|^2 dV}{\lambda_0 \gamma_{sa} \zeta \int_s \epsilon(\vec{r}) |\vec{E}(\vec{r})|^2 ds} = \frac{4\pi V \max [\epsilon(\vec{r}) |\vec{E}(\vec{r})|^2]}{\lambda_0 \gamma_{sa} \zeta \int_s \epsilon(\vec{r}) |\vec{E}(\vec{r})|^2 ds} = \frac{4\pi V}{\lambda_0 \gamma_{sa} \zeta} \frac{1}{\int_s u(\vec{r}) ds} \quad (2.18)$$

where the dimensionless energy density is defined as

$$u(\mathbf{r}) = \frac{\epsilon(\vec{r}) |\vec{E}(\vec{r})|^2}{\max [\epsilon(\vec{r}) |\vec{E}(\vec{r})|^2]} \quad (2.19)$$

A scale argument gives that

$$V \sim R^3, \quad \int_s u(\vec{r}) ds \sim R^2 \quad \Rightarrow \quad Q_{sa} = \frac{4\pi V}{\lambda_0 \gamma_{sa} \zeta} \frac{1}{\int_s u(\vec{r}) ds} \sim R \quad (2.20)$$

### 2.3.4 Whispering gallery loss ( $Q_{wgm}$ )

In whispering-gallery optical resonators, the optical modes are confined by total internal reflection (TIR) at the silica-air interface, during which lightwave is reflected at an angle below the TIR critical angle will be perfectly reflected without loss. Yet, TIR on a curved interface is not perfect, and leads transmitted wave. Strictly speaking, total internal reflection does not take place at a curved boundary between two distinct media, and light inside a whispering gallery resonator cannot be perfectly trapped, even in theoretically ideal conditions. This loss mechanism is called whispering-gallery loss, and is due to tunneling of the photons out of their bound states [34]. The fraction of photons that are able to tunnel out of the bound state of the WGM is dependent on the cavity radius and decreases

exponentially as a function of the resonators' diameter. The WGM limited Q is greater than  $10^{13}$  resonators with major diameters ( $D$ ) of  $50 \mu m$  or larger.

## 2.4 Mode volume

Besides the temporal confinement of light manifested itself through quality factors, the microresonators also realize the spatial confinement of light, which is crucial for various applications [4]. The most common used characterization of light is mode volume, which is defined as the mode occupies if the energy density was distributed evenly inside cavity at the peak value

$$V_{eff} = \frac{\int_V \epsilon(\vec{r}) |\vec{E}(\vec{r})|^2 dV}{\max(\epsilon(\vec{r}) |\vec{E}(\vec{r})|^2)} \quad (2.21)$$

where the integral is evaluated over all space, and also includes evanescent field.

## 2.5 Tapered fiber coupling

Because of phase mismatch, free-space excitation of the whispering-gallery modes in microresonator is extremely inefficient. Instead, efficient excitation can be achieved using the evanescent coupling. One of these techniques utilizes tapered optical fibers to efficient and controllable excite the ultrahigh-Q whispering gallery modes, with negligible parasitic loss [35, 36].

### 2.5.1 Tapered fiber fabrication

A straight fiber taper is made by pulling a standard single-mode fiber (SMF) at a constant speed over a hydrogen flame. The SMF is firstly mounted on a stage that holds the fiber. Then the hydrogen flame is ignited and two computerized motor will pull each end of the fiber to opposite direction. As the fiber heats up and melts, its diameter is adiabatically reduced until the desired diameter is reached, usually  $1-2 \mu m$ . The taper length and final diameter are controlled by adjusting the gas flow rate, the pulling speed, and the flame location. Single-mode tapers can be fabricated with extremely low transmission losses ( $> 95\%$  transmission), enabling efficient and ideal coupling to ultrahigh-Q microresonators.

### 2.5.2 Characterization of tapered fiber

After the pulling process, the tapered fiber can be modeled as an air-clad cylinder waveguide. The optical modes of a step-index cylindrical fiber, described by a core radius  $a$ , core refractive index  $n_1$ , and cladding index  $n$  is well studied [37]. Specifically, the propagation constant of each optical mode is given by  $\beta$ , where is determined from the transcendental equation

$$\left( \frac{J'_l(ha)}{haJ_l(ha)} + \frac{K'_l(qa)}{qaK_l(qa)} \right) \left( \frac{n_1^2 J'_l(ha)}{haJ_l(ha)} + \frac{n_2^2 K'_l(qa)}{qaK_l(qa)} \right) = \left( \frac{l\beta}{k} \right)^2 \left( \frac{1}{(qa)^2} + \frac{1}{(ha)^2} \right)^2 \quad (2.22)$$

where

$$\begin{aligned} q^2 &= \beta^2 - n_2^2 k^2 \\ h^2 &= n_1^2 k^2 - \beta^2 \end{aligned}$$

Solution of this equation results in a family of discrete propagation constants for the guided modes of the waveguide. Each modes is described by a set of three quantum numbers  $(l; m; p)$ , where  $l$  is equivalent to an angular quantum number,  $m$  is a radial quantum number, and  $p$  is a polarization. The lowest-order one is the  $HE_{11}$  mode. The effect coupling between tapered fiber and waveguide requires phase matching between the mode index of them. In the experiment, it is achieved by changing the diameter of tapered fiber. In particular, the fiber taper is pulled to a minimum diameter and the taper position is adjusted with respect to the resonator until the phase matched diameter is found.

### 2.5.3 Coupling-of-modes formalism

It is evident that the efficient coupling can be achieved with two conditions, phase matching and significant overlap of two modes of resonator and waveguide. Let  $a(t)$  be the field amplitude of a circulating mode of whispering-gallery-mode resonator. Let  $B_k$  be the slowly varying amplitude of pump mode  $k$  ( $1 \leq k \leq N$ ) and assuming the coupling between different modes is negligible. The coupler is modeled in the following fashion. After undergoing the coupler, the  $T_k$  of the mode  $k$  will be coupled and  $R_k$  of it could transmitted through.

By energy conservation, it follows

$$R_k^2 = 1 - T_k^2 \quad (2.23)$$

In the limit of  $1 - R \ll 1$  (*i.e.*, small coupling region), we obtain

$$R = \sum_k R_k \approx 1 - \sum_k \frac{T_k^2}{2} = 1 - \frac{T^2}{2} \quad (2.24)$$

We then have the equations for the mode amplitude [38]

$$a(t) = i \sum_k T_k B_k^{in}(t) + R \cdot a(t - \tau_0) \exp(i2nkL - \frac{\alpha L}{2}) \quad (2.25)$$

$$B_k^{out}(t) = R_k B_k^{in}(t) + iT_k a(t) \quad (2.26)$$

where  $\tau_0 = nL/c = 2\pi nr/c$  is the circulation time of the resonator and  $\alpha$  is the linear power attenuation rate. If the propagation losses is small, for a single-mode coupler, by expanding  $a(t - \tau_0) = a(t) - \tau_0 \frac{da(t)}{dt}$  and using the near resonance condition  $nL = m\lambda_0$  with  $m$  being an integer, we have

$$\begin{aligned} & R \cdot a(t - \tau_0) \exp(i2nkL - \frac{\alpha L}{2}) \\ & \approx a(t) - \tau_0 \frac{da(t)}{dt} - (1 - R)a(t) - \frac{\alpha L}{2} a(t) - inL \frac{\Delta\omega}{c} a(t) \end{aligned} \quad (2.27)$$

It then gives

$$\frac{da}{dt} = -i\Delta\omega a - (\delta_0 + \delta_c)a + iCB_k \quad (2.28)$$

where

$$\delta_0 = \frac{\alpha c}{2n_s}, \quad \delta_c = \frac{1 - R}{\tau_0}, \quad C = \frac{T}{\tau_0} \quad (2.29)$$

Herein, the term  $\delta_0$  comes from the intrinsic quality factor  $Q_0 = \frac{2\pi n}{\alpha\lambda}$ ;  $\delta_c$  describes the coupling. The relation between them defines coupling efficiency. In the limit of small

coupling region ( $1 - R \approx T^2/2$ ). The stationary solution of Eq.(2.29) gives

$$a_0 = \frac{iB_k}{\delta_0 + \delta_c + i\Delta\omega} \sqrt{\frac{2\delta_c}{\tau_0}} \quad (2.30)$$

and the total output intensity has a Lorentzian shape

$$(B_k^{out})^2 = (B_k^{in})^2 \left[ 1 - \frac{4\delta_c\delta_0}{(\delta_c + \delta_0)^2 + (\Delta\omega)^2} \right] \quad (2.31)$$

If  $\delta_0 = \delta_c$  the output intensity becomes zero at resonance. This regime is called critical coupling and complete power transfer of the optical power carried by the wave to the cavity mode occurs.

#### 2.5.4 Coupling coefficients and $Q_{ext}$ (the coupling quality factor)

We then aim to determine the coupling coefficient  $T$  of the coupler-resonator system. Denote the normalized transverse field pattern of resonator and waveguide by  $\langle E_{1,n}|$  and  $\langle E_{2,m}|$  with normalization condition

$$\frac{n}{2} \sqrt{\frac{\epsilon_0}{\mu_0}} \langle E_{i,n}| E_{i,m} \rangle = \delta_{mn}, \quad i = 1, 2 \quad (2.32)$$

where  $\epsilon_0$  and  $\mu_0$  are the permittivity and permeability of the free space, respectively. It follows, from the standard coupling mode theory, that the coupling coefficient at position  $z$  is given by [39]

$$C_{mn}(z) = -i\frac{\omega}{4} \langle E_{2,m}| \delta\epsilon | E_{1,n} \rangle = -i\frac{k}{4} \sqrt{\frac{\epsilon_0}{\mu_0}} \langle E_{2,m}| \delta(n^2) | E_{1,n} \rangle \quad (2.33)$$

where  $k$  is free-space wave number and  $\omega$  is the optical frequency. Alternatively, for computational simplicity in numerical simulation, if the normalization condition  $\langle E_{i,n}| E_{i,m} \rangle = \delta_{mn}$  is chosen. We have

$$C_{mn}(z) = -i\frac{k}{2n} \langle E_{2,m}| \delta(n^2) | E_{1,n} \rangle \quad (2.34)$$

The derivation of this coupling efficient is simple. The total fields in resonator and waveguide are the superposition of two field patterns

$$\langle E(x, y) | = a_1(z) \langle E_{1,n}(x, y) | + a_2(z) \langle E_{2,m}(x, y) | \quad (2.35)$$

By definition, the field  $\langle E_{1,n} |$  is the field in the absence of waveguide 2; the other words, the dielectric constant increase that produces the waveguide is “thought away”. The power transferred from resonator 1 to waveguide 2 is caused by the polarization current  $i\omega P_{21}$  produced in waveguide 2 by the resonator 1, within waveguide 2

$$i\omega P_{21} = i\omega(\epsilon_i - \epsilon)a_1 \langle E_{1,n} | \quad (2.36)$$

Note that only  $\epsilon_i = \epsilon$  appears because the polarization current  $i\omega\epsilon \langle E_{1,n} |$  flows in the absence of guide 2 and must be subtracted. The power transfer is

$$-\frac{1}{4} [a_2^* \langle E_{2,m} | i\omega | P_{21} \rangle + c.c.] = -\frac{1}{4} [i\omega a_1 a_2^* \langle E_{2,m} | (\epsilon_i - \epsilon) | E_{1,n} \rangle + c.c.] \quad (2.37)$$

Meanwhile, we have the coupling for the modes

$$\frac{d|a_2^2|}{dz} = C_{mn} a_1 a_2^* + c.c. \quad (2.38)$$

Comparison of above two equation yields the coupling efficient. For a high-Q optical resonator with a high loaded quality factor ( $Q_{ext} = \frac{\omega}{2\delta_c}$ ,  $T_k \ll 1$ ), the field amplitude  $a(t)$  changes insignificantly over the coupling zone and can therefore be assumed to be constant. We have the coupling coefficient between waveguide and resonator is

$$T = \int C_{mn}(z) \exp(i\Delta\beta z) dz \quad (2.39)$$

where  $\Delta\beta$  is the prorogation constant mismatch between resonator and waveguide and  $z$  is defined along the waveguide. The external coupling Q is, in general, defined as

$$Q_{ext} = \frac{\omega}{\tau_c} = \frac{\omega}{2\delta_c} \quad (2.40)$$

where  $\tau_c$  and  $\delta_c$  are the time constant power decay and field decay, respectively. It can be connected to the coupling coefficient  $T$  via

$$\delta_c = \frac{T^2}{2\tau_0} \quad (2.41)$$

Therefore, we have

$$\begin{aligned} Q_{ext} &= \frac{\omega\tau_0}{T_0^2} = \omega \frac{2\pi Rn}{c} \frac{1}{T^2} \\ &= \omega \frac{2\pi Rn}{c} \left| \int -i\frac{\omega}{4} \langle E_{2,m} | \delta\epsilon | E_{1,n} \rangle \exp(i\Delta\beta z) dz \right|^{-2} \end{aligned} \quad (2.42)$$

## 2.6 Summary

In this chapter, we discussed the basis of the ultrahigh-Q optical microresonators. These cavities feature high quality factor, are already indispensable for a wide range of applications and studies such as novel nonlinear source, biodetection, the cavity QED to name just a few [4]. The various sources of optical loss in optical cavities are discussed. Two different approaches to measure the quality factor were described.

We also described the tapered fiber coupling to the optical cavities and introduce the couple-of-modes formalism to model the coupler-resonator system.

## Chapter 3

# Thermal Stress in Silica-on-Silicon Wedge Resonators

### 3.1 Introduction

For the past few decades, numerous experimental and theoretical studies have considered stress behavior and its impact on devices [40–42]. In the silicon system, the oxide silica is grown at temperatures near  $1000^{\circ}\text{C}$ . Upon cooling to room temperature, the difference between the thermal expansion coefficients of the silica and silicon causes a well-known compressive stress in the oxide. While this stress typically does not cause yield, reliability or performance issues in photonic devices, certain whispering gallery style optical resonators and waveguides rely upon undercut of the oxide to create optical confinement [3,10,26]. The undercut silica layer creates an air-cladding to guide the light (Fig.3.1(a)), and if there is sufficient thermal-induced stress, then this thin air-cladding silica layer may buckle and form crown-like patterns. Understanding the buckling behavior is important in optimizing the device performance. Specifically, oxide undercuts must be deep enough in these structures to isolate the optical mode from the silicon support pillar, however, the crowning behavior can occur at a critical undercut value and thereby interfere with optical performance. Likewise, in MEMS systems with free standing structures, residual stress can physically warp devices to a degree that renders them no longer useful [43,44]. In this chapter, we measure the buckling behavior of silica disks structures and compare with two models so as to create design guidelines that eliminate buckling in both resonator and waveguide structures. Specifically, by proper selection of oxide thickness and undercut, excellent optical performance is obtained (over 800 million optical quality factor for disk resonator structures

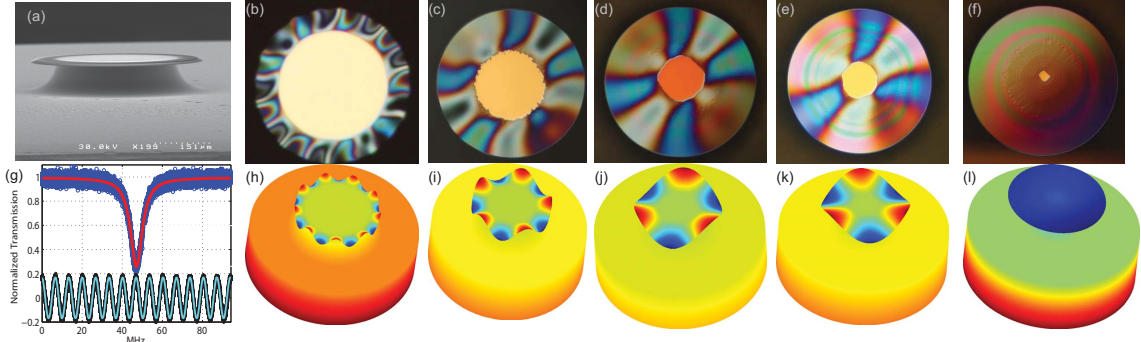


Figure 3.1: **(a)** SEM image of an unbuckled silica disk (500  $\mu\text{m}$  diameter and 2  $\mu\text{m}$  oxide thickness) resonator on a silicon pillar. The undercut is about 55  $\mu\text{m}$ . **(b)**–**(f)** Top-view microscope images of resonators (500  $\mu\text{m}$  diameter and 2  $\mu\text{m}$  oxide thickness) with different buckled oxide configurations. The undercuts of these devices are 70  $\mu\text{m}$ , 120  $\mu\text{m}$ , 155  $\mu\text{m}$ , 185  $\mu\text{m}$ , and 225  $\mu\text{m}$ , respectively. **(g)** Spectral scan for the resonator in panel (a). The measured linewidth corresponds to an optical Q factor of 37 million. The red curve gives a Lorentzian fitting of the experimental transmission and the cyan line shows a sinusoidal fitting of the interferometer output. **(h)**–**(i)** Finite element simulation results of resonators (500  $\mu\text{m}$  diameter and 2  $\mu\text{m}$  oxide thickness) showing different buckling configurations. The undercut of these devices matches those in the panels (b)–(f).

of 7.5 mm diameter and 10  $\mu\text{m}$  oxide thickness (see **Chapter 4**) [26]).

## 3.2 Experimental results

Earlier work on silica wedge-shaped resonators achieved Q factors as high as 50 million [9] in devices with diameters around 100  $\mu\text{m}$ . Those structures featured a lithographically-defined oxide disk of 2  $\mu\text{m}$  thickness that had been partially undercut using the silicon selective etchant xenon difluoride. The ability to extend both the Q factor and the resonator diameter to larger values (Q greater than 100 million and resonator diameter to the mm-cm size range) is important for applications such as microcombs and rotation sensing [5, 14]. However, due to thermal stress, simply scaling the previous device to larger diameters fails to provide satisfactory performance. Figure 3.1(b) shows a top view (interference contrast mode) image of a silica wedge resonator having 500  $\mu\text{m}$  diameter and 2  $\mu\text{m}$  oxide thickness. With about 70  $\mu\text{m}$  undercutting of the silicon, the silica layer starts to buckle and features a crown-like pattern. Further, the number of nodes in the buckled pattern decreases with the deepness of the undercut. For example, as shown in Fig. 3.1(b)–(e), the number of

nodes in the buckled structures are 18, 10, 8, and 6 for 70  $\mu\text{m}$ , 120  $\mu\text{m}$ , 155  $\mu\text{m}$ , and 180  $\mu\text{m}$  undercuts. Ultimately, if the undercut is deep enough, the resonator will return to the unbuckled configuration (Fig. 3.1(f)).

To assess the impact of buckling on the optical performance of the resonators, the intrinsic optical Q factor [4] of normal and buckled samples is measured. Devices were coupled to an optical fiber using a fiber taper [45, 46], and spectral lineshape data were obtained by tuning an external-cavity semiconductor laser (1,550 nm) across an optical resonance while monitoring transmission on an oscilloscope (see sample scan in Fig. 3.1(g)). To accurately calibrate the laser scan in this measurement, a portion of the laser output was also monitored after transmission through a calibrated Mach-Zehnder interferometer having a free spectral range of 6.72 MHz. The buckled resonators (Fig. 3.1(b)–(e)) show low Q factors, typically below 1 million. Moreover, some of these samples were observed to crack over a period of a few days. In contrast, an unbuckled 500  $\mu\text{m}$  diameter resonator with 2  $\mu\text{m}$  thickness (corresponding to an undercut of 55  $\mu\text{m}$  in Fig. 3.1(a)) featured a 38 million Q factor and this Q-factor performance was preserved for more than one year. The spectral scan for this resonator is shown in Fig. 3.1(g).

### 3.3 Finite element model

To model thermal stress, we take the difference between oxide growth temperature (1000°C) and the simulation temperature as a control parameter ( $\Delta T$ ) and simulate the equilibrium state of the resonator via a finite element model in COMSOL Multiphysics (<http://www.comsol.com/>). The following is defined as an order parameter,

$$\Omega = \frac{1}{V} \iiint_{\text{silica}} \sqrt{\left(\frac{\partial w}{\partial x}\right)^2 + \left(\frac{\partial w}{\partial y}\right)^2} dV \quad (3.1)$$

where  $w$  is the vertical component of deformation due to thermal stress,  $V$  is the volume of silica and integration is carried over the whole silica layer. The order parameter is a simple measure of the irregularity of the silica induced by the stress. Figure 3.2 is a plot of the numerically simulated order parameter plotted versus  $\Delta T$ . The plot shows a second-order phase transition behavior as  $\Delta T$  increases in a resonator of diameter 500  $\mu\text{m}$ , silica layer

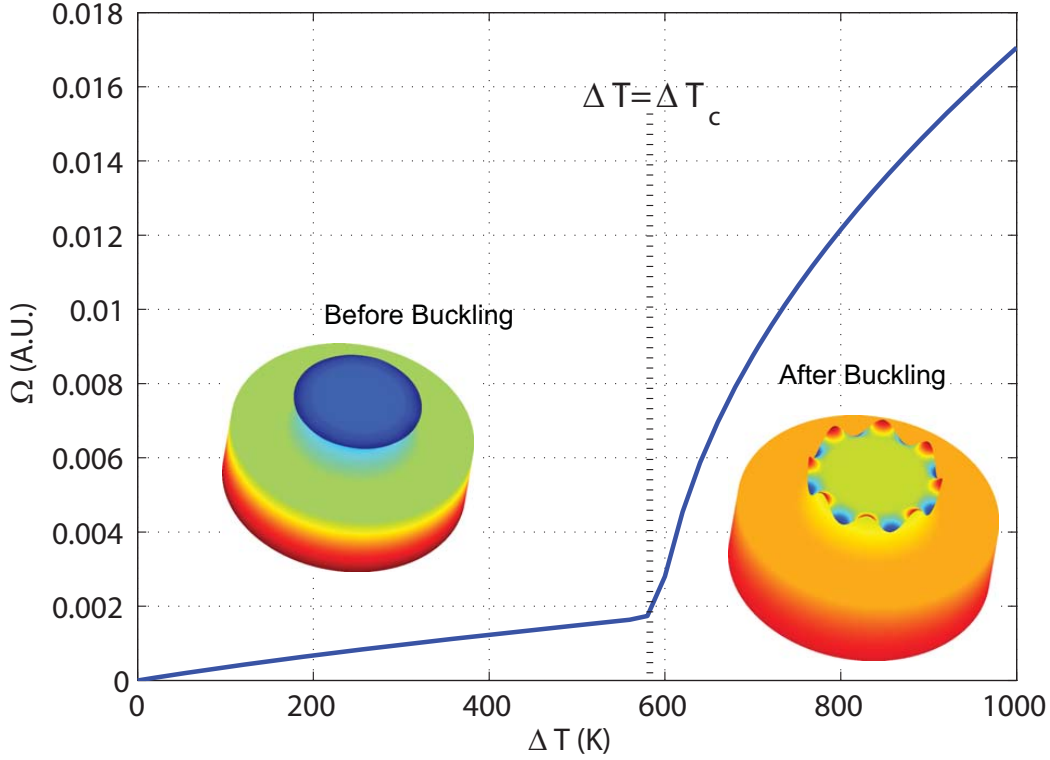


Figure 3.2: Plot of the order parameter (Eq. (3.1)) versus the change in temperature relative to the growth temperature. A second-order phase transition is apparent at a critical temperature difference ( $\Delta T_c$ ). Above this value, the disk buckles and features a crown pattern with several nodes. On the other hand, the silica layer bends uniformly down when  $\Delta T$  is smaller than the critical value. In this FEM simulation, the resonator has diameter  $500 \mu\text{m}$ , thickness  $2 \mu\text{m}$ , and undercut  $70 \mu\text{m}$ .

thickness  $2 \mu\text{m}$  and undercut of  $70 \mu\text{m}$ . Above a critical temperature difference ( $\Delta T_c$ ), the silica layer buckles and features a crown-like pattern with 16 nodes. In contrast, the silica layer bends uniformly downward when  $\Delta T$  is smaller than the critical value. Since the silica is grown at  $1000^\circ\text{C}$ , the equilibrium state of this resonator at room temperature will have a buckled pattern.

The equilibria of resonators with differing amounts of undercut were also calculated for comparison with the measurements in Fig. 3.1 (see Fig. 3.1(h)–(i)). Ultimately, if the undercut is deep enough, the silica layer will uniformly bend downward. The simulated configurations have 16, 10, 6 and 6 nodes for  $70 \mu\text{m}$ ,  $120 \mu\text{m}$ ,  $155 \mu\text{m}$ , and  $180 \mu\text{m}$  undercuts and are more or less consistent with measurements. The discrepancy might result from the slight irregularity in the etched silicon pillar.

To further understand the impact of thermal stress in silica/silicon system and validate our finite element model, a “bridge” structure consisting of two microdisks connecting by a cantilever of length 1 mm and width  $2\ \mu\text{m}$  is patterned and fabricated on a silica-on-silicon wafer (Fig. 3.3). It is the most common technique for measuring the thermal stress by measuring the deflection of a long, narrow, and thin beam or cantilever. Because of the smaller thermal expansion coefficient of silica, the beam will try to expand and finally buckle up. The measured out-of-plane deflection ( $(43 \pm 4)\ \mu\text{m}$ ) of the cantilever from SEM picture is a good agreement with predicted value ( $46.1\ \mu\text{m}$ ) from a finite element model.

### 3.4 Analytic model

In addition to the finite element analysis, an analytic model was studied to provide guidance on device design. The approach is based on a two-dimensional buckling model of the annular disk and the energy method. The energy model employed is especially useful when a rigorous solution of the Kirchhoff equation is unknown or it is required to find only an approximate value of the critical temperature difference for buckling [47–49]. Basically, if the work done by thermal stress is smaller than the strain energy of bending for every possible shape of buckling, then the unbuckled equilibrium is stable. If the same work becomes larger than the energy of bending for any shape of deformation, then the structure tends to be unstable and starts buckling. In a silica disk resonator with radius  $b$ , thickness  $t$  and for a silicon pillar of radius  $a$ , the buckling shape can be approximated by a sine curve along the circumference of a plate [50, 51]. Assume that the deflection of the annular disk in the vertical direction is

$$w = C(r - a)^2 \cos(n\theta) \quad (3.2)$$

where  $C$  is the amplitude of buckling,  $2n$  is the number of nodes in the crown-like pattern and the deflection obeys the clamped boundary condition at  $r = a$ . With respect to a polar coordinate system  $(r, \theta)$  with origin at the center, the components of stress induced by the

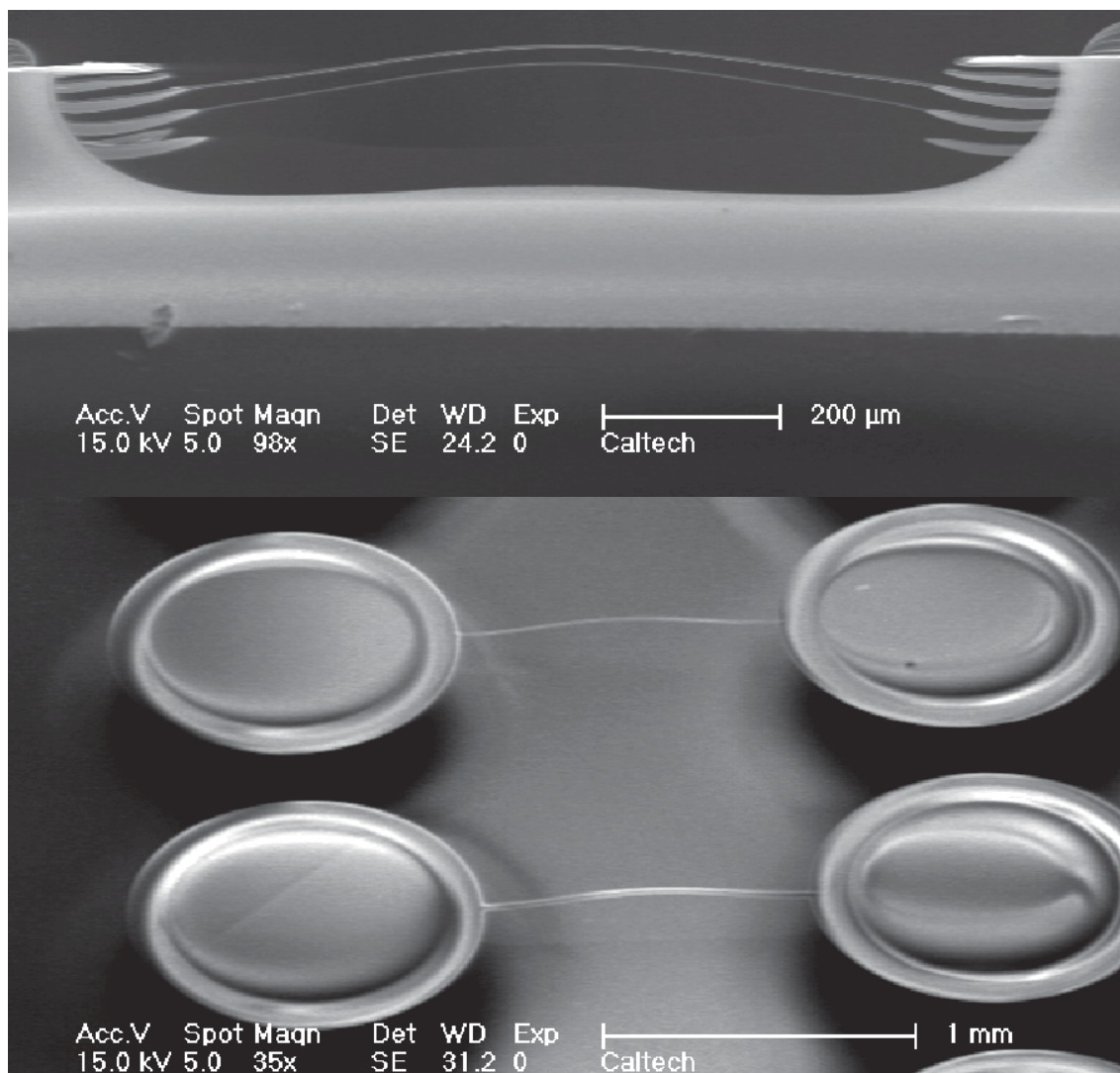


Figure 3.3: An SEM image of top (upper panel) and side (lower panel) view of silica bridge fabricated on a silicon chip. Due to the thermal stress, the bridge bends up. The cantilever has length of 1 mm and width from  $2\ \mu\text{m}$  to  $12\ \mu\text{m}$ . The measured vertical deflection ( $43\ \mu\text{m}$ ) agrees with the simulation result ( $46.1\ \mu\text{m}$ ).

thermal expansion mismatch are [52]

$$\sigma_r(r) = \frac{b^2 - a^2}{a^2(\frac{b^2}{r^2} - 1)}\sigma \quad (3.3)$$

$$\sigma_\theta(r) = -\frac{b^2 - a^2}{a^2(\frac{b^2}{r^2} + 1)}\sigma \quad (3.4)$$

where

$$\sigma = \frac{\Delta\alpha \cdot \Delta T}{\frac{1-\nu_{Si}}{E_{Si}} + \frac{1}{E_{SiO_2}} \left( \frac{1+\rho^2}{1-\rho^2} \right) + \frac{\nu_{SiO_2}}{E_{SiO_2}}} \quad (3.5)$$

$$= \Delta\alpha \cdot \Delta T \cdot h(\rho) \quad (3.6)$$

and where  $\rho = a/b$ ,  $\nu_{Si}$  and  $\nu_{SiO_2}$  are the Young's moduli of silicon and silica;  $E_{Si}$  and  $E_{SiO_2}$  are the Poisson's ratio of silicon and silica;  $\Delta\alpha$  is the difference of the thermal expansion coefficients;  $\Delta T$  is the temperature difference between oxidation growth temperature and room temperature. For clarity, we defined that  $h(\rho) = \frac{1}{\frac{1-\nu_{Si}}{E_{Si}} + \frac{1}{E_{SiO_2}} \left( \frac{1+\rho^2}{1-\rho^2} \right) + \frac{\nu_{SiO_2}}{E_{SiO_2}}}$ . The bending energy is [47] ( $\nu = \nu_{SiO_2}$ ,  $D = \frac{E_{SiO_2} t^3}{12(1-\nu_{SiO_2}^2)}$ )

$$\begin{aligned} U = & \iint r dr d\theta \left[ \frac{D}{2} \left( \frac{\partial^2 w}{\partial r^2} + \frac{1}{r} \frac{\partial w}{\partial r} + \frac{1}{r^2} \frac{\partial^2 w}{\partial \theta^2} \right)^2 \right. \\ & - D(1-\nu) \frac{\partial^2 w}{\partial r^2} \left( \frac{1}{r} \frac{\partial w}{\partial r} + \frac{1}{r^2} \frac{\partial^2 w}{\partial \theta^2} \right) \\ & \left. + D(1-\nu) \left( \frac{1}{r} \frac{\partial^2 w}{\partial r \partial \theta} - \frac{1}{r^2} \frac{\partial w}{\partial \theta} \right)^2 \right] \quad (3.7) \end{aligned}$$

The work done by the silica layer forces during the buckling is found to be [47]

$$T = -\frac{1}{2} \iint r dr d\theta \left[ \sigma_r t \left( \frac{\partial w}{\partial r} \right)^2 + \sigma_\theta t \left( \frac{1}{r} \frac{\partial w}{\partial \theta} \right)^2 \right] \quad (3.8)$$

where  $t$  is the thickness of the silica layer. By equating  $U$  and  $T$ , the critical condition of buckling can be written as

$$\Delta T = \frac{2t^2 E_{SiO_2}}{b^2(1-\nu_{SiO_2}^2) \Delta\alpha h(\rho)} \cdot \frac{F(n, \rho)}{G(n, \rho)} \quad (3.9)$$

where

$$F(n, \rho) = (-1 + \rho) \times \left[ 8(1 + \nu)(-1 + \rho) + 2n^4(-1 + \nu)(1 + \rho)(1 + (-8 + \rho)\rho) - n^2(13 + 12\nu(-1 + 3\rho) + \rho(-43 + (-7 + \rho)\rho)) \right] + 4(-2 + 6n^4(-1 + \nu) + n^2(-9 + 6\nu))\rho^2 \log(\rho) \quad (3.10)$$

$$G(n, \rho) = \frac{\rho^2}{-1 + \rho^2} \times \left[ 4(3 + \rho(-16 + 12\rho + \rho^3)) - n^2(9 + \rho(-64 + 36\rho + 19\rho^3)) + 12\rho^2(-4 + n^2(6 + \rho^2)) \log(\rho) \right] \quad (3.11)$$

Figure 3.4 shows the relation between the normalized critical temperature difference ( $\Delta\alpha\Delta T b^2/t^2$ )

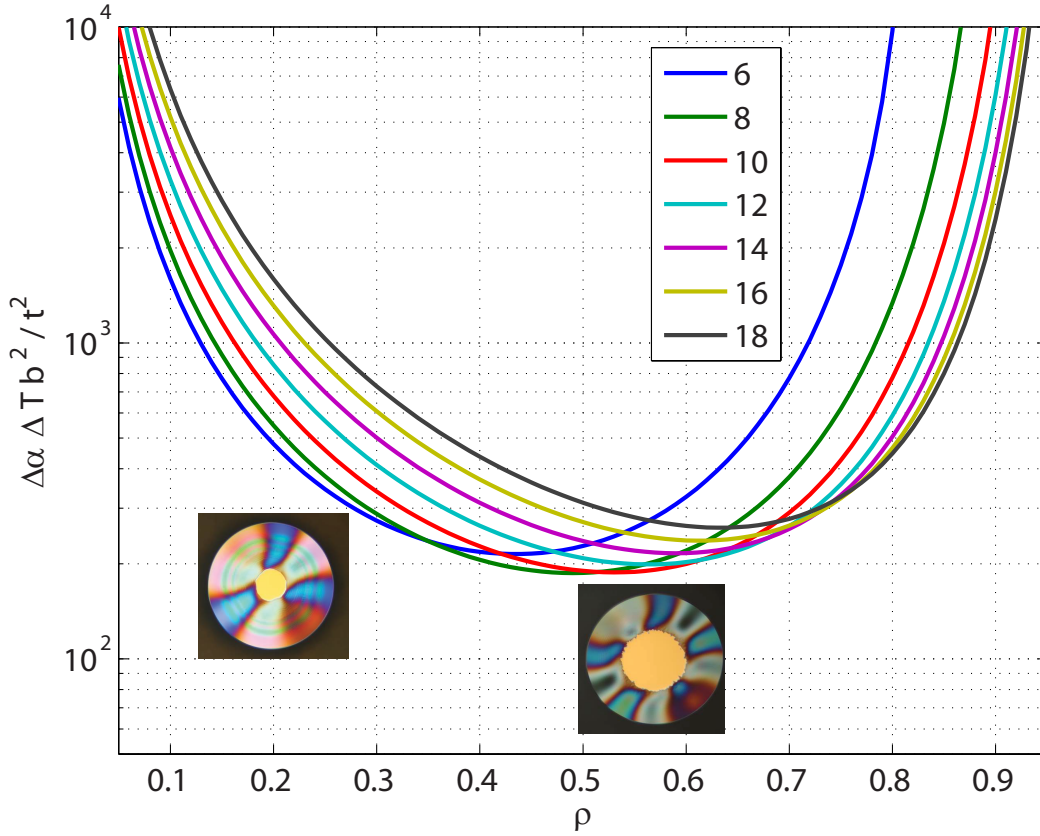


Figure 3.4: The relation between normalized critical temperature difference ( $\Delta\alpha\Delta T b^2/t^2$ ) and parameter  $\rho = a/b$  for configurations with different numbers of nodes (see legend) in the silica/silicon system. Insets show examples from experiments of the buckled configurations with  $\rho = 0.52$ , 10 nodes, and  $\rho = 0.26$ , 6 nodes (See Fig. 3.1).

and parameter  $\rho = a/b$  for configurations with different numbers of nodes in the silica/silicon disk system. The normalization used here provides a dimensionless parameter that characterizes the threshold of buckling. It also reflects the fact that critical temperature difference depends quadratically on the resonators' oxide thickness and inversely quadratically on their radius. At each  $\rho$ , the configuration with minimal critical temperature difference gives the equilibrium state after buckling. As the undercut goes deeper, the equilibrium buckled configuration will have fewer nodes. This result is consistent with both experimental observation and the finite element simulation. Further, the combination of these curves defines an envelope function that outlines the boundary between the unbuckled and buckled state (c.f. Fig. 3.2). It also explains the fact that the resonator has an unbuckled configuration for small silicon pillar (Fig. 3.1(g)).

The y-axis parameter in Fig. 3.4 shows that the critical temperature difference depends quadratically on the thickness of the silica layer. It implies that thicker oxides will avoid the buckling and maintain mechanical stability. Interestingly, optical performance, in particular the Q factor, also improves for thicker oxides. This can be understood to result because the optical field at the oxide-air interface is generally weaker for thicker oxide [26]. This reduces both surface absorption and scattering, thereby increasing the optical Q factor. From a design perspective, the undercut needs to be carefully controlled. On one hand, it must be deep enough to reduce optical loss due to the mode leakage into the silicon pillar. On the other hand, shallow undercut is more desirable to avoid buckling. Indeed, we have demonstrated elsewhere [26] that by increasing the oxide thickness to  $10\ \mu\text{m}$  and controlling the undercut to be approximately  $150\ \mu\text{m}$  it is possible to obtain a record Q factor on a chip of 875 million Q in a device that is mechanically stable (see **Chapter 4**).

To provide guidance to disk resonator design, we calculate the buckling threshold of undercut for different disk resonators having  $6\ \mu\text{m}$  and  $10\ \mu\text{m}$  oxide thickness. As shown in Fig. 3.5, for each given structure, there are two thresholds (lower and higher). If the undercut is smaller than the lower threshold or larger than the higher threshold, the resonator remains in the unbuckled configuration. In contrast, if the undercut is between these two thresholds, the resonator will buckle. (c.f. Fig. 3.1)

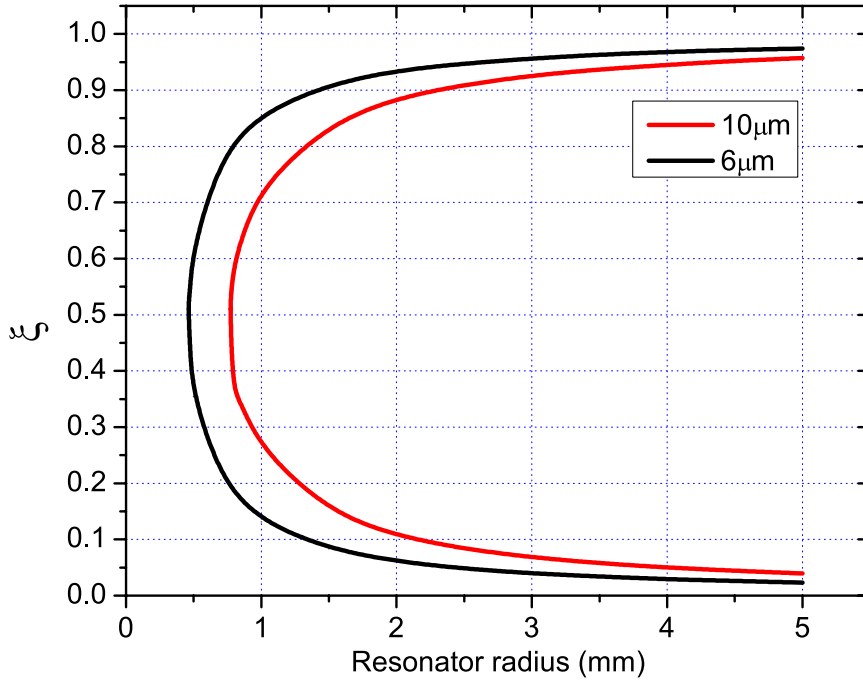


Figure 3.5: The threshold of undercut parameter ( $\xi = 1 - a/b$ ) for buckling. For each thickness, the left side of curve defines a region in which the disk resonators do not buckle.

### 3.5 Summary

In this chapter, we demonstrate and model the impact of the thermal stress in silica-on-silicon disk resonators. We provide both analytical and finite element simulation to understand buckling behavior and offer guidance on performance improvement. In particular, by proper design, stress does not limit the optical performance of these devices. Although we only discuss the particular case of the disk resonator, our analysis could be extended to guide the design of other structures.

## Chapter 4

# Chemically Etched Ultrahigh-Q Wedge Resonator

### 4.1 Introduction

Achieving long photon storage time (high-Q factor) in microcavities relies critically upon use of low absorption dielectrics and creation of very smooth (low scattering) dielectric interfaces. Figure 4.1 compares several current available high-Q-factor resonators. Although crystalline resonators currently provide the highest Q factors [53–55], in chip-compatible devices silica has by far the lowest intrinsic material loss. Microtoroid resonators combine this low material loss with a reflow technique in which surface tension is used to smooth lithographic and etch-related blemishes [10]. However, reflow smoothing makes it very challenging to fabricate larger-diameter ultrahigh-Q (UHQ) resonators or to leverage the full range of integration tools and devices available on silicon. Silicon-nitride microdisks, although flexible to integrate on chip, has relative low Q factors ( $5 \times 10^6$ ) [56]. The devices reported here attain UHQ performance using only conventional semiconductor processing methods on a silicon wafer. Moreover, the best Q performance occurs for diameters greater than  $500 \mu\text{m}$ , a size range that is difficult to access with microtoroids because of the limitations of the reflow process. Microcombs will benefit from a combination of UHQ and larger-diameter resonators (microwave-rate free spectral range, FSR) to create combs that are efficient in turn-on power and can be self-referenced [5]. Two further applications that can benefit from larger (1–50 mm diameter) UHQ resonators are integrated reference cavities and ring gyroscopes.

Excellent control of the free spectral range is also demonstrated here, opening the possi-

	Optical Q	Typical Size (diameter)		on-chip	Integration on chip	Size repeatability
		1 $\mu$ m	10 $\mu$ m			
CaF <sub>2</sub> resonator	10 <sup>11</sup>	[Bar chart showing size between 10 $\mu$ m and 1mm]		No	Not easy	Not easy
SiO <sub>2</sub> micro-sphere	10 <sup>10</sup>	[Bar chart showing size between 10 $\mu$ m and 1mm]		No	Not easy	No
SiO <sub>2</sub> micro-toroid	5x10 <sup>8</sup>	[Bar chart showing size between 10 $\mu$ m and 1mm]		Yes	Not easy	No
SiN <sub>x</sub> - based resonator	5x10 <sup>6</sup>	[Bar chart showing size between 10 $\mu$ m and 1mm]		Yes	Easy	Yes

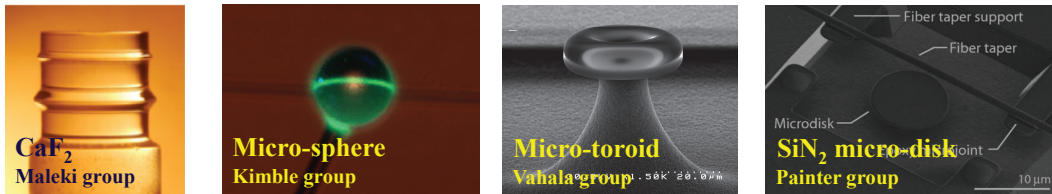


Figure 4.1: The comparisons among current available high-Q factor resonators.

bility of precision repetition rate control in microcombs or precision control of free spectral range. The latter is important in stimulated Brillouin lasers which have been recently demonstrated in ultrahigh-Q silica microspheres, in calcium fluoride resonators [57, 58] as well as in rib waveguide Fabry-Perot resonators [59]. As an application of this control, stimulated Brillouin lasers (SBLs) are demonstrated here using these new resonators. The devices feature very low threshold turn-on power, milliwatt-scale output power and very high coherence.

## 4.2 Device fabrication

Earlier work considered the Q factor in a wedge-shaped resonator fabricated of silica on a silicon wafer. Q factors as high as 50 million were obtained [9]. That approach isolated the mode from the lithographic blemishes near the outer rim of the resonator by using a shallow wedge angle. In the current work, we have boosted the optical Q by about 20X beyond these earlier results through a combination of process improvements. While the present devices resemble the earlier geometry [9], they derive ultrahigh-Q performance from overall

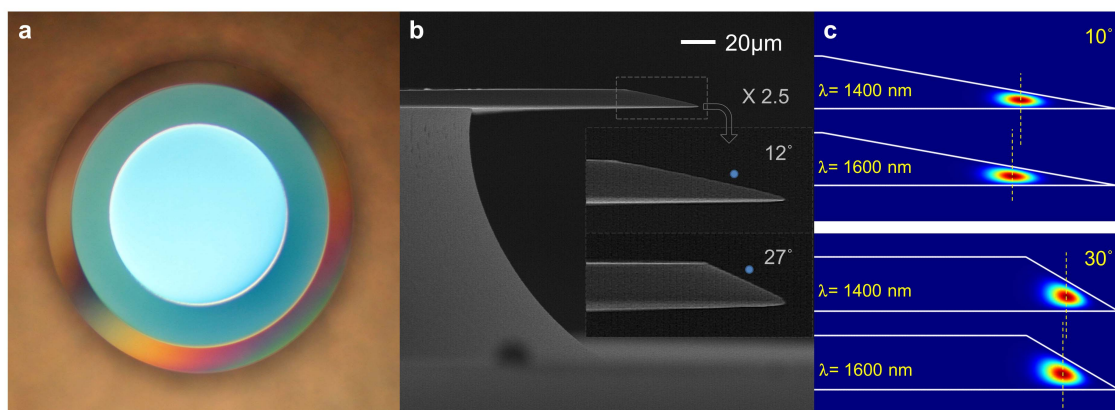


Figure 4.2: Micrographs and mode renderings of the wedge resonator from top and side views. **(a)** An optical micrograph shows a top view of a 1-mm-diameter wedge resonator. **(b)** A scanning electron micrograph shows the side-view of a resonator. The insets here give slightly magnified micrographs of resonators in which the wedge angle is 12 degrees (upper inset) and 27 degrees (lower inset). The small circle shows the approximate location of the taper during measurements. **(c)** A rendering shows calculated fundamental-mode intensity profiles in 10 degree and 30 degree wedge angle resonators at two wavelengths. As a guide, the center-of-motion of the mode is provided to illustrate how the wedge profile introduces normal dispersion that is larger for smaller wedge angles.

changes to the etch process and the oxide growth. Specifically, the physical principle at work in the earlier structures, a shallow wedge angle to provide roughness isolation, is no longer required. Indeed, and in contrast to earlier work, larger wedge angles are now desirable.

A top-view optical micrograph is provided in Fig. 4.2 to illustrate the basic geometry. The process flow begins with thermal oxide on silicon, followed by lithography and oxide etching with buffered hydrofluoric acid. In the insets to Fig. 4.2, scanning electron micrographs of devices featuring 12-degree and 27-degree wedge angles are imaged. Empirically, the angle can be controlled through adjustment of the photoresist adhesion using commercially available adhesion promoters. The oxide disk structures function as an etch mask for an isotropic dry etch of the silicon using  $\text{XeF}_2$ . During the dry etch, the silicon undercut is set so as to reduce coupling of the optical mode to the silicon support pillar. This value is typically set to about 100 microns for 1 mm diameter structures and over 150 microns for 7.5 mm diameter disks, however, smaller undercuts are possible while preserving ultrahigh-Q performance.

The fabrication process is outlined in Fig. 4.3. Disks were fabricated on (100) prime grade float zone silicon wafers. Photo-resist was patterned using a GCA 6300 stepper on

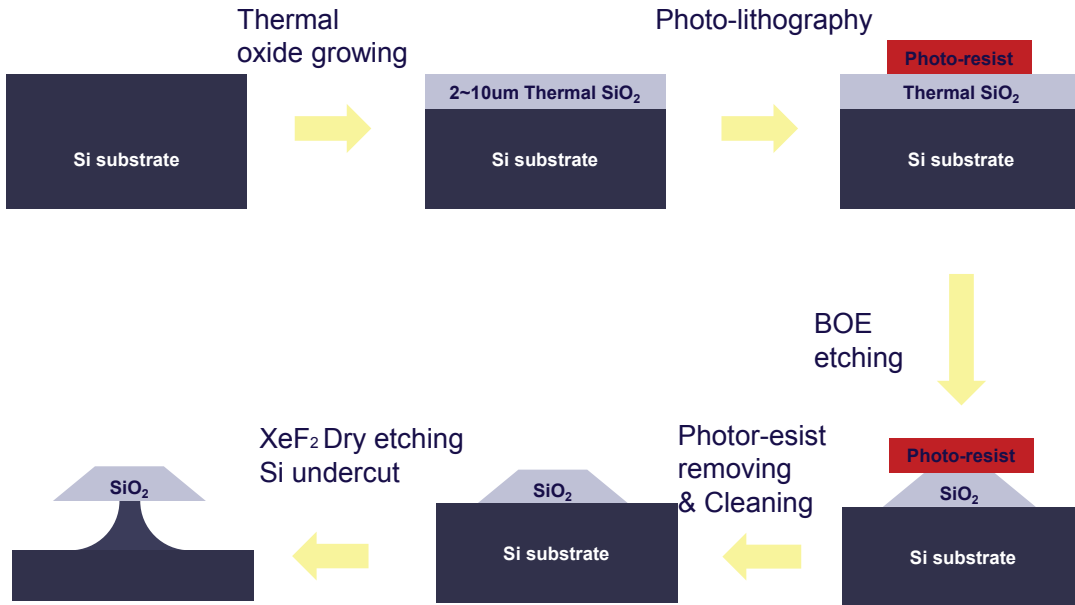


Figure 4.3: The fabrication procedure of disk resonators

thermally grown oxide of thickness in the range of 2 – 10 microns. Post exposure bake followed in order to cure the surface roughness of photo-resist pattern which acted as an etch mask during immersion in buffered hydrofluoric solution (Transene, buffer-HF improved). Careful examination of the wet etch revealed that the vertex formed by the lower oxide and upper surface contains an etch front that is distinct from that associated with the upper surface (see “foot” region in Fig. 4.4 inset). This region has a roughness level that is higher than any other surface and is a significant contributor to  $Q$  degradation. By extending the etch time beyond what is necessary to reach the silicon substrate, this foot region can be eliminated as shown in Fig. 4.4. With elimination of the foot etch front, the isotropic and uniform etching characteristic of buffered hydrofluoric solution results in oxide disks and waveguides having very smooth wedge-profiles which enhance  $Q$  factors. Additionally, the oxide used in these studies was prepared in such a way so as to reduce optical loss. While the oxide layers were prepared using a wet oxidation, it was found that a final dry oxidation step (24 hours) at  $1000^{\circ}\text{C}$  was required to reliably achieve the highest  $Q$  factors. This additional step is believed to drive down the water content in the silica oxide. After

the conventional cleaning process to remove photo-resist and organics, silicon was isotropically etched by xenon difluoride to create an air-cladding whispering gallery resonator. An atomic force microscope was used to measure the surface roughness of the three, silica-air dielectric surfaces. For the lower surface, the resonators were detached by first etching the silicon pillar to a few microns in diameter and then removing the resonator using tape. The r.m.s. roughness values on 10-degree wedge-angle devices are: 0.15 nm (upper), 0.46 nm (wedge), 0.70 nm (lower); and for 27-degree wedge-angle devices are: 0.15 nm (upper), 0.75 nm (wedge), 0.70 nm (lower). The correlation length is approximately a few hundred nm. The difference in the wedge surface roughness obtained for the large and small wedge-angle cases is not presently understood.

## 4.3 Device characterization

### 4.3.1 Optical Q-factor measurements

To measure intrinsic Q factor, devices were coupled to SMF-28 optical fiber using a fiber taper [45,46] and spectral lineshape data were obtained by tuning an external-cavity semiconductor laser across the resonance while monitoring transmission on an oscilloscope. The taper coupling could be adjusted so as to both over couple and under couple the resonator [46]. All measurements were performed in the 1500 nm band. To accurately calibrate the laser scan in this measurement, a portion of the laser output was also monitored after transmission through a calibrated Mach-Zehnder interferometer having a free spectral range of 7.75 MHz. The inset in Fig. 4.5 shows a spectral scan obtained on a device having a record Q factor of 875 million. In these measurements, the taper coupling was applied on the upper surface of the resonator near the center of the wedge region (see Fig. 4.2(b)). Modeling shows that the fundamental mode has its largest field amplitude in this region. Moreover, this mode is expected to feature the lowest overall scattering loss resulting from the three, dielectric-air interfaces as well as from the silicon support pillar. An additional test that can be performed to verify the fundamental mode is to measure the mode index by monitoring the free spectral range (FSR). The fundamental mode features the largest mode index and hence smallest FSR. To expedite the measurement of Q factor in these devices, an automated system was devised in which a broad spectral scan of the spectrum

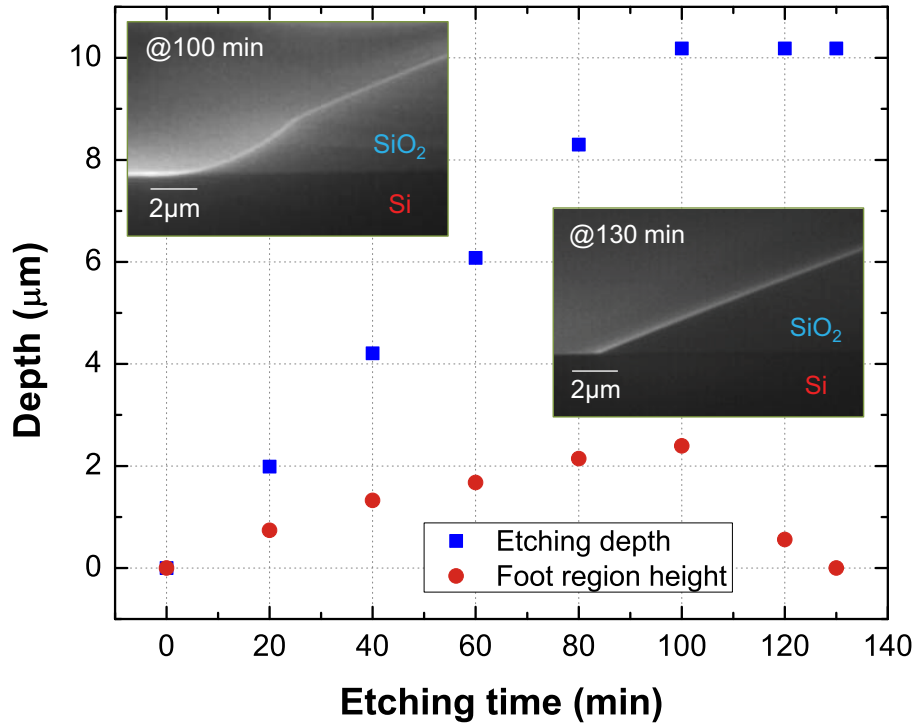


Figure 4.4: Data plot showing the effect of etch time on appearance of the “foot” region in etching of a 10- $\mu\text{m}$ -thick silica layer. The foot region is a separate etch front produced by wet etch of silica that is empirically observed to adversely affect the optical Q factor. The data show that by control of the etch time the “foot” region can be eliminated. The upper-left inset is an image of the foot region and the lower right inset shows the foot region eliminated by increase of the wet etch time.

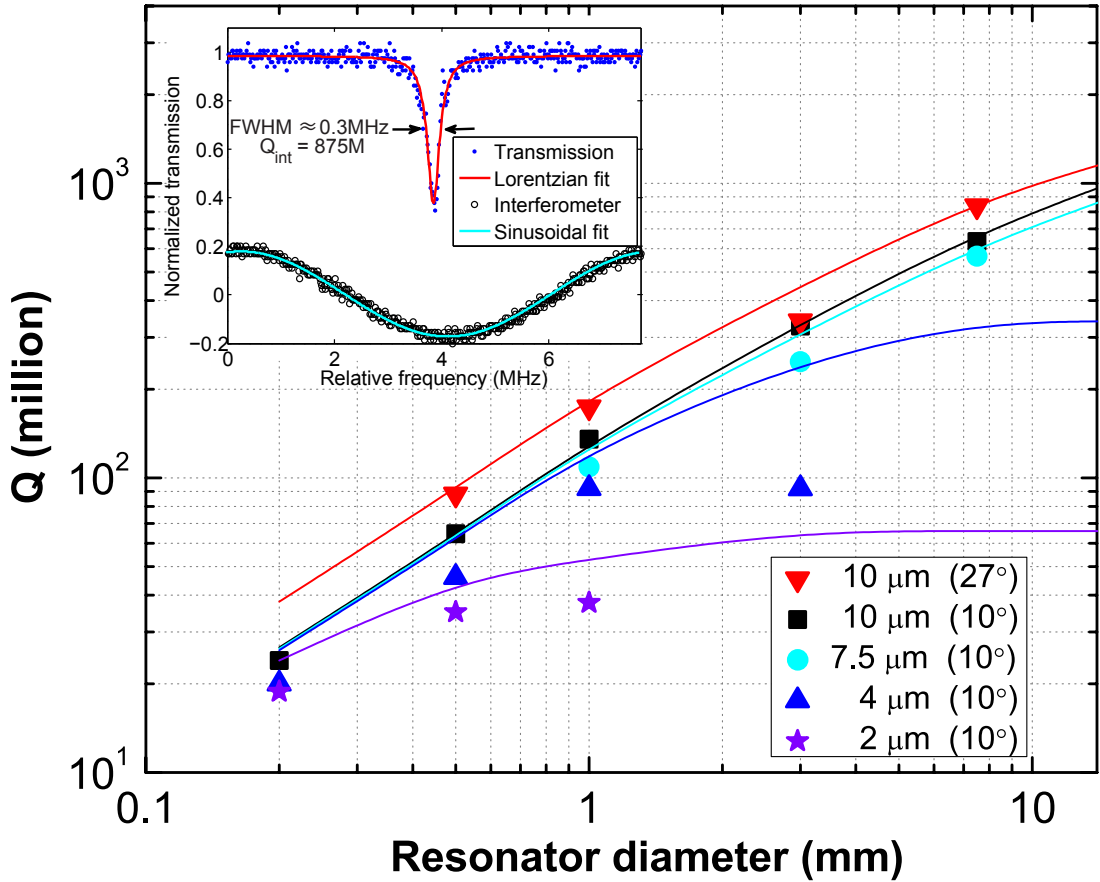


Figure 4.5: Data showing the measured Q factor plotted versus resonator diameter with oxide thickness as a parameter. Multiple devices were measured for each data point, however, the dispersion in Q values was typically low so that error bars are not shown and only the average Q value device is shown. For example, the average Q data (red points) are taken from the following set where each Q value represents a distinct device:  $D \approx 7.5$  mm,  $Q \approx 799$  M, 875 M;  $D \approx 3$  mm,  $Q \approx 326$  M, 331 M, 367 M;  $D \approx 1$  mm,  $Q \approx 169$  M, 174 M;  $D \approx 0.5$  mm,  $Q \approx 88$  M, 91 M. The solid lines show the predicted Q factor from a model that accounts for surface-roughness-induced scattering loss and also material loss (fitting gives a material Q of 2.5 billion). The r.m.s. roughness is measured using an AFM (see Methods section for values). The red data points correspond to a wedge angle of 27 degrees. All other data are obtained using a wedge angle of approximately 10 degrees. The inset shows a spectral scan for the case of a record Q factor of 875 million. In this spectrum, the resonator is undercoupled so that the linewidth is close to the intrinsic value. However, both critical coupling and strong over-coupling are also possible by adjusting the air gap between the taper and the resonator. The sinusoidal curve accompanying the spectrum is a calibration scan performed using a fiber interferometer.

(exceeding a full free spectral range) was performed and recorded onto a fast digital oscilloscope (1 GHz). Figure 4.6 provides a wide spectral scan of a resonator with a diameter

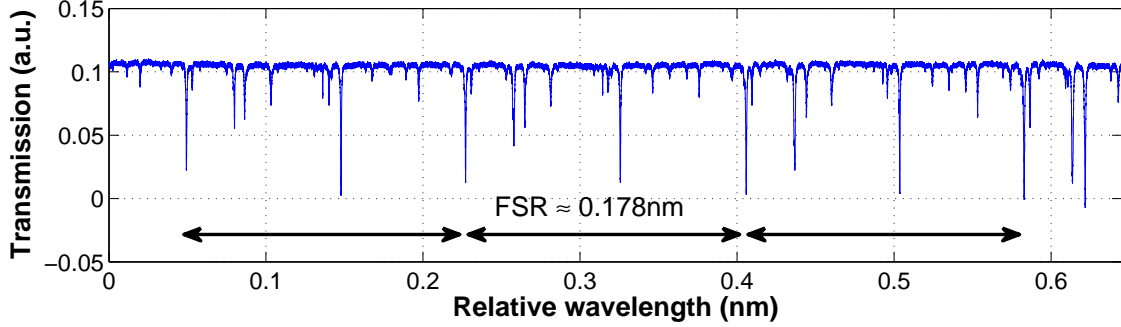


Figure 4.6: Broad spectral scan over 3 free spectral ranges (FSR) of a 3-mm-diameter resonator.

of 3 mm and a corresponding free spectral range (FSR) of approximately 0.178 nm. The scan includes 3 complete FSRs. The spectrum was then analyzed using a fitting algorithm that would identify and fit the resonator modes. This made possible rapid acquisition (and identification) of the highest Q mode. Spectra were taken in the undercoupled regime so as to obtain Q values closer to the intrinsic (unloaded) value. Finite element analysis shows that the modes can be approximately resolved into TE and TM cases where the transverse field is parallel to the flat (lower) oxide surface. TM waves extend further into the air and have slightly lower Q factors. All measurements reported are for TE waves.

The typical coupled power in all measurements was maintained around 1 microwatt to minimize thermal effects. However, there was little or no evidence of thermal effects in the optical spectrum (up to coupled power levels as high as 1 mW). Typically, these appear as an asymmetry in the lineshape and also a scan-direction dependent (to higher or lower frequency) spectral linewidth. As a further check that thermal effects were negligible, ring-down measurements [13] were also performed on a range of devices for comparison to the spectral-based Q measurement. For these, the laser was tuned into resonance with the cavity and a lithium niobate modulator was used to abruptly switch off the input. The output cavity decay rate was then monitored to ascertain the cavity lifetime. Ring-down data and spectral linewidths were consistently in good agreement. This insensitivity to thermal effects is a result of the larger mode volumes of these devices in comparison to earlier work on microtoroids (for which thermal effects must be carefully monitored). The mode volumes in the present devices are typically 100–1000 times larger.

Measurements showing the effects of oxide thickness and device diameter on Q factor

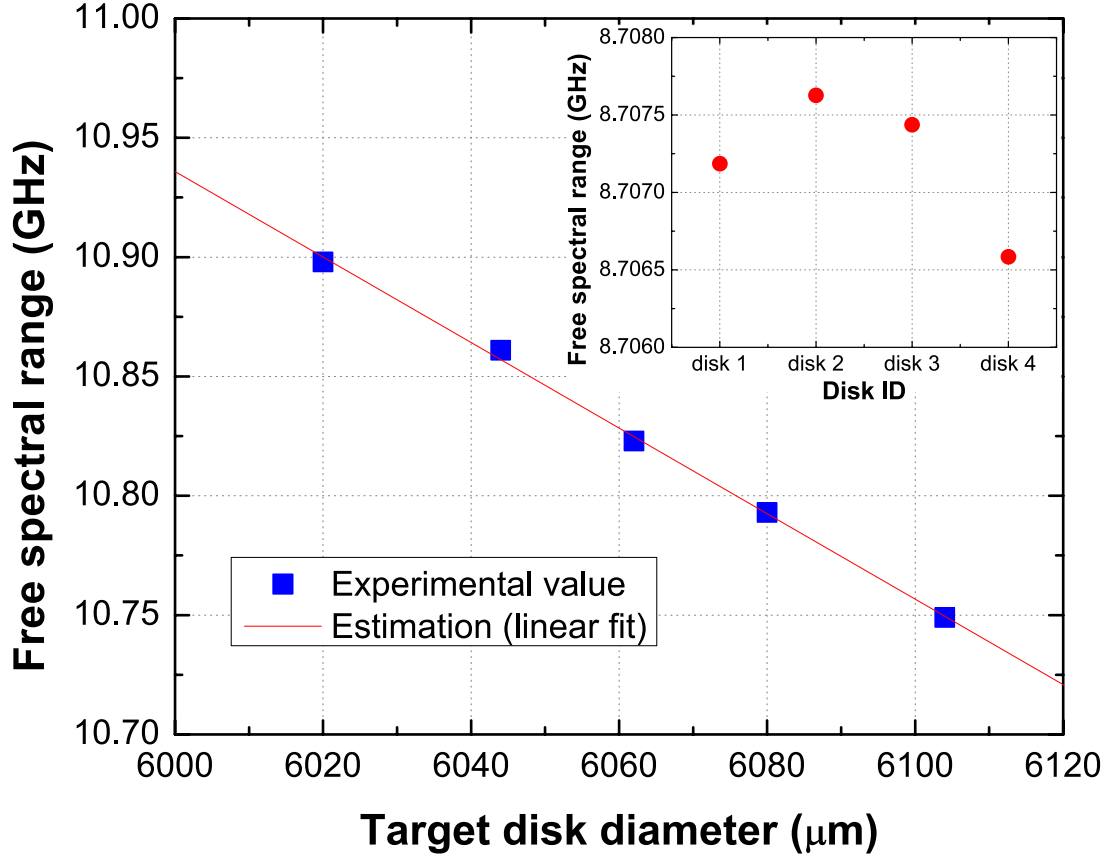


Figure 4.7: Plot of measured free spectral range (FSR) versus the target design-value resonator diameter on a lithographic mask. The plot shows one device at each size and five different sizes. The r.m.s. variance is 2.4 MHz (relative variance of less than 1:4,500). The inset shows the FSR data measured on four devices having the same target FSR. An improved variance of 0.45 MHz is obtained (a relative variance of 1:20,000).

are presented in the Fig. 4.5 main panel. Four oxide thicknesses are shown (2, 4, 7.5 and 10 microns) over diameters ranging from 0.2 mm to 7.5 mm. All data points, with the exception of the red points, correspond to a wedge angle of approximately 10 degrees. The upper most (highest Q at a given diameter) data correspond to a wedge angle of 27 degrees. It is interesting to note that there was a high level of consistency in the Q value measured on devices from a single chip. A complete data set for the red curve in Fig. 4.5 is provided in the Fig. 4.5 caption to indicate the low dispersion in Q data. To estimate these losses, we adapted a general approach reported elsewhere [29, 30, 32]. The solid curves give optical loss caused by surface scattering on the upper, wedge, and lower oxide-air interfaces and by bulk-oxide loss. Herein, the surface roughness was measured independently on each of these

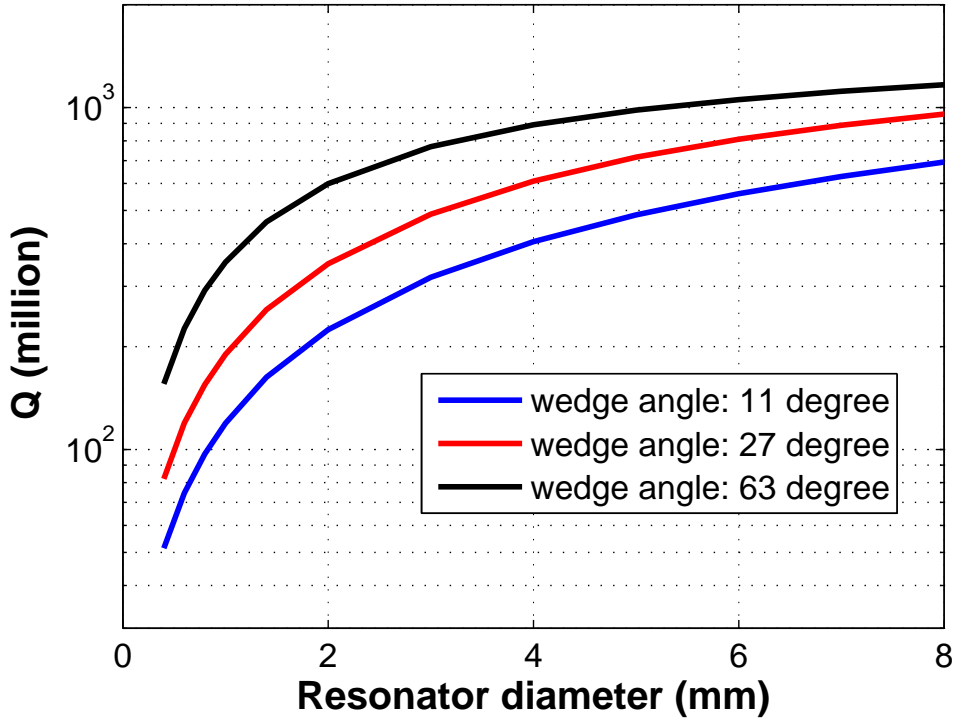


Figure 4.8: Optical Q versus diameter for three distinct wedge angles showing the systematic improvement of Q value with increasing wedge angle

surfaces using an atomic force microscope (AFM). The data corresponding to the 10 degree wedge angle show that Q increases for thicker oxides and also larger diameters. In general, there is reasonably good agreement between the model and the data, except in the case of the thinner oxides. For these thinner structures, there is a tendency for stress-induced buckling to occur at larger radii. This is believed to create the discrepancy with the model.

Using the model, this trend can be understood to result from loss that is caused primarily by scattering at the oxide-air interfaces. Specifically, both thicker oxides and larger-diameter structures feature a reduced field amplitude at the dielectric-air interface, leading to reduced scattered power. An overall boost to the Q factor is possible by increasing the wedge angle. In this case, the mode experiences reduced upper and lower surface scattering as compared to the smaller angle case. As noted before, this behavior is in contrast to the earlier work in which the wedge was used to isolate the mode from edge roughness [9]. Specifically, the larger angle case in Fig. 4.2(b) leads to higher Q values and a record Q factor of 875 million for any chip-based resonators is obtained under these conditions. In particular, because the edge roughness has been eliminated the wedge structure no longer

plays the role of isolating the optical mode. This behavior is further confirmed in the model of Fig. 4.8. Here, the optical Q factor is calculated versus resonator diameter with a fixed oxide thickness of 10 microns and for three different angles. As can be seen in the data, the Q factor steadily improves as the wedge angle is increased.

### 4.3.2 Precise size control of the resonators

The ability to lithographically define ultrahigh-Q resonators as opposed to relying upon the reflow process enables a multi-order-of-magnitude improvement in control of resonator diameter and FSR. This feature is especially important in microcombs and also certain nonlinear sources [57, 58]. As a preliminary test of the practical limits of FSR control, two studies were conducted. In the first, a series of resonator diameters were set in a CAD file used to create a photo mask. A plot of the measured FSR (fundamental mode) versus CAD file target diameter is provided in Fig. 4.7 (main panel). The variance from ideal linear behavior measured on 5 devices from different locations on the same four inch wafer is 2.4 MHz, giving a relative variance of better than 1:4,500 (FSR  $\approx$  11 GHz). The inset to Fig. 4.7 shows that for a second set of four devices from different locations on a separate wafer, but having the same target diameter, the variance is further improved to a value of 0.45 MHz or 1:20,000. More data runs will be accumulated over time to provide better statistics, however, these preliminary findings are nonetheless very encouraging. There is an overall size reduction that occurs between the mask and final etch diameter of about 10 microns (10 micron oxide), however, the above data suggest that this size reduction can be accurately calibrated.

### 4.3.3 Stimulated Brillouin lasers

As an application of the combination of size control and ultrahigh Q available using these new resonators, we then demonstrated stimulated Brillouin lasers (SBLs). Although Brillouin scattering is well known in optical fiber communication, including its use for gain in narrow-linewidth fiber lasers [60], generation of slow light [61, 62] and information storage [63], the realization of microcavity-based SBLs is very challenging on account of the requirement to precisely match the Brillouin shift to a pair of cavity modes. Specifically, the narrow linewidth of the Brillouin gain requires better than 1:1,000 control of the resonator

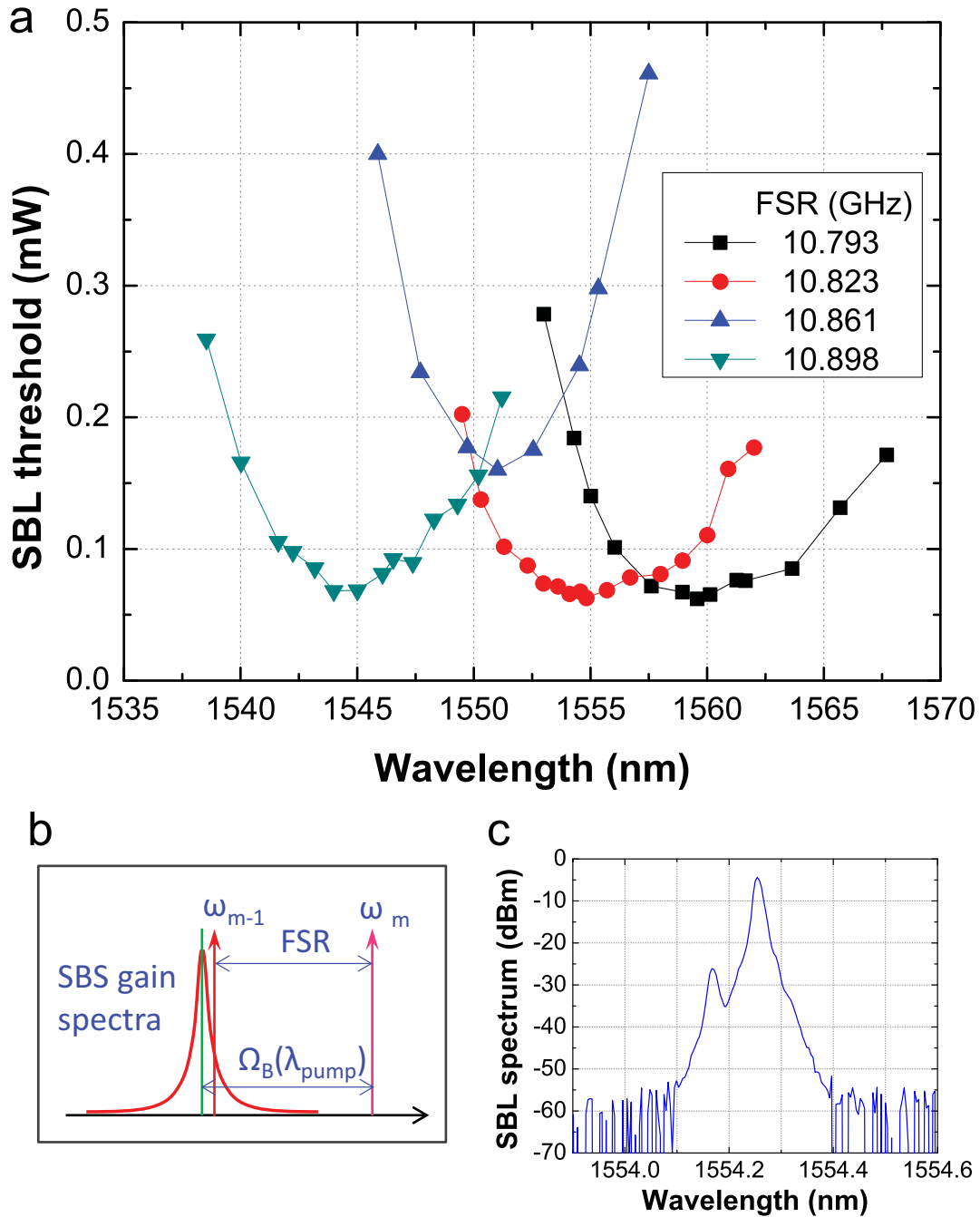


Figure 4.9: Illustration of tuning control of the SBL devices. (a) SBL threshold is measured as a function of pump wavelength using four slightly different resonator diameters. FSRs are indicated in the legend. (b) Illustration of the control of the SBL gain with the change of FSR and pump wavelength. (c) Spectrum of Brillouin laser output showing pump laser (lower peak) and laser output (higher peak). The pump wave appears weaker because the laser emission occurs along the opposite direction to the pump wave.

diameter to obtain a match and more realistically it requires 1:10,000 control for consistent low-threshold turn-on power.

To test the resonators as SBLs, pump power is coupled into the resonator by way of the fiber taper coupler. SBL emission is coupled into the opposing direction and routed via a circulator into a photodiode and optical spectrum analyzer to monitor both the laser output power and the spectrum. The transmitted pump wave is monitored using a balanced homodyne receiver so as to implement a Hänsch-Couillaud locking of the pump to the resonator [64, 65]. The threshold for SBL action is given by the following expression.

$$P_{th} = \frac{\pi^2 n^2 V_{eff}}{g_b Q_p Q_b \lambda_p \lambda_b} \quad (4.1)$$

where  $n$  is the refractive index,  $V_{eff}$  is the mode volume,  $\lambda_p$  ( $\lambda_b$ ) is the pump (lasing) wavelength, and  $Q_p$  ( $Q_b$ ) is the loaded Q factor of the pump (lasing) mode. Beyond the importance of high cavity Q factor evident in this expression, it is essential to maintain a large SBL gain parameter,  $g_b(\Delta\omega - \Omega_B)$  (where gain =  $g_b P_{pump}$ ,  $\Delta\omega$  is the free spectral range, and  $\Omega_B$  is the Brillouin shift). Because the gain spectrum is relatively narrow (typical full-width-half-maximum is 20–60 MHz [60, 66]), this requires a precise match of the free spectral range to the Brillouin shift.  $\Omega_B$  depends on the pump wavelength  $\lambda_p$  and phonon velocity  $V_a$  through the relation  $\Omega_B/2\pi = 2nV_a\lambda_p$ . An illustration of the control possible using the new resonator geometry is provided in Fig. 4.9(a), in which four devices having diameters of 6020, 6044, 6062 and 6080 microns (lithography mask size) were tested at a series of pump wavelengths in the 1500 nm band. In each device, the pump wavelength was sequentially tuned along resonances belonging to the same azimuthal mode family. The minimum threshold for each device corresponds to excitation at the Brillouin gain maximum (*i.e.*,  $g_b(\Delta\omega - \Omega_B = 0)$ ). The rise in threshold away from the minimum (for a given resonator diameter) reflects tuning of the Brillouin shift frequency with pump wavelength noted above. A typical spectrum showing the emitted laser line and the pump are given in Fig. 4.9(c). As an indication of the consistency of size and Q possible, all devices tested lased with minimum threshold values below 200 microwatts. Moreover, on account of the narrow Brillouin gain bandwidth, the side mode suppression at 1 mW output power was in excess of 60 dB (measured by mixing the pump and laser waves on a photo-detector and monitoring the electrical power in the beat note). The coherence properties of these

Brillouin lasers is excellent and is studied in the supplemental material. They, for example, feature sub-Hertz Schalow-Townes linewidths.

## 4.4 Discussion

The Q factor for these new resonators is not only higher in an absolute sense than what has been possible with microtoroids, but it also accesses an important regime of resonator FSR that has not been possible using microtoroids. To date, the smallest FSR achieved with the toroid reflow process has been 86 GHz ( $D = 750 \mu\text{m}$ ) and the corresponding Q factor was 20 million [67]. The present structures attain their best Q factors for FSRs that are complementary to microtoroids (FSRs less than 100 GHz). Beyond the application to stimulated Brillouin lasers described, this range has become increasingly important in applications like microcombs where self-referencing is important. Specifically, low turn-on power and microwave-rate repetition are conflicting requirements in these devices on account of the inverse dependence of threshold power on FSR. However such increases can be compensated using ultrahigh Q because turn-on power depends inverse quadratically on Q [68].

The wedge angle can be shown to provide control over the zero dispersion point in spectral regions where silica exhibits anomalous dispersion. Specifically, beyond 1.3 microns silica features anomalous dispersion, however, the wedge structure introduces a geometrical component of dispersion that is normal (see Fig. 4.2(c)). Calculations show that the overall zero dispersion falls within the 1.5 micron band for the structures tested here. Ultrahigh-Q performance in large area resonators is also important in rotation sensing [15] and for on-chip frequency references [69, 70]. In the former case, the larger resonator area enhances the Sagnac effect. In the latter, the larger mode volume lowers the impact of thermal fluctuations on the frequency noise of the resonator [71]. There can also be potential applications of these structures to cavity optomechanics [72, 73] where the ability to define the whispering gallery and a mechanical support in one lithographic step could provide an improved method to both boost optical Q while controlling mechanical eigenmodes and their damping. For example, spoke structures have been implemented in toroids to minimize clamping losses [74]. By applying the methods described here, structures like these could

be implemented in the same step used to define the whispering gallery.

Although not demonstrated here, there are several ways to incorporate waveguides into these devices. For example, wafer bonding has recently been used to apply a thermal oxide structure to a second wafer containing a nitride resonator with Q factors in the range of 20 million [75]. An adaptation of this approach is being studied to create a nitride-waveguide-coupled UHQ resonator. Such a device does not currently exist and would have a major impact on the many applications of UHQ devices. A key enabler of this approach would be the precise resonator size control that makes possible lithographic-defined fiducial locators to register mating parts. Finally, it is important to note that an upper bound to the material loss of thermal silica was established in this work. The value of 2.5 billion for material Q bodes well for further application of thermal silica to photonic devices. Also, while the ability to leverage thermal silica on silicon in this way is important, the techniques reported here could equally well be applied to high-quality silica deposited onto other substrates.

## Chapter 5

# Ultralow-Loss Silica Spiral Waveguide

### 5.1 Introduction

Fiber-optic waveguide for true time delay is used in rotation sensing, radio frequency photonics, high-stability microwave oscillators, and all-optical signal processing [14–20]. Transfer of these applications to a wafer imposes new challenges on microphotonic fabrication. Waveguide loss must be reduced to unprecedented, low levels and maintained over a broadband. Also, the process must scale so as maintain these low loss levels in a continuous waveguide structure over broad areas. Concerning waveguide loss, the lowest attenuation rates are obtained for a silica-based or silica-clad guide and there has been interest in the practical limits of optical loss in such structures [21–23]. For a pure silica core waveguide [23] the state-of-the-art does not reflect fundamental material limits, but is instead set by interface roughness on the waveguide, itself. Certain processes can heal out this roughness. Laser-induced reflow of thermal silica has been used to create ultrahigh-Q toroidal-shaped resonators [10], but comparably low attenuation rates have not been possible in adapting this technique for waveguide fabrication [76]. Likewise, thermal reflow is possible by introducing dopants such as phosphor and boron so as to lower the melting point of silica below that of silicon. However, the doping process has been observed to increase material optical loss [77].

Characterization of attenuation rate in a very low-loss integrated waveguide is complicated by the insertion loss associated with coupling light into the guide. The most reliable characterization methods avoid this problem entirely by using either resonators or opti-

cal backscatter reflectometry. Resonator Q measurements have long been recognized as a reliable way to characterize spans of waveguide configured into closed-loop whispering galleries [21]; because the Q factor in the under-coupled limit depends only upon waveguide attenuation.

While this method is an accurate way to test loss over a small area, the ultimate goal of replacing optical fiber in certain applications requires much greater spans of waveguide than has been typical in photonics. Local testing of either short spans of waveguide or resonators, while important, is not a sufficient test of device uniformity or fabrication scalability. Over large length spans, optical backscatter reflectometry provides attenuation versus propagation distance that captures attenuation variability caused by wafer-scale variation of the fabrication process [1]. Using backscatter reflectometry, an integrated silica waveguide (length 10 m) with loss of 1.7 dB/m and a silicon nitride in silica guide (length 6 m) with loss of 2.9 dB/m have been demonstrated [22, 23]. Moreover, a silicon nitride waveguide configured into resonators has produced even better results around 1.1 dB/m [78]. A loss of 0.3 dB/m has been reported for a silica guide [79]; and recently, loss less than 0.1 dB/m at 1580 nm (rising to 0.8 dB/m at 1540 nm) has been reported for a 1-meter-long silicon nitride waveguide using a backscatter method [2].

Beyond achieving very low optical loss values, long delay lines present a new and non-trivial device challenge with respect to optical micro-fabrication. The combination of the large required field size, susceptibility to single-point failure and low transmission loss make them sensitive to process-induced defects and defect density levels that might otherwise be tolerated in smaller-area, higher-loss devices. The fabrication process demonstrated here uses only conventional techniques. Specifically, only conventional lithography as well as wet and dry etching are performed. This enables visible defects and voids to be maintained at levels no greater than unity over areas of  $50 \text{ cm}^2$ , ensuring no breaks in transmission. This is an advantage over techniques such as wafer bonding [80].

In this chapter, both optical backscatter reflectometry and resonator Q measurements are used to confirm waveguide loss. Average measured waveguide loss of  $(0.08 \pm 0.01) \text{ dB/m}$  in long spirals is inferred from backscatter measurements over a broad band of wavelengths in the telecommunications window. Also, narrow-band backscatter measurements are used to study the wavelength dependence of the loss and a lower limit of  $(0.05 \pm 0.015) \text{ dB/m}$  is measured. Moreover, a lower value of 0.037 dB/m is obtained with resonator-based mea-

surements. As a simple application of these new devices, a data stream is also transmitted through a delay line to illustrate a data buffer function. The waveguide delay lines reported are the longest, ultralow-loss devices demonstrated to date and the ultralow-loss window is shown to be broadband, spanning the telecommunications window. Moreover, by showing that fields containing long sections of waveguide can be stitched to create an even longer continuous waveguide, the approach is shown to be scalable. Structures over areas as large as  $9.5\text{ cm} \times 9.5\text{ cm}$  are demonstrated and delays as long as 250 m are feasible.

## 5.2 Fabrication process and waveguide structure

To fabricate the waveguide delay line, we have adapted a technique for realization of high-Q silica whispering gallery resonators. Therein, disk resonators with Q factors as high as 50 million (0.5 dB/m) have previously been demonstrated using lithography, followed by a buffered HF etch and  $\text{XeF}_2$  dry etch of the silicon [9]. In those devices, a distinctive wedge profile was applied to isolate the optical mode from the rough lithographic edge. By creating a small-angle wedge, the mode was pushed away from the edge, thereby lowering scattering loss and boosting Q factor. After careful study of this process, we have found that proper etch control can eliminate the lithographic roughness altogether. As illustrated in Fig. 5.1, two competing etch fronts regulate whether the roughness is present. By allowing the etch time to run longer, a single etch front results and ultralow-loss structures can be fabricated over a wide range of angles (8–30 degrees). A long waveguide based upon this wedge geometry was prepared in the form of an Archimedean whispering-gallery spiral. A cross section is shown in Fig. 5.1. In the current design, only one edge of the oxide is used for waveguiding. As discussed later, a ridge design can enable use of the inner edge thereby boosting the areal efficiency of the delay structure. Finally, oxide thickness was increased from prior work so as to further reduce surface scattering loss. A thickness of  $8\text{ }\mu\text{m}$  was used in the present devices.

The details of fabrication is outlined as follows. Waveguides and disks were fabricated on (100) prime grade float zone silicon wafers. The oxide was prepared using the following procedure. An overall  $8\text{ }\mu\text{m}$  oxide film was grown by wet oxidation process. Finally, a dry oxidation process was performed for 24 hours. The temperature for all the oxidation

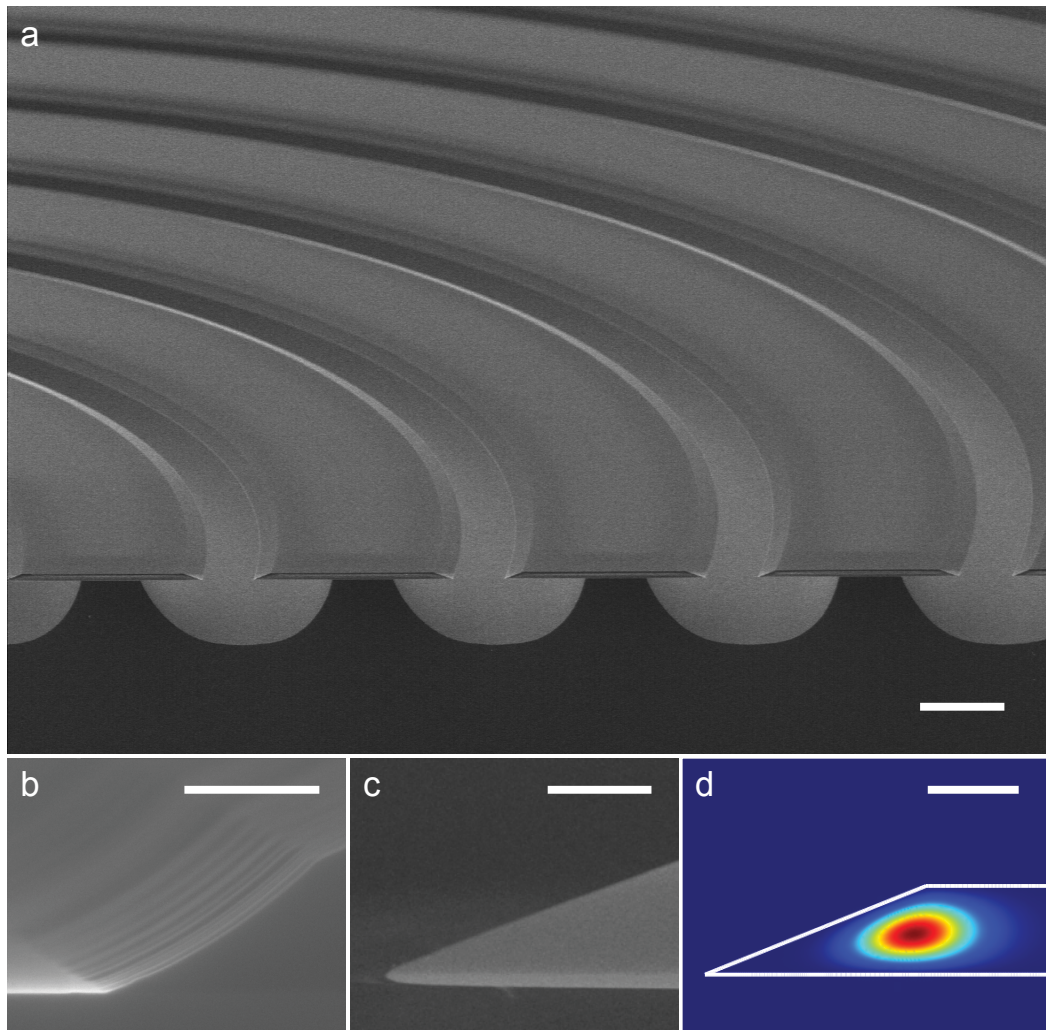


Figure 5.1: An SEM micrograph showing a cross section of the spiral delay line. **(a)** Silicon pillars support thermal oxide structures, the outer edge of which guides the optical mode. **(b)** Close-up view of oxide edge that is formed using a non-optimized etch. Two etch fronts are apparent along with roughening of the oxide surface. **(c)** Close-up view of oxide edge that is formed using an optimized etch. Etch duration has been increased to eliminate one of the etch fronts, resulting in a smooth edge. **(d)** The finite element simulation of the fundamental optical mode propagating inside the waveguide. Scale bars: **(a)**  $100\ \mu\text{m}$ ; **(b)**  $0.5\ \mu\text{m}$ ; **(c)**  $0.5\ \mu\text{m}$ ; **(d)**  $8\ \mu\text{m}$

processes was  $1000^{\circ}C$ . Photo-resist was patterned using a GCA 6300 stepper for disks and Canon FPA 3000iW stepper for spiral waveguides. Post exposure bake followed in order to cure the surface roughness of the photo-resist pattern which acted as an etch mask during immersion in buffered hydrofluoric solution (Transene, buffer-HF improved). The isotropic and uniform etching characteristic of buffered hydrofluoric solution resulted in oxide disks and waveguides having very smooth wedge profile. The reproducibility of the etch is excellent. Specifically, waveguide width control studies for waveguides on the same wafer show a  $\pm 0.25 \mu\text{m}$  variation in width. After the conventional cleaning process to remove photo-resist and organics, the silicon under the oxide structures was isotropically etched by xenon difluoride to create an air-cladding whispering gallery waveguide. Buffer patterns were introduced around the waveguide to prevent non-uniform undercut by loading effect during the xenon difluoride etching.

### 5.3 Backscatter characterization of single-spiral delay lines

An optical backscatter reflectometer (Luna OBR 4400) was used to characterize each delay line. Figure 5.3(a) shows a spiral with a path length of approximately 7 m. (All path lengths quoted here are physical path lengths and optical path lengths are about  $1.45\times$  longer.) The cleaved facet input is at the lower left corner of the chip and features a 7 degree cleave angle so as to reduce Fresnel reflection for backscatter reflectometer measurements. Optical fiber and index-matching oil are used for coupling (See Fig. 5.2). The waveguide is a single, counter-clockwise Archimedean spiral that terminates near the center of the spiral. As noted in Fig. 5.1, waveguiding occurs on the outer edge of the silica. The undercut to the silica must therefore be sufficient to eliminate scattering of the fundamental guided mode with the silicon pillar. Both calculation and measurement (see discussion of Fig. 5.3(c)) show that an undercut of  $60 \mu\text{m}$  is sufficient to lower this silicon pillar interaction to levels below that caused by silica surface scattering. In backscatter measurements, however, the presence of a few higher-order radial modes will produce an enhanced backscatter signal due to their stronger interaction with the silicon pillar. For the same reason, these modes also show higher waveguide attenuation, masking the underlying fundamental-mode optical loss. To prevent this masking effect, the undercut in Fig. 5.3(a) has been increased somewhat

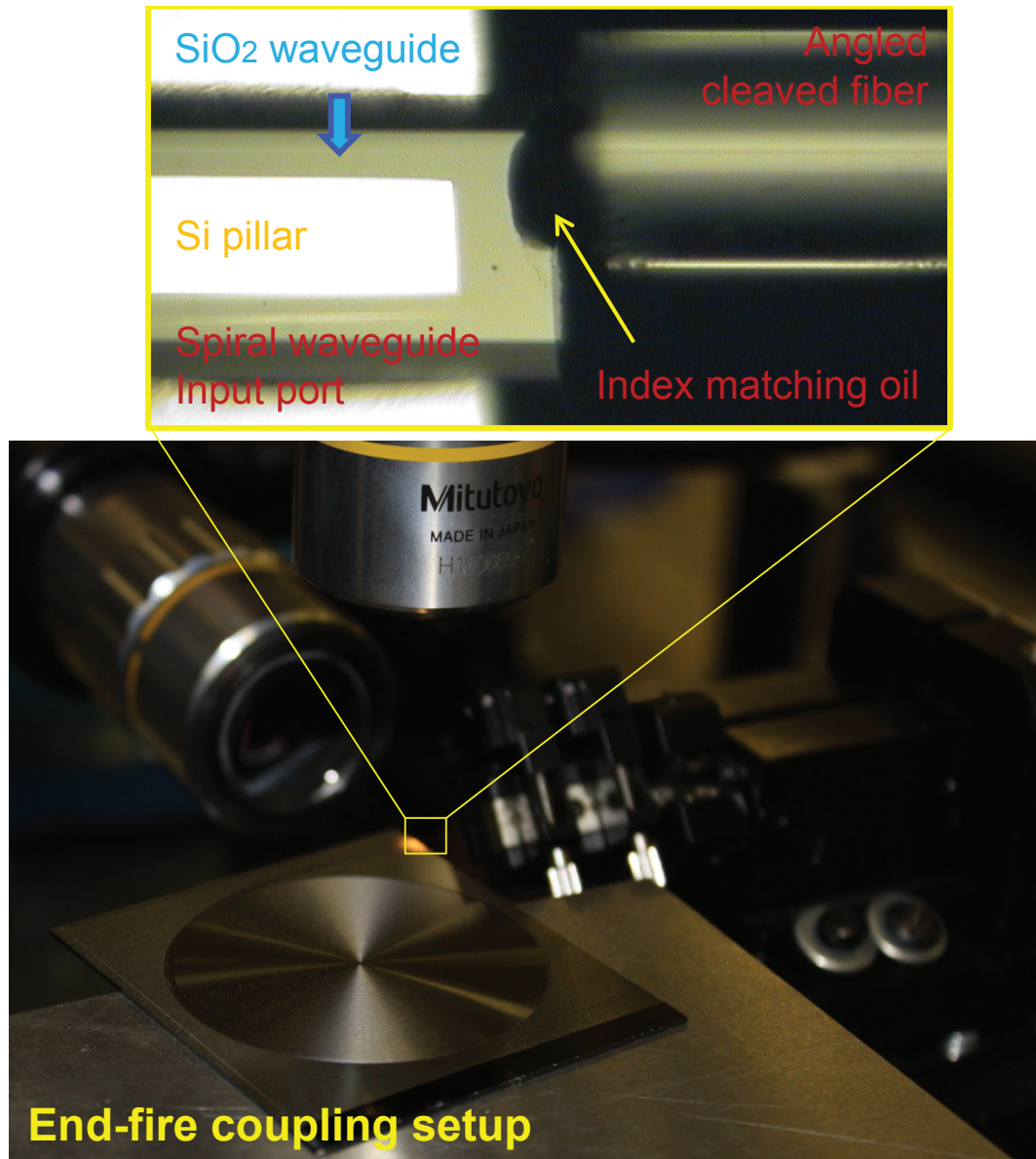


Figure 5.2: Optical backscattering measurement setup. Optical fiber and index-matching oil are used for end-fire coupling.

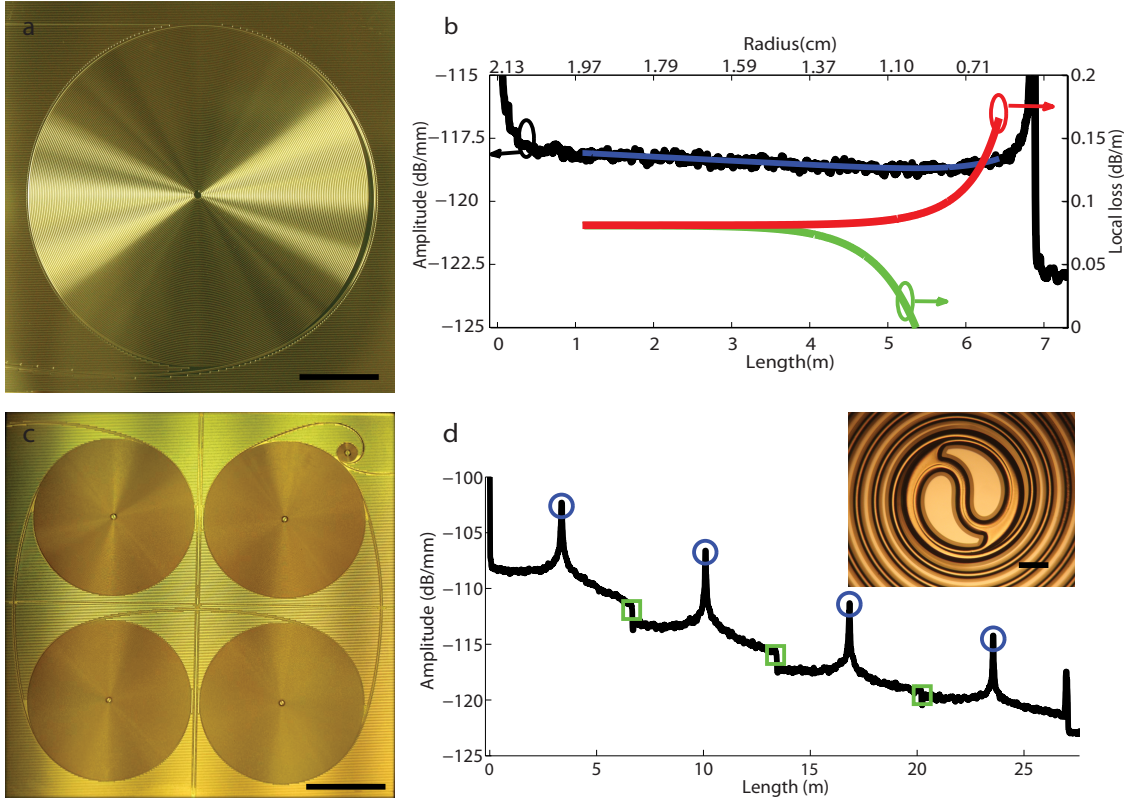


Figure 5.3: Optical micrographs and backscatter reflectometer data for a single spiral and a monolithic spiral cascade. **(a)** An optical micrograph of a 7 m physical path length, counter-clockwise spiral. This spiral has a diameter of 4.3 cm. **(b)** Optical backscatter reflectometer measurement of the spiral waveguide shown in panel **(a)**. On account of the return path, the backscatter decay rate is increased by twofold. The blue curve is a fit to the backscatter level, while the green curve gives a fit to the local backscatter decay rate, and the red curve uses a model to infer the actual local waveguide attenuation, which is approximately 0.08 dB/m over most of the spiral. The upper axis gives the radius from center while the lower axis gives the physical path length. **(c)** Optical micrograph of a cascaded, four-spiral waveguide having a physical path length of 27 m. The input port is in the upper left of the image, and the waveguides connecting neighboring spiral delays are visible. The entire chip is 9.5 cm  $\times$  9.5 cm and consists of four, separately exposed and stitched lithography fields. **(d)** Optical backscatter reflectometer measurement of the spiral waveguide delay line shown in panel **(c)**. The periodic singularities (blue circles) in the backscatter signal correspond to the optical wave transiting the inner adiabatic coupling region of each spiral. Other discontinuities (green squares) in back-scatter occur when the optical wave transfers between the spirals and result from higher-order transverse modes being mode filtered. The inset to panel **(d)** is a magnified view of the adiabatic coupling section, which is approximately 1 mm in diameter. Scale bars: **(a)** 1 cm; **(c)** 2 cm; **(d)** 500  $\mu$ m

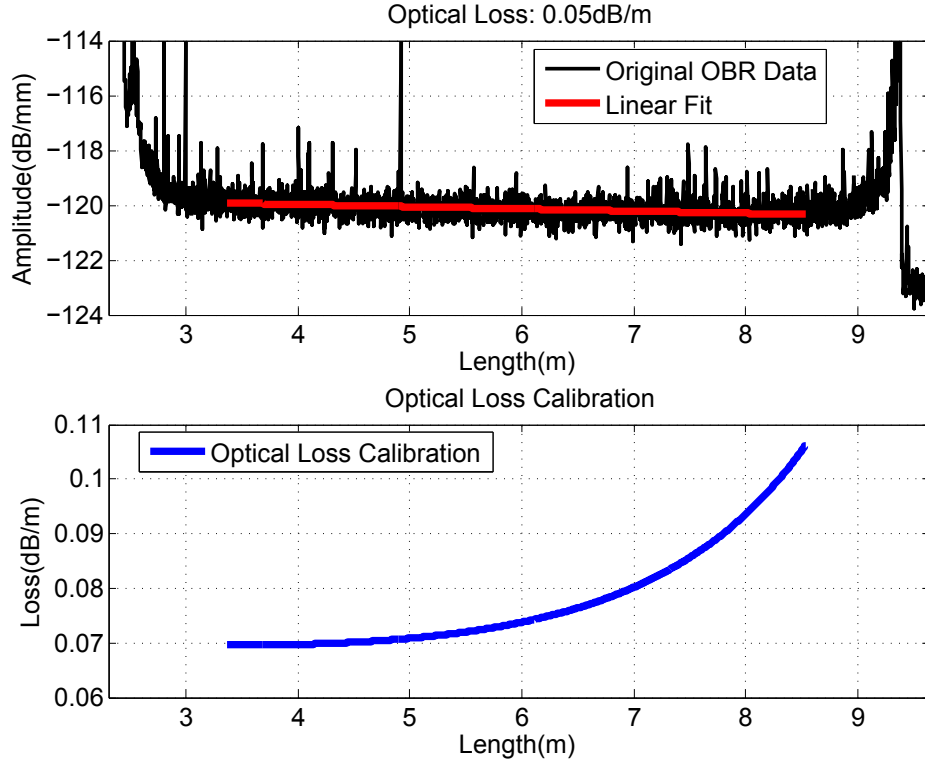


Figure 5.4: The calibration of spiral waveguide attenuation. The naive linear fitting in the upper panel gives an underestimated 0.05 dB/m loss. In contrast, the lower panel shows a more precise local attenuation rate calibrated based on Eq.(5.4).

beyond what is necessary for the fundamental mode. By doing this, even higher-order radial modes excited by the input fiber will experience a negligible level of pillar scattering. This behavior is observed by monitoring backscatter signal in spirals of increasing undercut. The backscatter decay rate is observed to steadily decrease and finally plateau at around  $75 \mu\text{m}$  of undercut.

Backscatter data in Fig. 5.3(b) are obtained for such a deeper undercut spiral. With the exception of the narrow-band spectral study in Fig. 5.9, all back-scatter data are taken using a broadband setting (approximately 90 nm span in the 1550 nm band) [1]. The data show a linear decrease (on the log scale) over nearly the full 7 m of the spiral path. The inferred loss rate from this data is  $(0.05 \pm 0.01) \text{ dB/m}$  and provides a lower bound on the waveguide attenuation rate. This value accounts for the optical return which increases the observed backscatter attenuation rate by twofold. To further refine the estimate, the impact of the varying backscatter signal caused by the changing radius of curvature is accounted for

in the measurement. For this calibration, we first note that bending loss data in Fig. 5.10 when compared to attenuation calculation based upon atomic force microscope (AFM) roughness data show that surface roughness scattering is the principle source of attenuation to diameters at least as large as about 1 cm. Starting with a simple power attenuation equation

$$\frac{dA(z)}{dz} = -\alpha(z)A(z) \quad (5.1)$$

where  $A(z)$  is the optical power at location  $z$  and  $\alpha(z)$  the local waveguide attenuation. By assuming that backscatter strength is proportional to attenuation with coefficient  $C(z)$ , we have

$$\beta(z) = C(z)\alpha(z) \quad (5.2)$$

where  $\beta(z)$  is the local backscattering rate. Since the detected backscattering ( $B(z)$ ) is further attenuated during its back-propagation

$$B(z) = e^{-\int_0^z \alpha(s)ds} \beta(z)A(z) \quad (5.3)$$

By differentiating Eq.(5.3), we finally reached a simple differential equation relates the measured backscatter power,  $B(z)$ , to local waveguide attenuation,  $\alpha(z)$ . The equation is given by,

$$\frac{1}{B(z)} \frac{dB(z)}{dz} = -\left[2\alpha(z) - \frac{1}{\alpha(z)} \frac{d\alpha(z)}{dz}\right] \quad (5.4)$$

This equation shows that when the attenuation rate is changing with distance (in the present case on account of the slowly changing radius of the waveguide), there is a slight correction to the loss as inferred from the backscatter rate. Inward spiraling waves produce a backscatter signal that attenuates more slowly on account of this term, while outward spiraling waves appear to decay more quickly. By using the measured backscatter data as input to the above equation, a corrected value of  $(0.08 \pm 0.01)$  dB/m for the loss of the device in Fig. 5.3(a) is obtained. Figure 5.4 shows the impact of the correction term in Eq.(5.4). The naive linear fitting in the upper panel gives an underestimated 0.05 dB/m loss. In

contrast, more precise local attenuation rate can be calibrated as shown in the lower panel of Fig. 5.4 about 0.07 dB/m loss at the outer of the spiral.

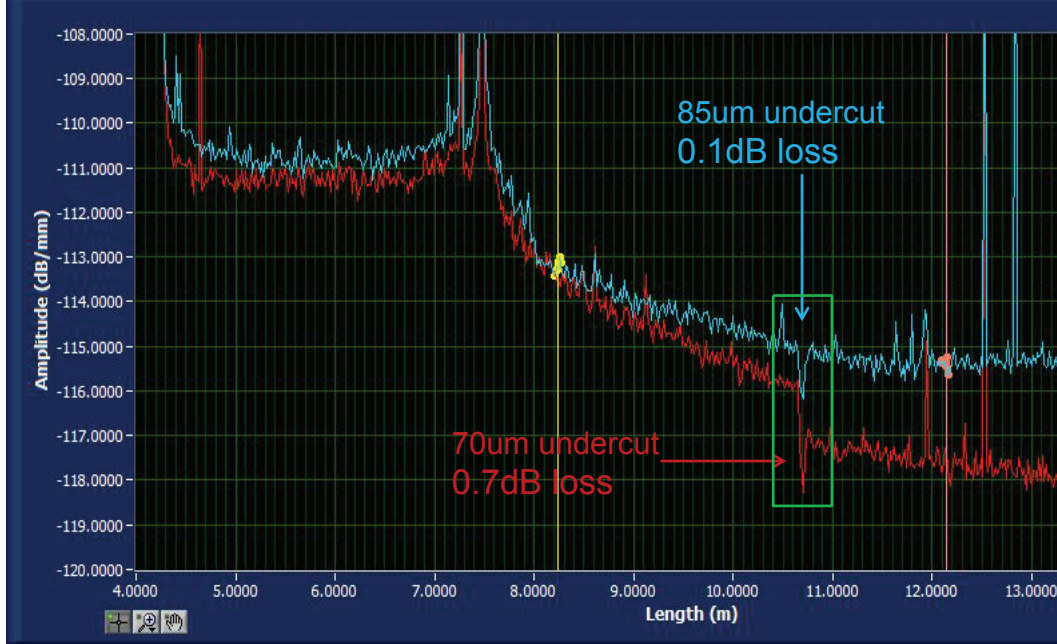
## 5.4 Backscatter characterization of cascaded-spiral delay lines

### 5.4.1 27 meter spiral delay lines

Figure 5.3(c) shows four spirals cascaded on a single wafer to create a 27 m (physical length) waveguide. Each spiral is approximately 4 cm in diameter. The lithography for the spirals involved exposure and stitching of four, distinct lithography fields using a Canon FPA 3000iW stepper tool. The angle-cleaved input facet is in the upper-left corner of this figure. Each spiral features inward and outward, interlaced Archimedean-shaped waveguides that are connected at the spiral center by an adiabatic coupler. The adiabatic coupler features a completely undercut silica guide that is designed so as to maintain propagation in the fundamental transverse mode through the clockwise to counter-clockwise turn. As shown below, the adiabatic coupler introduces about 0.1 dB insertion loss. In the present design, the constraints imposed on this completely-undercut adiabatic coupler when combined with etch nonuniformity over the  $9.5\text{cm} \times 9.5\text{cm}$  wafer area limits the silicon undercut to about  $60\ \mu\text{m}$ . This causes significant interaction of non-fundamental, radial modes with the silicon pillar as noted above. As a result, the backscatter data in Fig. 5.3(d) show an apparent increased loss as light propagates through the first two spirals (also see Tab. 5.1). Moreover, the higher-order modes cause a discontinuity in the backscatter at the large-radii, waveguide interconnection between spirals. These conclusions are confirmed through measurements on smaller-area, cascaded-spiral designs in which a progression of deeper undercuts completely removes the discontinuity and reduces the apparent loss in the entrance spirals. As shown in Fig. 5.5, upon increasing the silicon undercut at the connection between waveguide from  $70\ \mu\text{m}$  to  $85\ \mu\text{m}$  through a local etching, the discontinuity is significantly reduced from 0.7 dB (red curve) to 0.1 dB (blue curve). They are also confirmed by the apparent reduction of attenuation in the third and fourth spirals (see Fig. 5.3(d) and the full characterization results of this spiral waveguide in Tab. 5.1), wherein we believe propagation is primarily in the fundamental mode as a result of high-order mode filtering provided by spirals one and two as well as their interconnections. It is also significant that the backscatter discontinuity between spirals three and four is weak (see and Fig. 5.3(d) and Tab. 5.1), also reflecting

27 m cascade spiral	1st	2nd	3rd	4th
Waveguide loss (dB/m)	$0.23 \pm 0.01$	$0.18 \pm 0.01$	$0.12 \pm 0.01$	$0.11 \pm 0.01$
Hand off loss (dB)	0.03	0.02	0.08	0.04
Connection loss (dB)	0.72	0.76	0.22	

Table 5.1: Loss characterization of 27 m cascade spiral waveguides in Fig. 5.3(c)

Figure 5.5: The connection loss between cascade spirals can be improved via a local etching which increases the silicon undercut at the connection from  $70 \mu\text{m}$  to  $85 \mu\text{m}$ .

propagation primarily in the fundamental mode.

Analysis of waveguide attenuation in any of the spirals of Fig. 5.3(c) is performed by plotting the ratio of out-going to in-going backscatter strength at equidistant points from the spiral center. Such a plot for spiral 3 is shown in Fig. 5.6. The slope of the linear fit gives approximately 0.1 dB/m loss for the waveguide, while the intercept gives an insertion loss for the adiabatic coupler of less than 0.1 dB. A similar value is obtained for spiral 4, while spirals 1 and 2 show an apparent waveguide loss of 0.2 dB/m, presumably because of the presence of higher-order radial modes. The small difference in optical loss (0.08 dB/m vs. 0.1 dB/m) for the spirals of Fig. 5.3(a) and 5.3(c) might reflect slight process variation in the fabrication of these devices.

The adiabatic transition (“hand off”) used to connect the clockwise and counter-

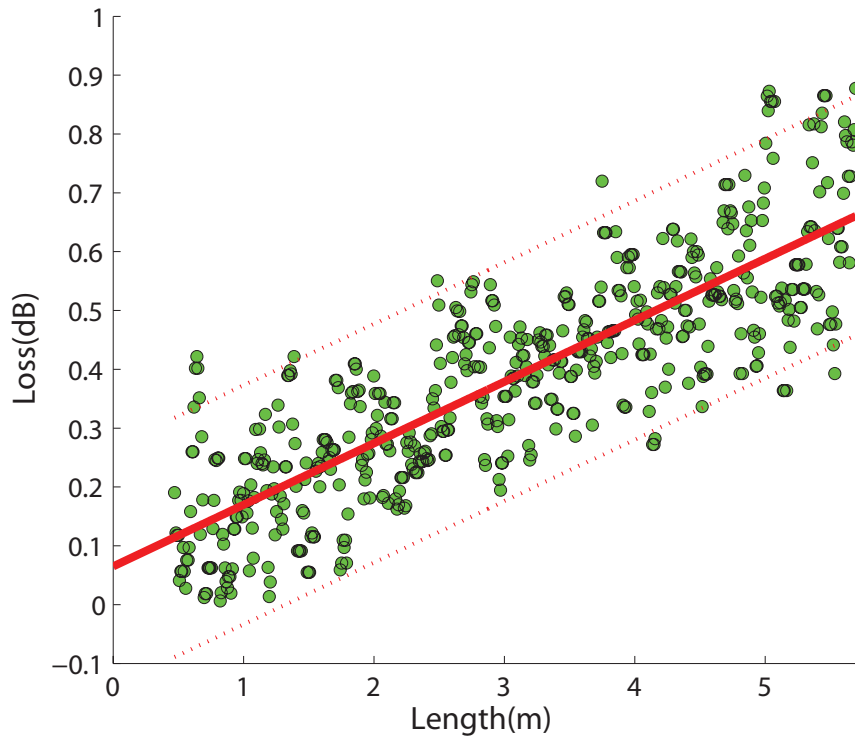


Figure 5.6: Analysis of waveguide loss and adiabatic coupler insertion loss using backscatter data. Green data points are generated by taking the ratio of backscatter signals at symmetrically offset distances away from the adiabatic coupler in spiral 3 of Fig. 5.3(c). The intercept reveals the insertion loss of the coupler as given by a range of possible values falling within a confidence interval. The fitted line (red solid line) slope of about 0.1 dB/m provides a measure of the waveguide attenuation rate and is in reasonable agreement with the spiral in Fig. 5.3(a). The dotted red lines provide the 95% confidence interval.

clockwise Archimedean spirals was designed by applying a variational analysis to the following functional (c.f. **Chapter 6**) [25]

$$E = \int_{z_0}^{z_1} \left( \frac{\partial \kappa(s)}{\partial s} \right)^2 ds \quad (5.5)$$

where  $\kappa(s)$  is the curvature of the waveguide and  $s$  is the arc length. Variation of this equation minimizes the adiabaticity condition over the waveguide. By applying the variation to a third-order polynomial subject to boundary conditions of smooth connection up to the first-order derivative of curvature with the Archimedean spiral, a numerical function for the ‘‘S-shape’’ bend was generated. The S-waveguide width used in the variation was selected so as to allow full undercut of the silica upon etching and reduce intermode coupling [25].

#### 5.4.2 More testing on cascaded-spiral delay lines

The spiral structures offer great flexibilities to design waveguides. Figure 5.7(a-c) shows spirals cascaded on a single wafer to create waveguides with various lengths. The cascade spirals consist of 2, 4 and 6 spirals and have total physical length 6.7 m, 3.6 m, and 1.6 m, respectively. The lithography for these spirals involved single exposure with a MA6 aligner tool. The angle-cleaved facets provide input and output of the waveguides. Optical backscattering measurements were carried to characterize the loss of each structure and the results are summarized in Tab. 5.2. Again, we notice that, in general, the waveguide loss decreases in the later spirals presumably because of high-order mode filtering provided by first few spirals as well as their interconnections. The S-bend hand off might bring 0.1–0.2 dB insertion loss. Also, it is significant that smaller spirals incurs higher losses. It is due to their larger scattering loss at smaller curvature radius. The higher average losses in these samples may also result from the lithography imperfection of aligner compared to stepper.

#### 5.4.3 Loss spectrum

The backscatter reflectometer measurement is based on a frequency sweep method. By degrading spatial resolution, narrower spectral scans are possible so that spectral variation of the waveguide loss can be measured. In Fig. 5.9, spectral data of waveguide loss in a 7 m

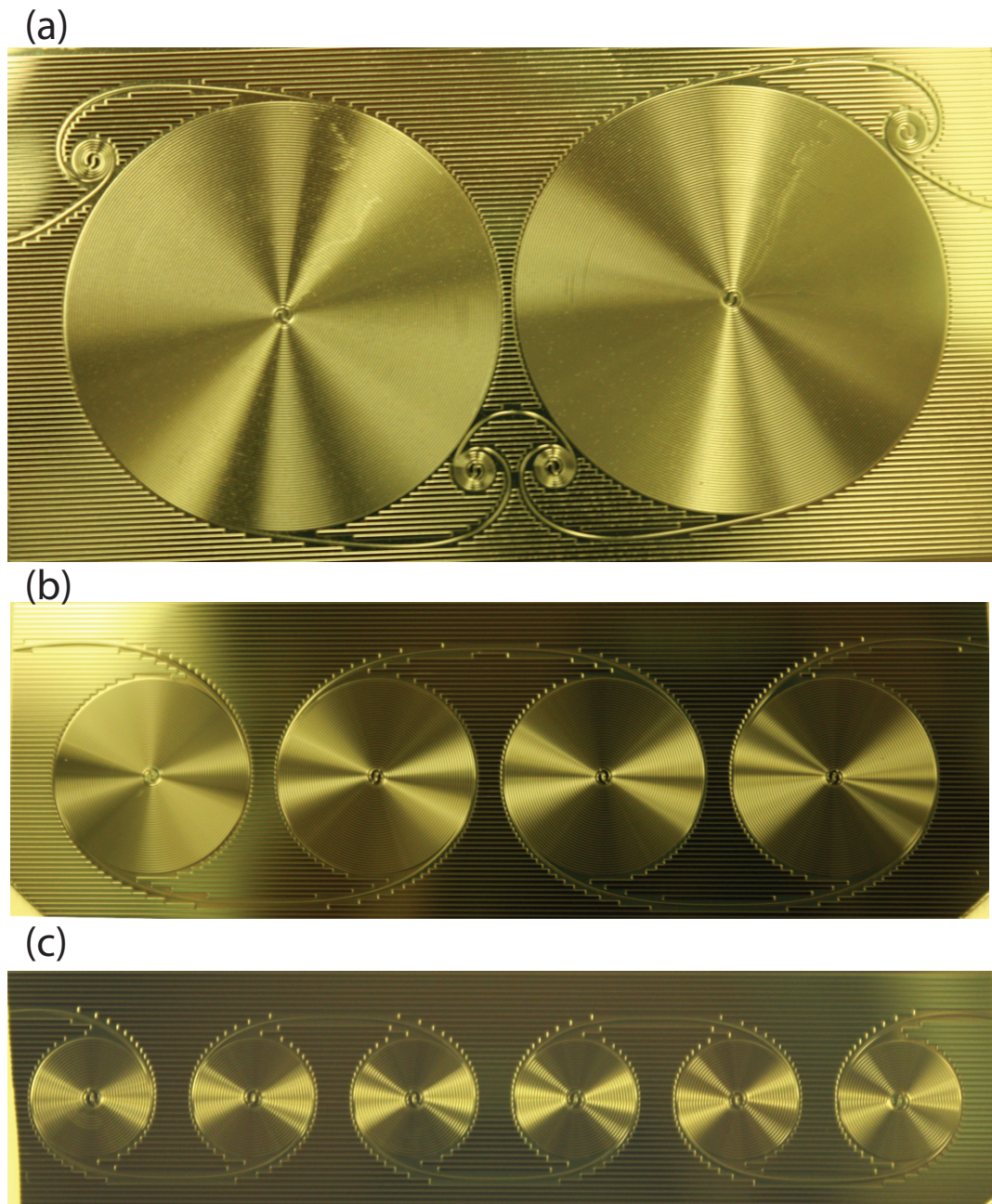


Figure 5.7: The optical images of cascade spirals consist of 2(a), 4(b), and 6(c) individual spirals. The total delay of spirals are 6.7 m, 3.6 m, and 1.6 m, respectively.

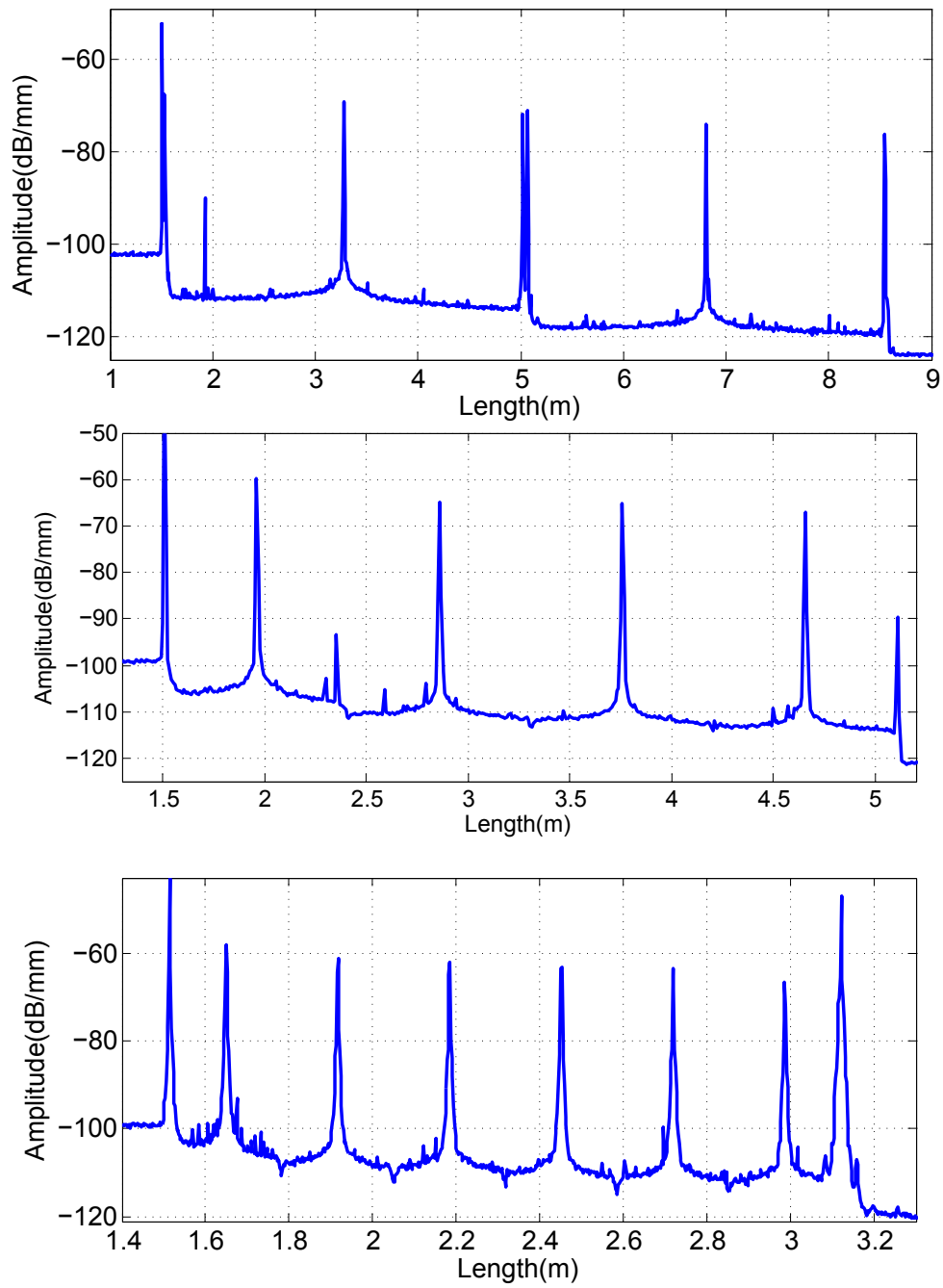


Figure 5.8: Optical backscatter reflectometer measurements of various cascade spiral waveguides shown in Fig. 5.7

2-cascade spiral	1st	2nd				
Waveguide loss ( $dB/m$ )	0.37	0.17				
Hand off loss ( $dB$ )	0.05	0.05				
4-cascade spiral	1st	2nd	3rd	4th		
Waveguide loss ( $dB/m$ )	0.96	0.63	0.69	0.64		
Hand off loss ( $dB$ )	0.09	0.16	0.30	0.11		
6-cascade spiral	1st	2nd	3rd	4th	5th	6th
Waveguide loss ( $dB/m$ )	5.58	2.07	1.33	1.03	0.95	0.98
Hand off loss ( $dB$ )	0.32	0.17	0.14	0.23	0.24	0.11

Table 5.2: Loss characterization of cascade spiral waveguides shown in Fig. 5.7

spiral is presented with the measurement window set to 5 nm (spatial resolution of 200  $\mu\text{m}$ ). A minimum value of  $(0.05 \pm 0.015)$  dB/m is measured near 1595 nm. There is, overall, a weak variation in the apparent loss rate. None of the features seem to be associated with molecular absorption.

## 5.5 Loss analysis

### 5.5.1 Waveguide loss analysis

In the waveguide, transmission loss results from two sources: the absorptive material losses and scattering loss due to the surface roughness. Through Q versus resonator diameter studies, we conclude that scattering losses are the dominant source of loss in the structures tested (see Fig. 5.10). To model these losses, we adapted a general approach reported elsewhere [22, 29, 30]. The rough interface induced radiation loss is calculated via an equivalent volume density, which could be evaluated from the roughness profile and surface electric field

$$\vec{J}(\vec{r}) = -i\omega\epsilon_0(n_0^2 - n_1^2)\vec{E}(\vec{r})\delta(\vec{r} \in \text{interface}) \quad (5.6)$$

where  $\omega$  is the radial frequency of the light,  $\epsilon_0$  is the free-space permittivity,  $n_0$  and  $n_1$  are the refractive index of waveguide and cladding, respectively, and  $\vec{E}(\vec{r})\delta(\vec{r} \in \text{interface})$  gives the electric field at the interface. From this, the far-field radiation as well as the corresponding loss can be evaluated. Assuming that the roughness profiles at top, bottom,

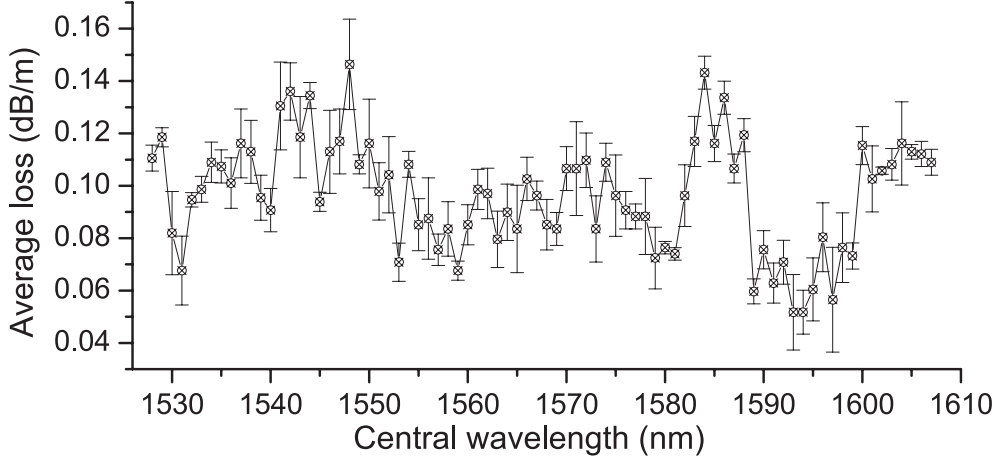


Figure 5.9: The wavelength dependence of waveguide loss. The loss is measured with backscattering reflectometry over a wavelength range of 1528 to 1608 nm in a 7-m-long spiral waveguide. The minimum loss measured is  $(0.05 \pm 0.015)$  dB/m near a wavelength of 1595 nm. The values plotted have been calibrated for spiral curvature using Eq. (5.5). A measurement window of 5 nm is applied [1, 2]. Error bars are included on each point and have been computed by standard deviation of three independent measurements.

and sidewall interfaces are mutually uncorrelated, the scattering loss  $\alpha_{sc}$  is given by [29, 30]

$$\alpha_{sc} = \sum_{interface} \oint (\vec{S}_i \cdot \vec{r}) \tilde{C}(\beta - n_1 k_0) dS \quad (5.7)$$

where  $\vec{S}_i$  is the Poynting vectors generated by the equivalent volume density,  $\beta$  is the propagation constant,  $k_0$  is the wave number and  $\tilde{C}$  is the Fourier transform of the autocorrelation function of the surface roughness profile. Herein, the vectorial electric field at the boundary is calculated using FEM simulation. To determine the surface profile, AFM measurement of the upper, wedge and lower surfaces have also been performed. The roughness profiles are fit to a Gaussian model [29, 30, 32] which gives corresponding r.m.s. roughness variances of 0.15 nm and 0.48 nm with correlation length of approximately 200 nm for the upper and wedge surfaces, respectively. Then, the numerical integration over a spherical surface surrounding the current distribution yields the estimation of the scattering loss.

To obtain the dependence of attenuation on waveguide bending, the Q factor of disk resonators of varying diameters is measured. Data in Fig. 5.10 show that optical attenuation as low as 0.037 dB/m can be obtained in these structures, corresponding to an optical Q factor of 670 million. AFM measurement of the upper, wedge and lower surfaces have

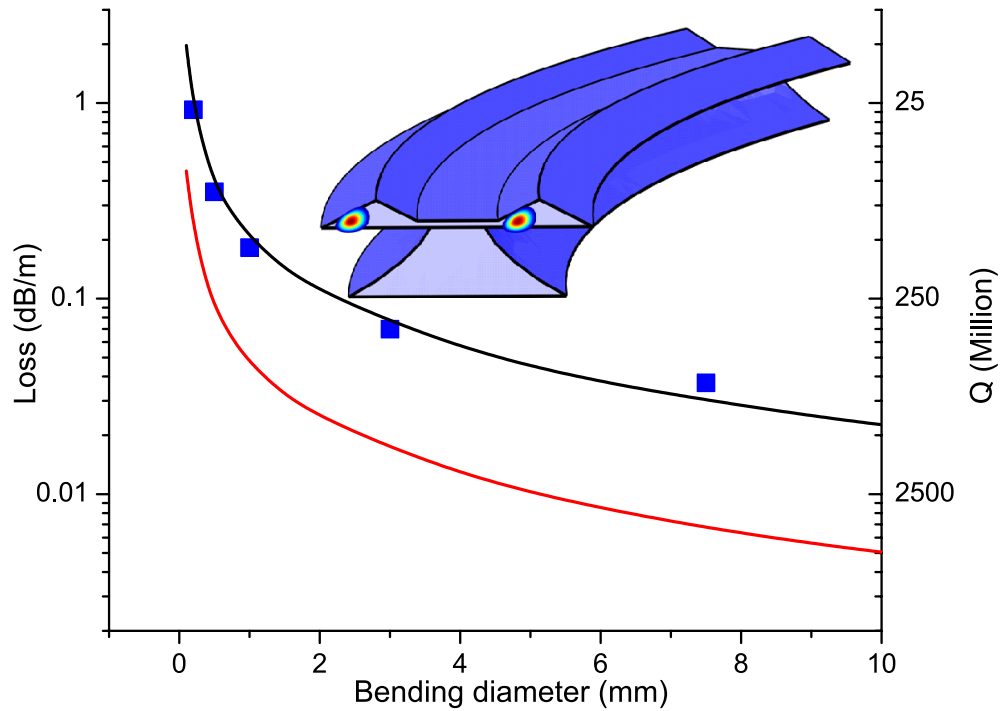


Figure 5.10: Bending loss data plotted versus the bending diameter. The blue squares are data points obtained from  $Q$  measurement on resonators of varying diameters. The black curve is a fit to the data using roughness data provided in the text and obtained using an AFM. The principle source of roughness is the lower interface and an estimate of the bending loss in case this surface can be smoothed to the level of the upper surface is provided as the red curve. The inset shows a modified version of the spiral design in which a waveguide ridge is created so as to provide both interior and exterior guiding in the spiral. The two, color-graded regions give the mode intensity profile.

also been performed on these resonators giving corresponding r.m.s. roughness variances of 0.15 nm and 0.48 nm with correlation length of approximately 200 nm for the upper and wedge surfaces, respectively. The roughness of the lower surface is as large as 1–2 nm in amplitude, but occurs in concentric ring patterns, suggesting that a complex surface interaction takes place during undercut of the silicon. The lower side roughness (assuming a 200 nm correlation length) has been used as a fitting parameter to model the loss versus diameter in Fig. 5.10 (see Methods for discussion of model). Also, a projection of the predicted loss is given assuming that the lower surface roughness could be reduced to that of the upper oxide surface. In the current design, loss levels lower than 0.01 dB/m could be realized. Significantly, the AFM data in conjunction with the optical attenuation data show that thermal oxide is an excellent optical material. Indeed, 0.037 dB/m is a loss value that is close to that of the first technologically successful optical fiber [81]. Concerning the stability of this result, based on early work in silica microspheres [12], it is not expected that water adsorption will impact Q stability for the larger resonator diameters studied here. Indeed, neither resonators or spiral waveguides experienced any measurable degradation over measurement periods that lasted for several days.

### 5.5.2 S-bend (hand off) loss analysis

The insertion loss of S-bend (hand off) (The adiabatic transition used to connect the clockwise and counter-clockwise Archimedean spirals) can be largely explained by surface scattering. As the lightwave propagates through waveguide, it is scattered by bulk material and surface roughness. Only part of the scattering light will be captured and propagate backward to create backscattering signal, whereas others will contribute to scattering loss. Thus, if we assume the capture rate is the same along the waveguide, the scattering loss then is proportional to the backscattering signal. Under this assumption, we can connect scattering loss to the backscattering signal level.

$$\frac{\alpha(z_1)}{\alpha(z_2)} = \frac{B(z_1)}{B(z_2)} \quad (5.8)$$

where  $\alpha(z_1)$  and  $\alpha(z_2)$  are the local attenuation loss coefficients at  $z_1$  and  $z_2$  and  $B(z_1)$  and  $B(z_2)$  are the backscattering levels at  $z_1$  and  $z_2$ . In Fig. 5.11, blue trace shows an

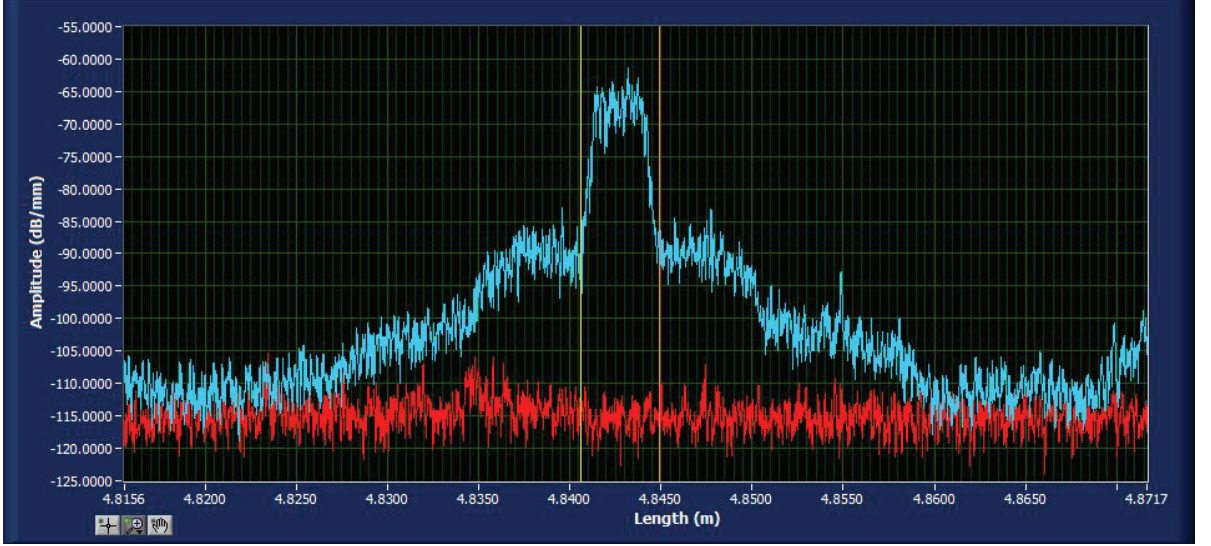


Figure 5.11: Comparison of backscattering trace between S-bend hand off and Archimedean part of spiral waveguide.

optical backscattering from hand off region, and red one gives the trace from Archimedean part spiral waveguide. Apparently, hand off region has much higher level of backscattering which will bring greater scattering loss. To estimate its total insertion loss, we may integrate the backscattering signal across the hand off (from  $z_1$  to  $z_2$ ) and compare it with a similar integration across a span of waveguides (from  $z_3$  to  $z_4$ ) with the same length (approximately 5 mm). We have

$$\alpha_{\text{hand off}} = \alpha_{\text{wg}} l \cdot \frac{\int_{z_3}^{z_4} B(z) dz}{\int_{z_1}^{z_2} B(z) dz} \approx 0.12 \text{ dB}. \quad (5.9)$$

where  $\alpha_{\text{hand off}}$  is the insertion loss of the hand off,  $\alpha_{\text{wg}}$  is the unit attenuation of the waveguide, and  $l$  gives the length of the hand off region. The estimated value of 0.12 dB is consistent with the measurement results using linear regression.

## 5.6 Optical buffer demonstration

As a simple test of the delay line such as might occur in optical buffering, a 13.5 m double spiral was used to delay a 2.5 Gb/s data stream. For this, the light output from an external-cavity semiconductor laser (New Focus, Velocity 6300) was modulated using a lithium niobate modulator (EOspace, intensity modulator AZ-OK5-10) and coupled into

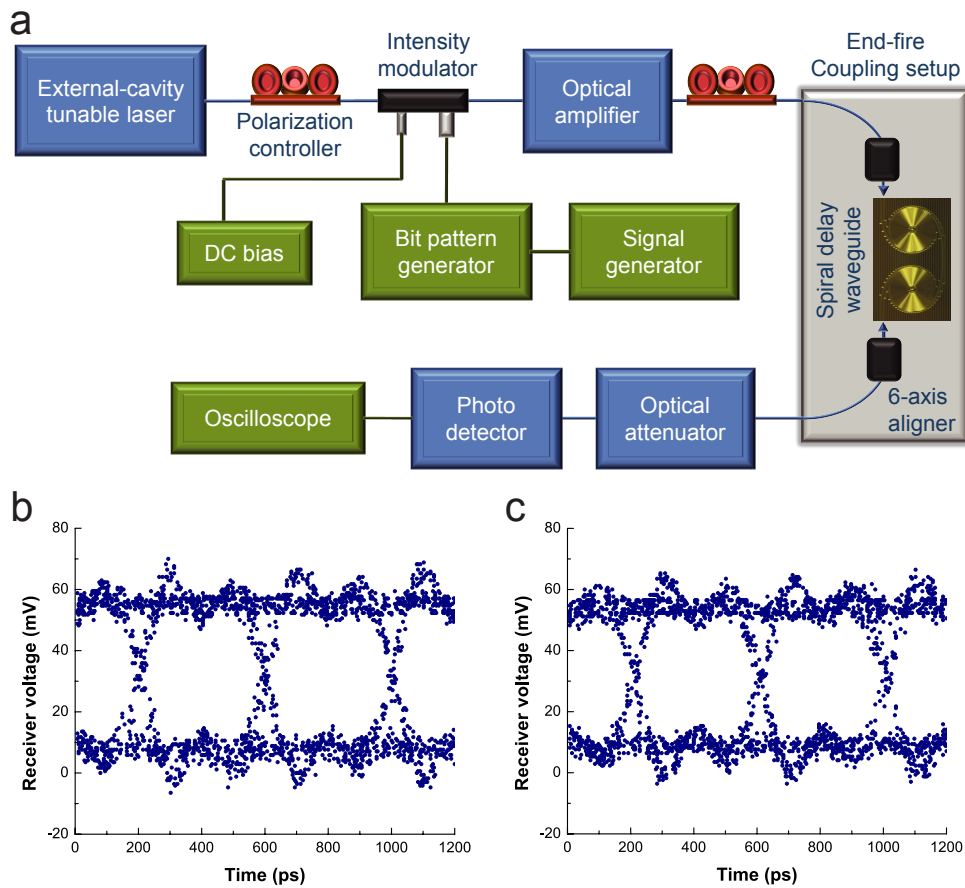


Figure 5.12: Demonstration of the spiral waveguide in the function of data delay as might occur in an optical buffer. (a) Experimental setup used to test a 13.5 m long cascaded spiral in the function of a buffer for a 2.5 Gb/s data stream. Beginning in the upper left of the panel, a single-frequency laser source is modulated to create a pseudorandom bit stream. The bit stream is amplified and coupled into the spiral delay line. Subsequent to the delay, the signal is attenuated, detected, and displayed on an oscilloscope to generate eye patterns. Polarization controllers are also used to launch signals on either the TE or TM mode of the delay line. (b) Eye patterns generated with the 13.5 m spiral delay replaced by a fiber optical cable. (c) Eye patterns generated with the data stream buffered in the 13.5 m spiral delay. The eye patterns of the detected input and output data streams were averaged over 10 s with no visible degradation or change in the structure of the eye pattern.

the delay line. The delay line was mounted onto a six axis aligner and the input and output fibers were coupled using precision 6 axis aligners. The output was passed through a variable attenuator and detected using a high-speed photo-detector (New Focus, model 1554). Eye patterns of the detected input and output streams were averaged over 10 s with no visible degradation or change in the structure of the eye pattern. In this specific test, the optical delay line stored approximately 170 bits. At 10 Gb/s, it would contain 680 bits. Both the setup and the eye-pattern data are presented in Fig. 5.12.

## 5.7 Theory of direct measurements of $n_2$ of the spiral waveguide

Accurate determination of non-linearities of the spiral waveguide is important issue in utilizing in all-optical transport networks. In this section, the second-order refractive index ( $n_2$ ) has been discussed and its measurement techniques are overviewed. The brief description of each measured method is given.

### 5.7.1 Kerr effect nonlinearity

The intensity dependence of the refractive index in the waveguide is called Kerr effect and comes from the third-order susceptibility of the material. In general, the refractive index of the waveguide can be expressed as

$$n = n_0 + n_2 \left( \frac{P}{A_{eff}} \right) \quad (5.10)$$

where  $n_0$  is the intensity independent refractive index and  $n_2$  is the coefficient of the non-linear refractive index, which is related to the third-order susceptibility by the relation.

$$n_2 = \frac{3}{8n} \Re(\chi_{xxxx}^{(3)}) \quad (5.11)$$

Silica has one of the lowest  $n_2$  of any optical material with a typical value of  $n_2$  to be  $2.5 \times 10^{-20} \text{ m}^2/\text{W}$ . Although high intensities are required to make the intensity dependent term significant, appearance of nonlinear phenomena may occur at reasonable powers of few

dBm in the spiral waveguide because of large distances and small effective core area. The intensity dependence of the refractive index leads to a large number of interesting effects including self-phase modulation (SPM), cross phase modulation (XPM), and four-wave mixing (FWM) [82].

### 5.7.2 Measurements via self-phase modulation (SPM)

Self-phase modulation (SPM) refers to the self-induced phase shift experienced by an optical field during its propagation in waveguide. For a light with power  $P$  and wavelength  $\lambda$ , the nonlinear phase shift from a waveguide of length  $L$ , and effect mode area  $A_{eff}$  is

$$\Psi_{NL} = \frac{2\pi}{\lambda} \frac{n_2}{A_{eff}} PL = \gamma PL \quad (5.12)$$

where we have defined a nonlinear parameter  $\gamma$  as [82]

$$\gamma = \frac{2\pi}{\lambda} \frac{n_2}{A_{eff}} \quad (5.13)$$

It quantifies the nonlinear phase shift from a waveguide with unit length and power. When two intense cw-signal with frequency  $\omega_1$  and  $\omega_2$  propagating in an optical waveguide, SPM acts as a beat envelope in the frequency domain. Rather than standard method, we evaluate the effect of self-phase modulation of a mixed light field in the time domain. This method has advantage of reaching an analytical solutions. For two input laser with equal intensity at frequency  $\omega_0$  and  $\omega_1$ , the total input field can be written as

$$\begin{aligned} E(z = 0, t) &= A \left[ e^{i(\omega_0 t + \phi_0)} + e^{i(\omega_1 t + \phi_1)} \right] + c.c. \\ &= A e^{i\omega_0 t} \left[ e^{i\phi_0} + e^{i(\Omega t + \phi_1)} \right] + c.c. \end{aligned} \quad (5.14)$$

where  $A$  is the common amplitude of the field,  $\phi_0$  and  $\phi_1$  are phases and  $\Omega = \omega_1 - \omega_0$ . As the field propagates in the waveguide with nonlinear coefficient  $n_2$ , the phase is modified

via self-phase modulation. At a distance  $z$  in the waveguide, we have [83]

$$\begin{aligned}
\Delta\phi(z, t) &= \frac{2\pi L_{eff}}{\lambda} \cdot n_2 E(z, t)^2 \\
&= \frac{2\pi n_2 L_{eff}}{\lambda} \cdot A^2 \left[ \cos(\omega_0 t + \omega_1 t + \phi_0 + \phi_1) + \cos(\Omega t + \phi_1 - \phi_0) \right]^2 \\
&= \frac{2\pi n_2 L_{eff}}{\lambda} \cdot A^2 \left[ 2 \cos\left(\frac{\omega_0 t + \omega_1 t + \phi_0 + \phi_1}{2}\right) \cos\left(\frac{\Omega t + \phi_1 - \phi_0}{2}\right) \right]^2 \\
&\approx \frac{2\pi n_2 L_{eff}}{\lambda} \cdot 2A^2 \cos\left(\frac{\Omega t + \phi_1 - \phi_0}{2}\right)^2 \\
&= \frac{2\pi n_2 L_{eff}}{\lambda} \cdot A^2 \left[ 1 + \cos(\Omega t + \phi_1 - \phi_0) \right]
\end{aligned} \tag{5.15}$$

where due to the linear absorption of the waveguide, the effective length of it is

$$L_{eff} = L \int_0^L e^{-\alpha l} dl = L \cdot \frac{1 - e^{-\alpha L}}{\alpha} \tag{5.16}$$

Thus, set  $\tau = t - \frac{z}{v}$  where  $v = \frac{c}{n}$  is the phase velocity in the waveguide

$$E(z, t) = A e^{-\alpha z/2} e^{i\omega_0 \tau} \left[ e^{i\phi_0} + e^{i(\Omega \tau + \phi_1)} \right] \cdot e^{-i \frac{2\pi n_2 L_{eff}}{\lambda} \cdot A^2 \left[ 1 + \cos(\Omega t + \phi_1 - \phi_0) \right]} \tag{5.17}$$

Then, taking the Fourier transform, we reach

$$\begin{aligned}
E(z, \omega) &= A e^{-\alpha z/2} e^{-i \left[ \omega_0 \frac{z}{v} + \frac{2\pi n_2 L_{eff}}{\lambda} \cdot A^2 - \phi_0 \right]} \\
&\quad \times \mathcal{F} \left\{ \left[ e^{i\omega_0 t} + e^{i(\omega_1 t + \phi_1 - \phi_0 - \Omega \frac{z}{v})} \right] \cdot e^{-i \frac{2\pi n_2 L_{eff}}{\lambda} \cdot A^2 \cos(\Omega t + \phi_1 - \phi_0)} \right\} \\
&= A e^{-\alpha z/2} e^{-i \left[ \omega_0 \frac{z}{v} + \frac{2\pi n_2 L_{eff}}{\lambda} \cdot A^2 - \phi_0 \right]} \\
&\quad \times \left[ \delta(\omega - \omega_0) + \delta(\omega - \omega_1) e^{i(\phi_1 - \phi_0 - \Omega \frac{z}{v})} \right] \\
&\quad * \mathcal{F} \left\{ e^{-i \frac{2\pi n_2 L_{eff}}{\lambda} \cdot A^2 \cos(\Omega \tau + \phi_1 - \phi_0)} \right\}
\end{aligned} \tag{5.18}$$

where the Fourier transform is defined as  $\mathcal{F}(f(t)) = \frac{1}{\sqrt{2\pi}} \int_{-\infty}^{\infty} f(t) e^{-i\omega t} dt$ . Let  $\psi = \frac{4\pi n_2 L_{eff}}{\lambda} \cdot A^2$  and exploit the Bessel identity ( $e^{iz \cos(\theta)} = \sum_{m=-\infty}^{\infty} i^m J_m(z) e^{im\theta}$ ), we finally reach

$$\begin{aligned}
E(z, \omega) &= A e^{-\alpha z/2} e^{-i \left[ \omega_0 \frac{z}{v} + \frac{\psi}{2} - \phi_0 \right]} \left[ \delta(\omega - \omega_0) + \delta(\omega - \omega_1) e^{i(\phi_1 - \phi_0 - \Omega \frac{z}{v})} \right] \\
&\quad * \mathcal{F} \left\{ \sum_{m=-\infty}^{\infty} (-i)^m J_m\left(\frac{\psi}{2}\right) e^{-im(\Omega \tau + \phi_1 - \phi_0)} \right\}
\end{aligned} \tag{5.19}$$

where we notice that

$$\begin{aligned} & \mathcal{F}\left\{ \sum_{m=-\infty}^{\infty} (-i)^m J_m\left(\frac{\psi}{2}\right) e^{-im(\Omega\tau + \phi_1 - \phi_0)} \right\} \\ &= \sum_{m=-\infty}^{\infty} (-i)^m J_m\left(\frac{\psi}{2}\right) \delta(\omega + m\Omega) e^{im(\Omega\frac{z}{v} - \phi_1 + \phi_0)} \end{aligned} \quad (5.20)$$

which gives

$$\begin{aligned} E(z, \omega) &= A e^{-\alpha z/2} e^{-i\left[\omega_0\frac{z}{v} + \frac{\psi}{2} - \phi_0\right]} \\ &\times \sum_{m=-\infty}^{\infty} (-i)^m J_m\left(\frac{\psi}{2}\right) \int [\delta(\omega' - \omega_0) + \delta(\omega' - \omega_1) e^{i(\phi_1 - \phi_0 - \Omega\frac{z}{v})}] \delta(\omega - \omega' + m\Omega) e^{im(\Omega\frac{z}{v} - \phi_1 + \phi_0)} d\omega' \\ &= A e^{-\alpha z/2} e^{-i\left[\omega_0\frac{z}{v} + \frac{\psi}{2} - \phi_0\right]} \\ &\times \sum_{m=-\infty}^{\infty} (-i)^m J_m\left(\frac{\psi}{2}\right) \left[ \delta(\omega + m\Omega - \omega_0) + \delta(\omega + m\Omega - \omega_1) e^{i(\phi_1 - \phi_0 - \Omega\frac{z}{v})} \right] e^{im(\Omega\frac{z}{v} - \phi_1 + \phi_0)} \end{aligned} \quad (5.21)$$

We notice that the spectrum is discrete, consisting of harmonics of the beat frequency  $\omega_1 - \omega_0$ . The intensity of the wave at frequency  $\omega = \omega_1 + m\Omega$

$$\begin{aligned} I(z, \omega = \omega_1 + m\Omega) &= \frac{nc}{8\pi} E(z, \omega) E(z, \omega)^* |_{\omega = \omega_1 + m\Omega} \\ &= \frac{nc}{8\pi} A^2 e^{-\alpha z} \left[ J_{|m|}^2\left(\frac{\psi}{2}\right) + J_{|m+1|}^2\left(\frac{\psi}{2}\right) \right] \end{aligned} \quad (5.22)$$

where  $m$  is an integer and as defined previously

$$\begin{aligned} \psi &= \frac{4\pi n_2 L_{eff}}{\lambda} \cdot A^2 \\ &= \frac{4\pi n_2 L_{eff}}{\lambda A_{eff}} \cdot P = 2\gamma \cdot L_{eff} \cdot P \end{aligned} \quad (5.23)$$

where  $\gamma$  is the nonlinear coefficient ( $\gamma = \frac{2\pi}{\lambda} \cdot \frac{n_2}{A_{eff}}$ ),  $P$  is the average power and  $A_{eff}$  is the effective area of the optical waveguide and defined as

$$A_{eff} = \frac{(\iint_s |E(x, y)|^2 ds)^2}{\iint_s |E(x, y)|^4 ds} \quad (5.24)$$

where  $E(x, y)$  is the electrical field of the propagation mode. It gives an analytic expression for the frequency components of the field at any waveguide length. The intensity of any

side band is proportional to the input intensity of one of the input intensity,  $\frac{nc}{8\pi}A^2$ . It is possible only to measure the relative heights of the spectral components.

$$\frac{I_0}{I_1} = \frac{J_0^2(\frac{\psi}{2}) + J_1^2(\frac{\psi}{2})}{J_1^2(\frac{\psi}{2}) + J_2^2(\frac{\psi}{2})} \quad (5.25)$$

Here  $I_0$  is the intensity it gives us the ratio of spectral densities of the fundamental wavelength to the first-order sidebands. Now, the phase shift is only a function of  $\frac{I_1}{I_0}$ , which can be easily measured. It is possible to calculate the nonlinear coefficient from the angular coefficient.

$$\frac{n_2}{A_{eff}} = \frac{\lambda}{4\pi L_{eff}} \left( \frac{\psi}{P} \right) \quad (5.26)$$

### 5.7.3 Measurements via four-wave mixing (FWM)

When three lightwave with frequency  $\omega_j$ ,  $\omega_k$ ,  $\omega_l$  interact in a nonlinear medium such as silica spiral waveguide, they give rise to a fourth wavelength ( $\omega_{jkl}$ ) which is formed by the scattering of the incident photons, producing the fourth photon. In general, the optical field amplitude of the FWM component crater in a waveguide of length  $L$  is [82]

$$A_{jkl} = i\gamma \sqrt{P_j(0)P_k(0)P_l(0)} \int_0^L e^{-\alpha z} \exp(i\Delta\beta_{jkl}z) dz \quad (5.27)$$

where  $P_j(0)$ ,  $P_k(0)$  and  $P_l(0)$  are input powers of the three optical carriers and

$$\Delta\beta_{jkl} = \beta_j + \beta_k - \beta_l - \beta_{jkl} \quad (5.28)$$

is the mismatch of propagation constant. We might expanding  $\beta(\omega) = \beta_0 + \beta_1(\omega - \omega_0) + (\beta/2)(\omega - \omega_0)^2$  and using that fact that

$$\omega_{jkl} = \omega_j + \omega_k - \omega_l = \omega_j - \Delta\omega_{kl} \quad (5.29)$$

we have

$$\begin{aligned} \Delta\beta_{jkl} &= -\beta_2(\omega_j - \omega_l)(\omega_k - \omega_l) \\ &= \frac{2\pi cD}{\lambda^2}(\lambda_j - \lambda_l)(\lambda_k - \lambda_l) \end{aligned} \quad (5.30)$$

where the dispersion parameter  $\beta_2$  is converted to  $D$  using  $D = -\frac{2\pi c}{\lambda^2}\beta_2$ . By integration, we finally reach

$$A_{jkl}(L) = i\gamma\sqrt{P_j(0)P_k(0)P_l(0)}\frac{e^{i\Delta\beta_{jkl}L} - 1}{i\Delta\beta_{jkl} - \alpha} \quad (5.31)$$

The power of the FWM component is then

$$P_{jkl}(L) = \eta_{FWM}\gamma^2 L_{eff}^2 P_j(0)P_k(0)P_l(0) \quad (5.32)$$

where the FWM efficiency ( $\eta_{FWM}$ ) is defined as

$$\eta_{FWM} = \frac{\alpha^2}{\alpha^2 + \Delta\beta^2} \left[ 1 + \frac{4e^{-\alpha L} \sin^2(\Delta\beta_{jkl}/2)}{(1 - e^{-\alpha L})^2} \right] \quad (5.33)$$

If we exploit the FWM technique with two optical signals (pump and probe), the intensity of the generated FWM component at the waveguide output is

$$P_{FWM}(L) = \eta_{FWM}\gamma^2 L_{eff}^2 P_{pump}^2(0)P_{prob}(0) \quad (5.34)$$

In the measurement, the ratio between the FWM signal and the probe is proportional to the square of the output pump power

$$R_p = \frac{P_{FWM}(L)}{P_{prob}(L)} = \eta_{FWM}\gamma^2 L_{eff}^2 P_{pump}^2(L)e^{3\alpha L} \quad (5.35)$$

## 5.8 Discussion

There has been no attempt to reduce footprint in this study since the emphasis has been on reduction of attenuation rate and demonstration of scalability. However, a modification of the current design is shown in Fig. 5.10 as an inset. This design uses a ridge geometry produced by a second wet etch to locally confine the mode to both sides of the spiral and leads to a considerable improvement in the area utilization of the wafer. Using the surface roughness measurements described above, we estimate that a comparably low-loss, 100 m long structure could be fabricated in the same footprint as the cascaded spiral of Fig. 5.3(c). Specifically, in the current design approximately 200  $\mu\text{m}$  per waveguide is used in the Archimedean spiral. In the ridge design, this could be reduced to 70  $\mu\text{m}$  per waveguide.

uide. By extension of the stitching method already demonstrated here, it would then be possible to lithographically stitch 10 spiral fields onto an 8 inch wafer for a total path length of 250 m.

Finally, the integration of this optical delay with an optical circuit is also under study. By using a silicon nitride taper design it is possible to adiabatically and selectively couple a single-mode nitride waveguide to the fundamental mode of the spiral structures described here. This is possible because the fundamental transverse mode of the delay line features the largest effective index (since it has the largest propagation constant  $\beta$ ). As such, a silicon nitride (refractive index 2.0) waveguide taper of thickness approximately 200 nm can be tapered so as to reduce its effective index to the point of coupling with only the fundamental transverse mode. Using input and output silicon-nitride adiabatic couplers, the delay line would function essentially as a single transverse mode device, and could be interfaced directly to conventional photonic circuits on silicon.

## Chapter 6

# Low Optical Loss Adiabatic Connections in Waveguides

### 6.1 Introduction

Progress in optical communications has motivated much research in optical circuits composed of basic elements such as modulators, switches and splitters. In designing any type of integrated optical circuit, linking two given points or elements with minimal loss is a universal problem [84]. It is becoming even more important in the light of the recent development of ultralow-loss optical waveguides [3, 21–23, 85]. With propagation loss less than 0.1 dB/m [3, 85], the additional loss imposed by connections in these structures must be addressed carefully. The current design strategy is normally based on piece-wise construction from a certain family of curves, such as ellipses and sinusoidal curves [84, 86, 87]. However, it is not clear that these families will always provide the best possible solution to the general problem of linking two points in an arbitrary optical circuit. Herein, we propose a novel algorithm to the optical connection design. The design algorithm minimizes the transition loss by avoiding excitation of higher-order optical modes. It is physically based and applicable to any waveguide connection (single mode or multimode) between two points in a photonics circuit. The approach is flexible enough to handle arbitrary boundary conditions.

An ideal design algorithm will minimize two types of loss: bending loss and transition loss. The first mechanism is a result of radiative loss present in any bent waveguide. The second mechanism, which is more critical in connection design, comes from the abrupt change or discontinuity of curvature in the connection. It includes not only mismatch of overlap in the propagating mode at the joint points but also the intermode power exchange

(cross talk) caused by the variation of curvature along the connection waveguide path. This cross talk can cause distortion via multimode interference. Because bending loss is most readily reduced by making the bend radius larger or by increasing the mode confinement, it is the connection loss that is the primary focus here. However, the proposed algorithm, by minimizing all intermode coupling, actually minimizes both bending loss and transition loss [88, 89].

A generalized waveguide connection is illustrated in Fig. 6.1 with different curvatures at the terminals of waveguides A and B. In prior work, several different methods have been applied to reduce the insertion loss of this connection. In the offset approach, a small lateral offset in waveguides of different curvature (but having the same tangent) is applied to improve mode overlap [90]. However, this method always results in some mismatch of the modes and also requires high-resolution fabrication. In the matched bent approach, the connection is designed to minimize the leaky-mode excitation at the end of the bend [91]. In particular, if the length of the bent waveguide is a multiple of the beat length of the fundamental and a higher-order mode, then only the fundamental mode is present at the output of the bend. This approach has the side effect of introducing a wavelength dependence into the design. In another method, the curvature is smoothly transformed between the endpoints using specialized curves [92]. One such curve is a clothoid curve [93], which is widely used in highway design [94, 95], robot path planning [96] and computer graphics [97]. However, this method is not general enough to minimize loss in problems containing other constraints such as footprint minimization and general boundary conditions. Our algorithm, in contrast, is based on loss minimization and connection designs satisfying arbitrary boundary conditions. A variational approach is introduced to achieve the optimal curve connecting two waveguide endpoints having specified curvature and tangent vectors. Section 6.2 introduces our general design algorithm, and Section 6.3 describes the experimental result to validate our algorithm.

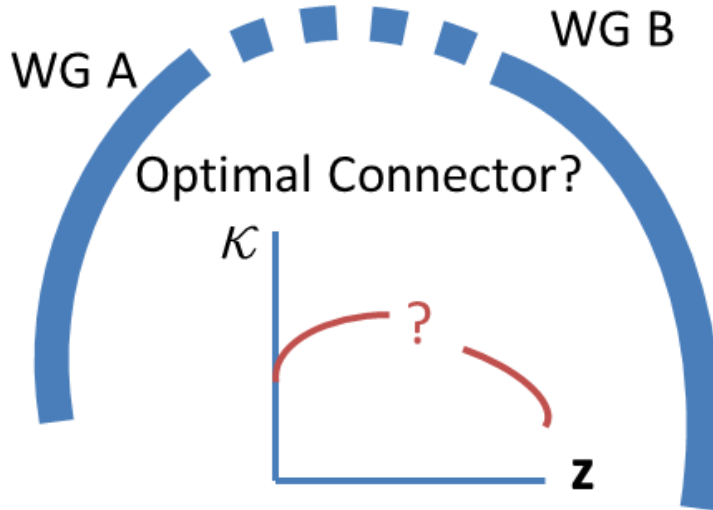


Figure 6.1: An illustration of the generic connection design problem. Waveguides A and B are shown linked by the connection waveguide (dashed). To create a low insertion loss, coupling to higher-order modes must be reduced at the connecting points as well as through out the transition. The inset shows the curvature ( $\kappa$ ) versus path length,  $z$ .

## 6.2 Design algorithm

### 6.2.1 Overview

In a straight waveguide, the fundamental mode is centered in the waveguide, while it is slightly shifted from center in a curved waveguide [98]. This mismatch results in loss when the light transitions between two segments with discontinuous curvature. To this end, we require the junction of the connection region to the waveguides A and B to feature a continuous curvature. Likewise, the curvature is required to be continuous along the connection waveguide. Even with the continuous curvature, the evolution of curvature itself along the connection waveguide can introduce inter-mode power transfer [99, 100]. Accordingly, the slow or adiabatic evolution of curvature along the connector is desirable.

Conformal mapping provides a way to both simplify the discussion and provide a more intuitive understanding of the lightwave evolution [101]. If  $n(x, y)$  denotes the transverse refractive index of the waveguide,  $\kappa(z)$  is the curvature,  $(x, y)$  are the transverse coordinates ( $x = R_1$  and  $x = R_2$  at the inner and outer boundary) and  $z$  is the coordinate along the direction of propagation, then using the conformal transformation (see Fig. 6.2),

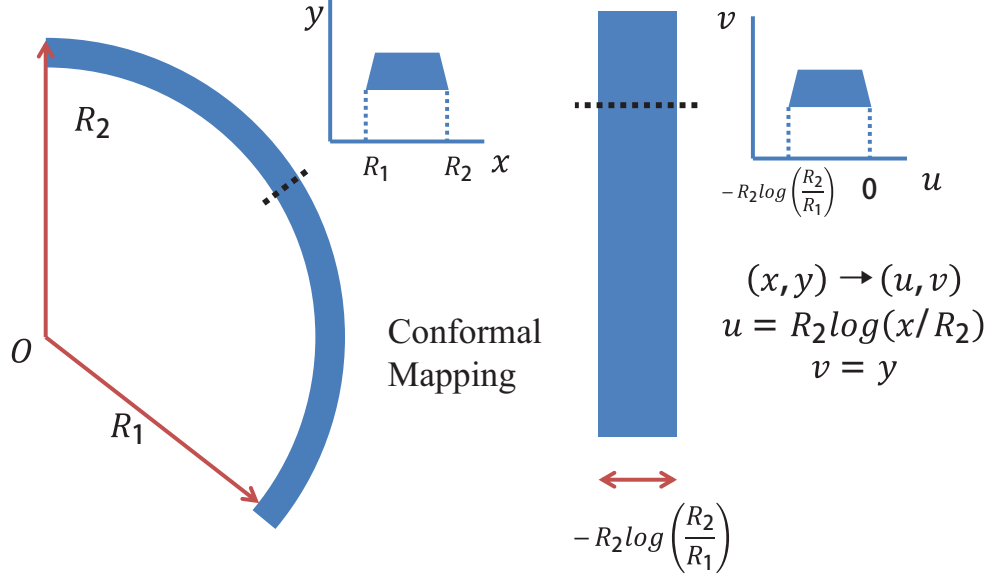


Figure 6.2: Conformal mapping between a bent waveguide and a straight waveguide. The transverse refractive index,  $n(x, y)$ , of the curved waveguide is mapped to  $n_{eq}^2(u, v, z) = n^2(u, v)e^{2u\kappa(z)}$  for a straight guide.

$$(x, y) \rightarrow (u, v) : u = R_2 \log(x/R_2), v = y \quad (6.1)$$

one can show that a bent waveguide with curvature  $\kappa(z)$  behaves like a straight waveguide with a refractive index profile [101] given by,

$$n_{eq}^2(u, v, z) = n^2(u, v)e^{2u\kappa(z)} \quad (6.2)$$

With this mapping, the original problem can be transformed to the equivalent problem of designing the refractive index profile in a non-uniform straight waveguide.

The transition loss can be calculated from coupled-mode theory. We consider a medium with general dielectric constant  $\epsilon(\vec{r})$  and constant permeability  $\mu$ . The fields are expressed by the superposition of local normal modes,  $\{\vec{e}_p(x, y), \vec{h}_p(x, y)\}$ , having propagation constants  $\{\beta_p\}$

$$\vec{E} = \sum_p A(\beta_p, z) \vec{e}_p(x, y) \quad (6.3)$$

$$\vec{H} = \sum_p A(\beta_p, z) \vec{h}_p(x, y) \quad (6.4)$$

with orthonormal condition

$$\iint_S \hat{z} \cdot (\vec{e}_p \times \vec{h}_q^*) dS = \delta_{pq} \quad (6.5)$$

where  $\hat{z}$  is the unit vector along the axis of propagation and “ $S$ ” represents the local surface area that is normal to the axis of propagation. For slow variation in  $\epsilon$ , the coupling coefficient  $C(\beta_p, \beta_q)$  between two modes  $p$  and  $q$  is given by ( $q \neq p$ )

$$\begin{aligned} C(\beta_p, \beta_q) &= \frac{1}{4} \iint_S \hat{z} \cdot \left( \vec{e}_q \times \frac{\partial \vec{h}_p^*}{\partial z} - \vec{e}_p^* \times \frac{\partial \vec{h}_q}{\partial z} \right) dS \\ &= \frac{\omega}{4(\beta_p - \beta_q)} \iint_S (\vec{e}_q \cdot \vec{e}_p^*) \frac{\partial \epsilon}{\partial z} dS \end{aligned} \quad (6.6)$$

where  $\omega$  is the optical frequency in radians/sec. We see that the coupling is directly proportional to  $\frac{\partial \epsilon}{\partial z}$  and only exists between the modes with the same polarizations. Now consider a region from  $z_0$  to  $z_1$  and suppose that at  $z = z_0$  the only non-zero modal amplitude is  $A(\beta_p, z_0)$ . To leading order, the propagation solution is given by:

$$A(\beta_q, z_1) \sim A(\beta_p, z_0) \int_{z_0}^{z_1} C(\beta_p, \beta_q) \exp(i(\beta_p - \beta_q)z) dz \times \exp\left(-i \int_{z_0}^{z_1} \beta_q(z) dz\right) \quad (6.7)$$

Thus, power transfer from mode  $p$  to  $q$  is found to be proportional to  $(\frac{\partial \epsilon}{\partial z})^2 / (\beta_p - \beta_q)^2$ . Namely,

$$\left| \frac{A(\beta_q, z_1)}{A(\beta_p, z_0)} \right|^2 \propto \int_{z_0}^{z_1} \frac{1}{(\beta_p - \beta_q)^2} \left( \iint_S \left( \frac{1}{\epsilon} \frac{\partial \epsilon}{\partial z} \right) dS \right)^2 dz \quad (6.8)$$

Based on the estimation in Eq. (6.8), it is possible to design a curve that will mitigate the power transfer during the variation of curvature. In particular, with the equivalent index profile of curved waveguide  $\epsilon_{eq}(x, y, z) = \epsilon(x, y)e^{2u\kappa(z)}$  and the width of waveguide much smaller than its curvature radius (*i.e.*,  $w = R_2 - R_1 \ll R_1$ ), we have

$$\left| \frac{1}{\epsilon} \frac{\partial \epsilon}{\partial z} \right| \approx \left| 2(R_2 - x) \frac{\partial \kappa(z)}{\partial z} \right| \quad (6.9)$$

Herein, it is apparent that a narrower waveguide is desirable to minimize the power transfer. Assuming the width of the waveguide to be unchanged, a tempting objective functional to

be minimized is given by:

$$E[\kappa(s)] = \int_{z_0}^{z_1} \left( \frac{\partial \kappa(s)}{\partial s} \right)^2 ds \quad (6.10)$$

where, for mathematical simplicity, we have replaced the  $z$  with the arc-length parameter  $s$ . This equation is the working equation used here to minimize the power transfer in a connection waveguide having evolving curvature along the connection path.

### 6.2.2 S-bend design

In this subsection, we apply our algorithm to design a low insertion loss S-bend connection waveguide [3]. S-bend connections waveguides occur in spiral waveguides wherein two interlaced Archimedean spirals (one clockwise and one counter clockwise) must be joined near the center of either spiral. An application of recent interest has been the creation of ultralow optical loss waveguides for true time delay applications [14–18]. Significant efforts have been put into realization of these structures [21–23]. Recently, we have demonstrated a silica-on-silicon waveguide having optical attenuation of 0.08 dB/m over path lengths as long as 27 meters [3]. These delay-line designs feature two embedded Archimedean-shaped spirals, coupled using an S-bend waveguide [3]. In previous research [22, 23], the S-bend waveguide paths are normally constructed from sinusoidal curves, ellipses or other families of curves that are not necessarily the optimal choice. In contrast, using the above described algorithm, we can design an optimal S-bend so as to minimize excitation of higher-order modes.

We note that the functional  $E$  is the  $L^2$  norm of the variation of curvature along the arc. This problem is therefore similar to the “minimization of variation of curvature (MVC)” problem in computer graphics and free-way design [94]. The variation of  $E$  leads to the following corresponding Euler-Lagrange equation,

$$\kappa''(s) = 0 \quad (6.11)$$

The solution family is  $\kappa = k_0 + k_1 s$ , which are similarity transformations of the basic Euler spiral (*i.e.*, clothoid)  $\kappa = s$  [93], where the curvature varies linearly along the length of the

curve. Indeed, the Euler spiral has been employed as the transition curve in connecting straight and bent waveguides [92]. This solution is, however, unsatisfying for a variety of reasons. First, the variational equation is expressed in terms of  $\kappa$  rather than curve  $(x, y)$ ; also, the boundary conditions are expressed in terms of curvature rather than  $z$ . Similarly, positional endpoint constraints are missing. The most general endpoint constraints are the specification of curve length, end point positions, and end point tangents. Of these, the end point position constraints require Lagrange multipliers. The end point constraints  $(x_0, y_0)$  and  $(x_1, y_1)$  for connection to waveguides A and B are expressed as the integral of the unit tangent vector of direction  $\theta(s)$ :

$$\begin{cases} x_0 + \int_0^s \cos(\theta(s))ds = x_1 \\ x_0 + \int_0^s \sin(\theta(s))ds = y_1 \end{cases} \quad (6.12)$$

Therefore, by adding the Lagrange multipliers ( $\lambda_1$  and  $\lambda_2$ ) and eliminating  $\kappa$  in favor of  $\theta$ , the following the functional must be minimized over the length  $l$  [102]

$$E' = \int_0^l [(\theta'')^2 + \lambda_1 \sin \theta + \lambda_2 \cos \theta] ds \quad (6.13)$$

The corresponding Euler-Poisson equation is then given by:

$$2\theta'''' + \lambda_1 \cos \theta - \lambda_2 \sin \theta = 0. \quad (6.14)$$

Without loss of generality we may assume  $\lambda_1 = 0$  and observe that  $\frac{dy}{ds} = \sin \theta$ .

$$\theta'''' - \lambda_2 y' = 0. \quad (6.15)$$

Upon integration, the resulting equation is

$$\kappa'' = \lambda_2 y \quad (6.16)$$

where  $\kappa(s) = \theta'(s)$  and the constant of integration has been set at zero by a translation of the curve. As an aside, it is interesting to note that for  $\lambda_2 = 0$ , this equation is equivalent to that of the Euler spiral. To approximately solve this ODE (Eq. (6.16)), we may consider a family

of curves with curvature given in terms of a cubic polynomial of arc length “ $s$ ” [102, 103].

$$\kappa(s) = a_0 + a_1s + a_2s^2 + a_3s^3. \quad (6.17)$$

This curve family provides a very good approximation to the original variational problem and provides an analytical expression of the connection path [102]. To see this, assuming small turning angles,  $y$  is almost proportional to  $s$  plus a constant offset, so substituting into Eq. (6.16),  $\kappa'' \approx c_1s + c_2$ , and then integrating twice yields Eq. (6.17).

The coefficients of the polynomial ( $a_i$ ) are determined by matching the endpoint po-

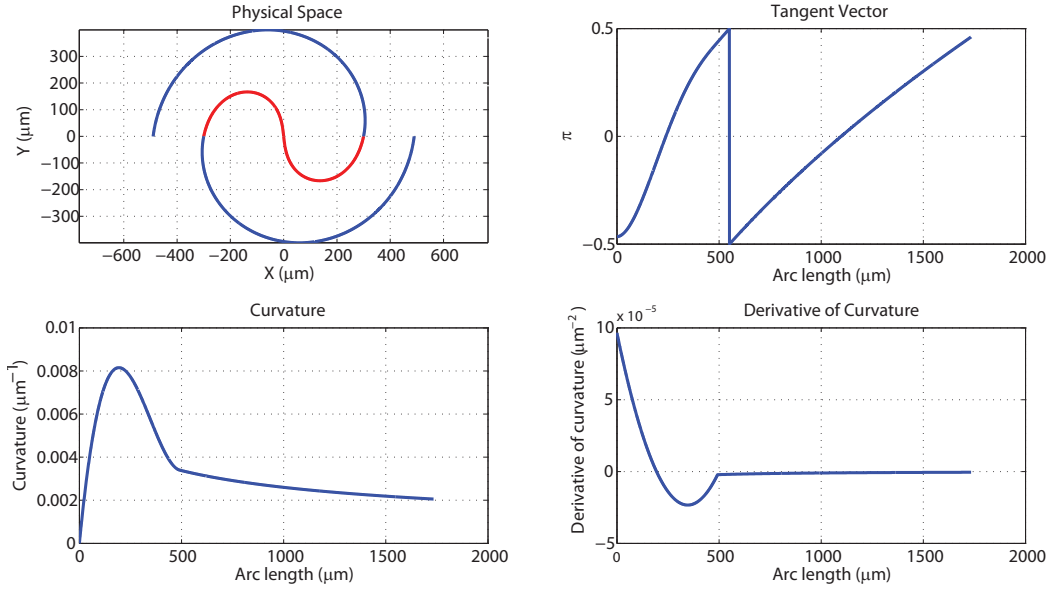


Figure 6.3: The optimal S-bend design that minimizes mode coupling between clockwise and counter-clockwise Archimedean spiral waveguides. A jump from  $0.5\pi$  to  $-0.5\pi$  of the tangent vector in the upper right panel is due to the convention that the tangent vector is defined as  $[-0.5\pi, 0.5\pi]$  (for example, a tangent vector of  $0.6\pi$  is considered as  $0.6\pi - \pi = -0.4\pi$ ). The geometry property is still continuous.

sitions, endpoint tangents and the curvature between the S-bend and Archimedean spiral. By symmetry, we only need to design the incoming arc of the S-bend. This curve starts at the origin ( $x = 0, y = 0$ ) and has curvature  $\kappa = 0$  at  $x = 0, y = 0$ , which leads to the

following formulation

$$\left\{ \begin{array}{l} \theta_1 = \theta_0 + \int_0^{s_1} \kappa(s) ds = \theta_0 + \int_0^{s_1} a_1 s + a_2 s^2 + a_3 s^3 ds \\ \kappa_1 = a_1 s + a_2 s^2 + a_3 s^3 |_{s=s_1} \\ \kappa'_1 = \frac{d\kappa(s)}{ds} |_{s=s_1} = \frac{d}{ds} (a_0 + a_1 s + a_2 s^2 + a_3 s^3) |_{s=s_1} \\ (x_1, iy_1) = \int_0^{s_1} \exp(i\theta(s)) ds \end{array} \right. \quad (6.18)$$

The additional constraint of curvature at the starting point has been enforced and gives  $a_0 = 0$ . By solving a set of unknowns  $(a_1, a_2, a_3, \theta_0, s_1)$  to match the input parameters  $(\theta_1, \kappa_1, \kappa'_1, (x_1, iy_1))$  from the end point of the Archimedean spiral, a curve for the adiabatic coupler is successfully defined as shown in Fig. 6.3. In particular, to specify the constraint, without loss generality, let the position of connection be  $(x, y) = (A, 0)$ , the Archimedean spiral can be specified in the polar coordinate  $(r, \phi)$  as

$$r = R + A\phi \quad (6.19)$$

with curvature given as

$$\kappa(\phi) = \frac{R^2 + 2AR\phi + A^2(2 + \phi^2)}{(R^2 + A(A + 2R\phi + A\phi^2))^{1.5}} \quad (6.20)$$

and its derivative with respect to  $s$  (the arc-length parameter  $s = R\phi + \frac{1}{2}A\phi^2$ )

$$\frac{d\kappa(\phi)}{ds} = \frac{d\kappa}{ds} \frac{ds}{dt} = \frac{-A(A(2A + 2r\phi + A\phi^2) + r^2)}{(A(A + 2r\phi + A\phi^2) + r^2)^{2.5}} \quad (6.21)$$

At the connection point ( $\phi = 0$ ), the boundary conditions are given as

$$\left\{ \begin{array}{l} \tan(\theta) = dy/dx |_{\phi=0} = \frac{R}{A} \\ \kappa(\phi = 0) = \frac{2A^2 + R^2}{(A^2 + R^2)^{1.5}} \\ \frac{d\kappa(\phi=0)}{ds} = \frac{-A(2A^2 + r^2)}{(A^2 + r^2)^{2.5}} \\ (x_1, y_1) = (A, 0) \end{array} \right. \quad (6.22)$$

along with Eq. (6.18), we could solve all the parameters that define the hand-off region curve.

### 6.3 Experimental verification

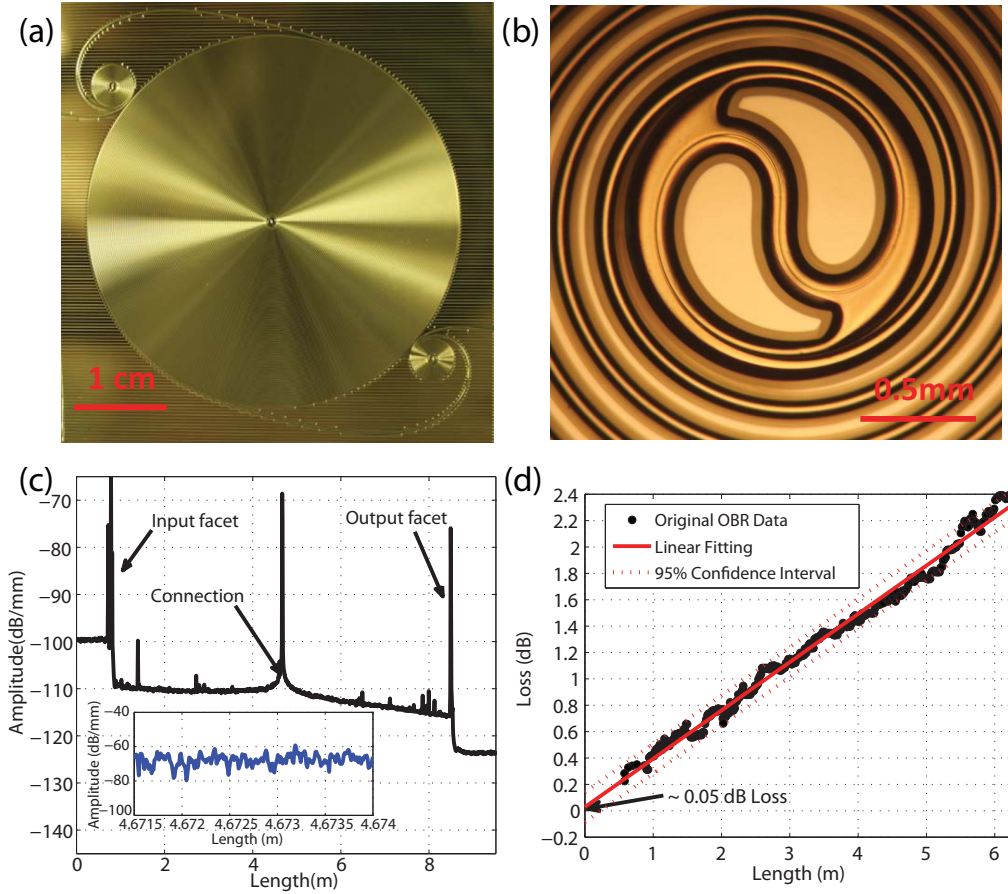


Figure 6.4: (a) Optical micrograph of a spiral waveguide having a physical path length of 7 meters. The input port is in the upper left of the image, and there are two small spirals at the input and output ports (not resolved in the backscatter trace of panel (c)). The entire chip is  $4.5 \text{ cm} \times 4.5 \text{ cm}$ . (b) A magnified view of the adiabatic coupling section (approximately 1 mm in diameter). Light brown regions are silicon (under oxide or exposed) while darker brown regions along the border of the light brown are silica that has been undercut by dry etching. Very dark brown border regions are also silica but have a wedge profile. For further details see Ref. [3]. (c) Optical backscatter reflectometer measurement of the spiral waveguide. Besides occasional random noise spikes that we believe are associated with small dust particles on the surface of the waveguide, the major singularities in the backscatter signal correspond to the input facet, the optical wave transiting the inner adiabatic coupling region of the spiral and the output facet. The inset shows a close-in view of the adiabatic coupler region (*i.e.*, peak of the singularity). There is no apparent drop in signal within this region. (d) Analysis of the adiabatic coupler insertion loss using backscatter data. Data points are generated by taking the ratio of backscatter signals at symmetrically offset distances away from the adiabatic coupler in (a). The intercept reveals the insertion loss of the S connection as given by a range of possible values falling within a confidence interval determined by linear regression.

Measurement of connector loss in waveguides is complicated by the insertion loss associated with coupling light into the waveguide. The most reliable characterization methods avoid this problem entirely by using either optical backscatter reflectometry [1] or resonator Q characterization. To this end, we employed two independent tests to validate our design algorithm. Firstly, a two-way spiral waveguide (Fig. 6.4(a)) was fabricated [3]. It features inward and outward, interlaced Archimedean-shaped waveguides that are connected at the spiral center by our adiabatic connector designed with our algorithm. We expect our coupler to maintain propagation in the fundamental transverse mode through the clockwise to counter-clockwise turn. The performance of the coupler is evaluated by its additional insertion loss. Secondly, Fig. 6.7(a) shows a closed-loop resonator consist of two couplers. By measuring its quality (Q) factor, the insertion loss and the mode preservation of the coupler can be extracted. This approach could not only confirm the minimal power loss from the connector but also verify its mode preservation properties.

### 6.3.1 Spiral waveguide measurements

We firstly use optical backscatter reflectometry [1] to characterize the insertion loss. The spiral waveguides and S-connector waveguide are fabricated via procedures outlined in Ref. [3]. This process begins with lithography and etching with buffered hydrofluoric acid of silica on silicon. The oxide layer then functions as an etch mask for an isotropic dry etch of the silicon using  $\text{XeF}_2$ . Further details on the processing are given in Ref. [3]. Fig. 6.4(a) shows a 7 m (physical length) spiral waveguide that is approximately 4.5 cm in diameter. The angle-cleaved input facet (7 degree cleave angle) is at the upper-left corner of the chip. Optical fiber and index-matching oil are used for end-fire coupling. The waveguides have a width of 170 microns. A magnification of the S-shaped connection is shown in Fig. 6.4(b). The connection width was tapered to 10 microns at its narrowest point to relax the condition in Eq. (6.9). The spiral waveguides were characterized using a Luna OBR 4400 backscatter reflectometer [1]. A measured backscatter trace is given in Fig. 6.4(c). As can be seen in the trace, the adiabatic connector creates a singularity in the backscattering signal. Higher-resolution measurement of this singularity reveals that this region rises and plateaus over a length of several mm at the center of the S-bend connection (see inset to Fig. 6.4(c)). The apparent lack of any decrease in backscatter signal within this region required that another method be applied to analyze the coupler loss.

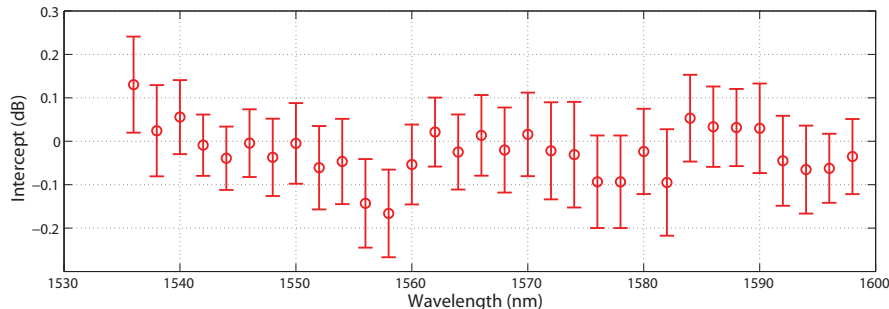


Figure 6.5: The S-connection intercept (see Fig. 6.4(d)) measured with backscattering reflectometry over a wavelength range from 1536 to 1598 nm in a 1-meter-long spiral waveguide. A measurement window of 10 nm is applied. The error bars are obtained from three independent measurements.

As an alternate measurement, we plotted the ratio of out-going to in-going backscatter strength at equidistant points from the spiral center. By symmetry, these pairs of points will have the same curvature. The ratio of backscatter strength can be written as

$$\log\left(\frac{P_{backscatter}(\frac{z}{2})}{P_{backscatter}(-\frac{z}{2})}\right) = -\alpha_1 \cdot z - \alpha_0 \quad (6.23)$$

where the center of the spiral is the origin,  $P_{backscatter}(\frac{z}{2})$  and  $P_{backscatter}(-\frac{z}{2})$  are out-going and in-coming waveguide backscattering strength at the equidistant points from the spiral center; the waveguide length between these two points is  $z$ ;  $\alpha_1$  is the waveguide loss per unit length and  $\alpha_0$  is the insertion loss of the S-bend connection. Such a plot is shown in Fig. 6.4(d). The slope of the linear fit gives approximately 0.35 dB/m loss for the waveguide, while the intercept gives an estimated insertion loss for the adiabatic coupler of 0.05 dB. This insertion loss and the indicated confidence interval result from linear regression on all of the points. Data points within 0.25 meters of the S-bend have been omitted in this estimate as there is a large increase in the variance on account of the steep slope associated with the backscatter singularity (see Fig. 6.4(c)). As an aside, the spiral device of this measurement was fabricated using a contact aligner and therefore features a higher waveguide loss as compared to that reported in Ref. [3], wherein devices were fabricated using a Canon stepper lithography tool.

To evaluate the spectral performance of the connection, backscattering measurements were performed over 1536 – 1598 nm with an instrument measurement window set to 10 nm.

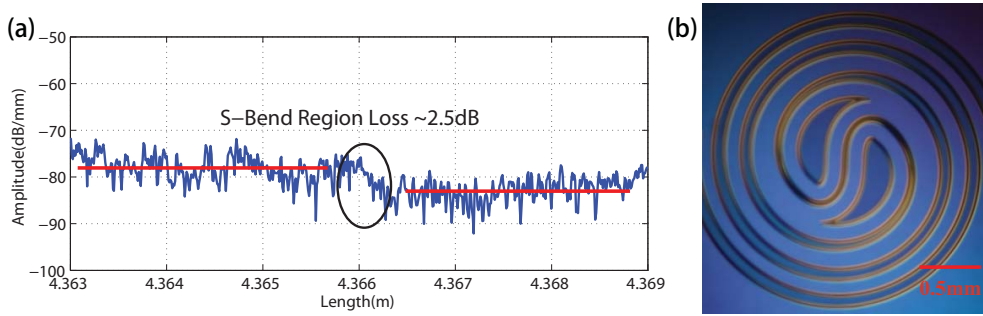


Figure 6.6: **(a)** A high-spatial-resolution, backscatter trace of an unsuccessful S-bend design based on a conventional clothoid curve design. About 2.5 dB insertion loss was measured using the OBR measurement technique. **(b)** Micrograph of the clothoid curve S connection.

Figure. 6.5 shows the spectral dependence of the intercept (see Fig. 6.4(d)) measured in a 1 meter spiral. There is, overall, a weak variation across the spectrum, however, the variation is larger than that inferred from the confidence interval in Fig. 6.4(d). We attribute this to the reduced length of this spiral and hence the smaller number of points used in the regression. Reducing the measurement window to 10 nm to study the spectral variation is also believed to have contributed to a larger variation.

Finally, we also characterized a S-connection design using a traditional clothoid curve. As shown in Fig. 6.6(a), a 2.5 dB insertion loss was inferred from high-spatial-resolution OBR measurements. This should be compared to the similar measurement (see inset in Fig. 6.4(c)) performed on the structure in Fig. 6.4(a). In that measurement no drop in backscatter level was observable. A micrograph of the clothoid connection is provided in Fig. 6.6(b). The clothoid curve starts at the origin (defined here as the center of the spiral) with zero curvature and its curvature varies linearly with its arc length. The other end of the clothoid needs to connect smoothly to the outside Archimedean spiral smoothly, which is not a trivial task and can introduce extra loss. The clothoid curve data were obtained using a tapered fiber coupler [35, 36] to couple to the interior arc (as opposed to end-fire coupling). This approach enables rapid testing of the structures.

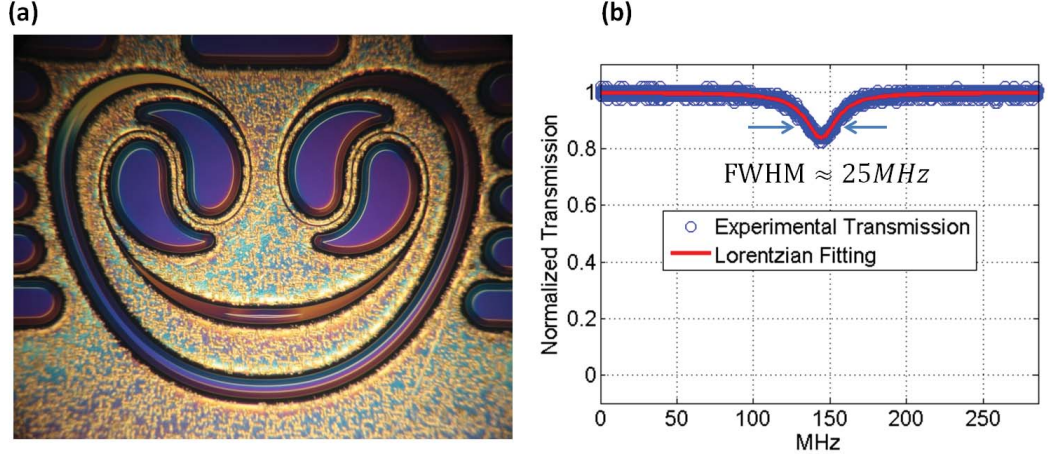


Figure 6.7: **(a)** An optical micrograph of a resonator with two connectors. This resonator has a round-trip length of  $1.5 \text{ cm}$ . Buffer patterns are introduced to achieve the uniform etching via loading effect. **(b)** A spectral scan for the case of a Q factor of  $8 \times 10^6$ .

### 6.3.2 Resonators measurements

The resonators consisting of two connectors are fabricated with the same procedure to create the waveguides (Fig. 6.7(a)). Again, the waveguide has a width of  $170 \mu\text{m}$  and the connector has a width of  $10 \mu\text{m}$ . During the dry etch, the two connectors are completely undercut. To measure intrinsic Q factor, the resonators are coupled to SMF-28 optical fiber using a fiber taper [35, 36, 45] and spectral lineshape data were obtained by tuning an external-cavity semiconductor laser across the resonance while monitoring transmission on an oscilloscope. To accurately calibrate the laser scan in this measurement, a portion of the laser output was also monitored after transmission through a calibrated Mach-Zehnder interferometer having a free spectral range of  $7.75 \text{ MHz}$ . Figure 6.7(b) shows a spectral scan obtained on a device having a Q factor of about 8 million. This resonator has a round trip physical length  $1.5 \text{ cm}$ . For a disk resonator with similar size, the Q factor is typically above 100 million [26]. The reduction of the Q is attributed to the two connections and it provides us an estimation of insertion loss which is given by

$$\alpha = \frac{\pi n L}{\lambda} \left( \frac{1}{Q_0} - \frac{1}{Q_{disk}} \right) \approx 0.046 \text{ dB} \quad (6.24)$$

where  $Q_0$  and  $Q_{disk}$  are the quality factor of our resonator and normal disk resonator,  $L$  and  $n$  is round trip and effect index of resonator. Thus, the insertion loss of a S-bend connector is approximately 0.023 dB. This value provides an upper bounded of connectors insertion loss. The nice resonance properties of this resonator also reveal the significance that our coupler not only prevent the loss in the propagation but also preserve the mode and avoid any cross talk loss. This mode preservation nature of our coupler is critical in application with the multi-mode waveguide.

### 6.3.3 Loss analysis

In our S-connector design, the waveguide length of connection is approximately 1 cm (with waveguide width  $10\ \mu\text{m}$ ). We compared measured insertion loss to attenuation calculations based upon atomic force microscope (AFM) roughness data [3, 26]. It shows that surface roughness scattering is the principle source of attenuation in the S connection [26], and the surface scattering loss is estimated to be 1.8 dB/m based on a model outlined in Ref. [3]. The increase in waveguide loss within the S-connection as compared to the Archimedean section of the spiral waveguide is a result of the reduced width of the S-connection waveguide. This width, as noted earlier, was reduced so as to relax the adiabaticity condition.

## 6.4 Summary

In this chapter, we present a variational approach to design of adiabatic optical waveguide connections. This algorithm is based on a coupled-mode theory and minimizes the inter-mode power coupling by appropriate design of curvature along a variational path. This optimization process can be implemented automatically and incorporated into mask-generating software. At the same time, it is general enough to cover most situations in optical circuit designs that connect two arbitrary waveguides. Because the approach is based on continuous adjustments to curvature it is less sensitive to dimension control in etching/fabrication of the waveguide in comparison with the offset approach. Meanwhile, the loss of the designed connector is insensitive to wavelength and provides good performance over a broad-band spectrum.

As a demonstration, a S-bend connector for spiral waveguides was designed and fab-

ricated. Backscattering measurements confirmed the excellent performance over 65 nm in the telecommunication band. Resonator measurement estimated a 0.023 dB insertion loss of this design. The measured loss originated mainly from surface scattering.

## Chapter 7

# Designs of Ultralow-Loss Spiral Waveguides

### 7.1 Introduction

The fabrication of wedge resonators and spiral waveguides both start with photomask designs that define the structure of devices [3,26]. Basically, resonator and waveguide patterns are generated with computer program such as MATLAB and then imported to AutoCAD. The resulting files are sent to photomask vendors for production. The generation of resonators' photomask is straightforward and easy. Radius is the only free parameter to be concerned. Since a few lines of code will do the job, it is acceptable to use throwaway code for their mask designs and generations. In contrast, photomask designs of spiral waveguides are not trivial and complicated by its constantly varying curvature and centimeter-scale footprint. They involve several subtle practical considerations such as undercut control, ultralow-loss inter-spiral connections and buffering patterns. In particular, the optical loss control in the spiral waveguide design is becoming critical in the light of the recent development of ultralow-loss optical waveguides [3, 21–23, 85]. With propagation loss less than 0.1 dB/m [3, 85], the additional loss imposed by connections in these structures must be addressed carefully. Meanwhile, since the generation of photomasks design of spiral waveguides may involve hundreds lines of codes, the desirable implementation of design program should offer reusability and be able to handle various requirements, such as number of cascade spirals and waveguide length. Specifically, it should be reused and modified easily to generate different spiral waveguide designs. Therefore, serious investigation is deserved to achieve successful and flexible designs of ultralow-loss spiral waveguides.

## 7.2 Design principles and implementations of spiral waveguides

The silica spiral waveguides are typically composed of multiple cascade individual spirals connected together [3]. Each individual spiral consists of two Archimedean-shaped spirals which are connected by a S-bend connection waveguide in the center. In addition, the buffering patterns are introduced to improve etching uniformity across the whole pattern. Figure 7.1 shows an example of waveguide design. It consists of two cascaded spirals connected together and input/output ports at the corners of the pattern. In the following sections, design principles of Archimedean spirals, S-bend connection, connection waveguide between individual spirals, input/output waveguides and buffering patterns will be discussed in detail.

### 7.2.1 Archimedean spirals

Archimedean spiral topology is used in almost all the on-chip waveguides [3, 22, 23] since it has the optimal area utilization. This spiral waveguide design features two embedded Archimedean-shaped spirals, one that brings light from the exterior to the interior and the other that returns the light to the exterior. In cartesian coordinate, they can be parameterized by  $\theta$  as

$$\begin{cases} x_c(\theta) = (R_0 + A \cdot \theta) \cdot \sin(\theta) \\ y_c(\theta) = (R_0 + A \cdot \theta) \cdot \cos(\theta) \end{cases} \quad (7.1)$$

where parameter  $R_0$  controls the starting position of the spiral and parameter  $A$  determines the distance between successive turnings. Yet, this function only defines an isolated line but not a waveguide with inner and outside boundary. To extend it to be a waveguide, two

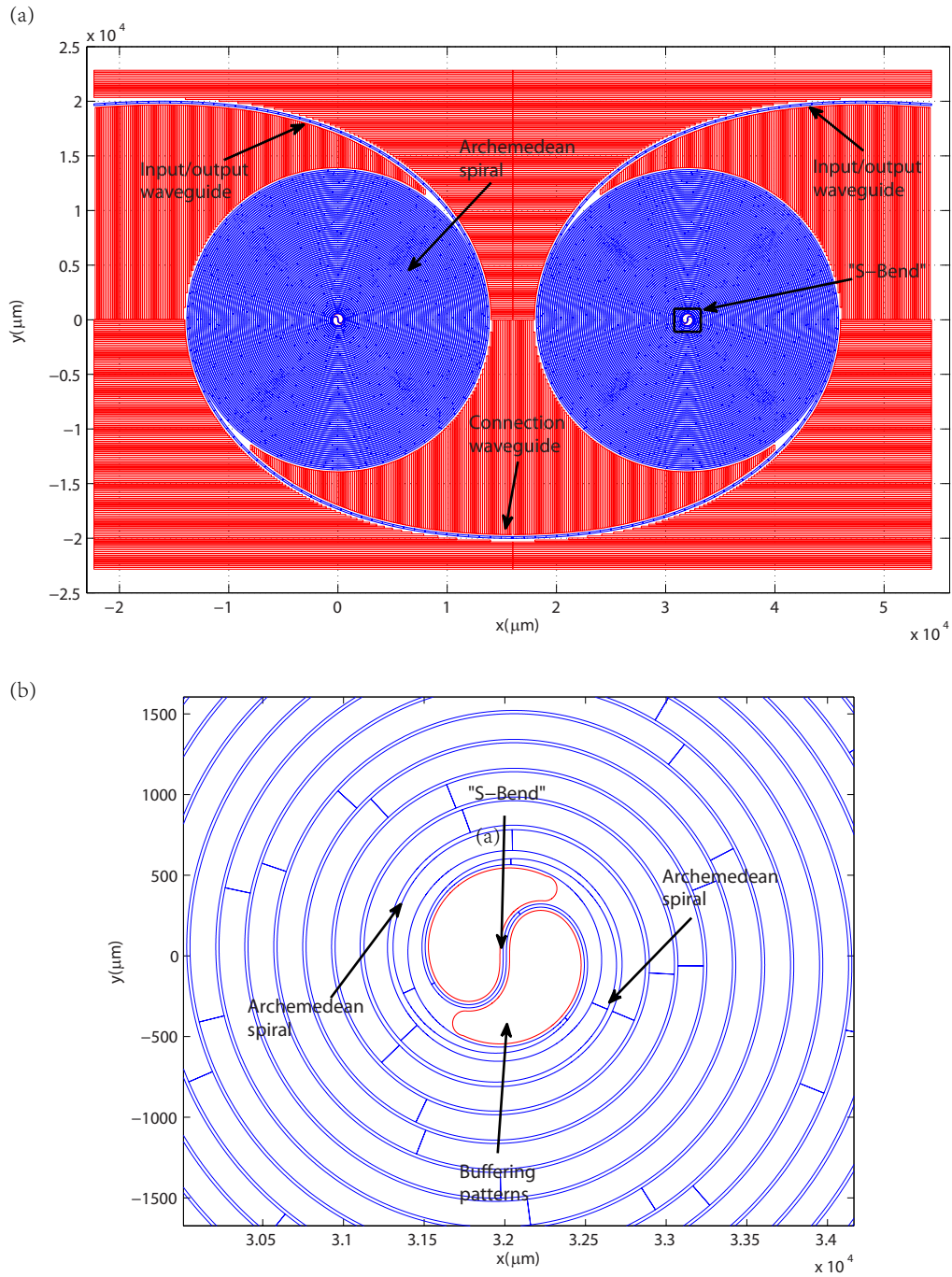


Figure 7.1: An example of spiral waveguide design. **(a)** A MATLAB-generated spiral waveguide design consists of two individual spirals. The surrounding red patterns are buffering patterns. **(b)** A zoom-in view of the center of spiral waveguide pattern. The red patterns in the center are buffering patterns to reduce the loading near the S-bend connection.

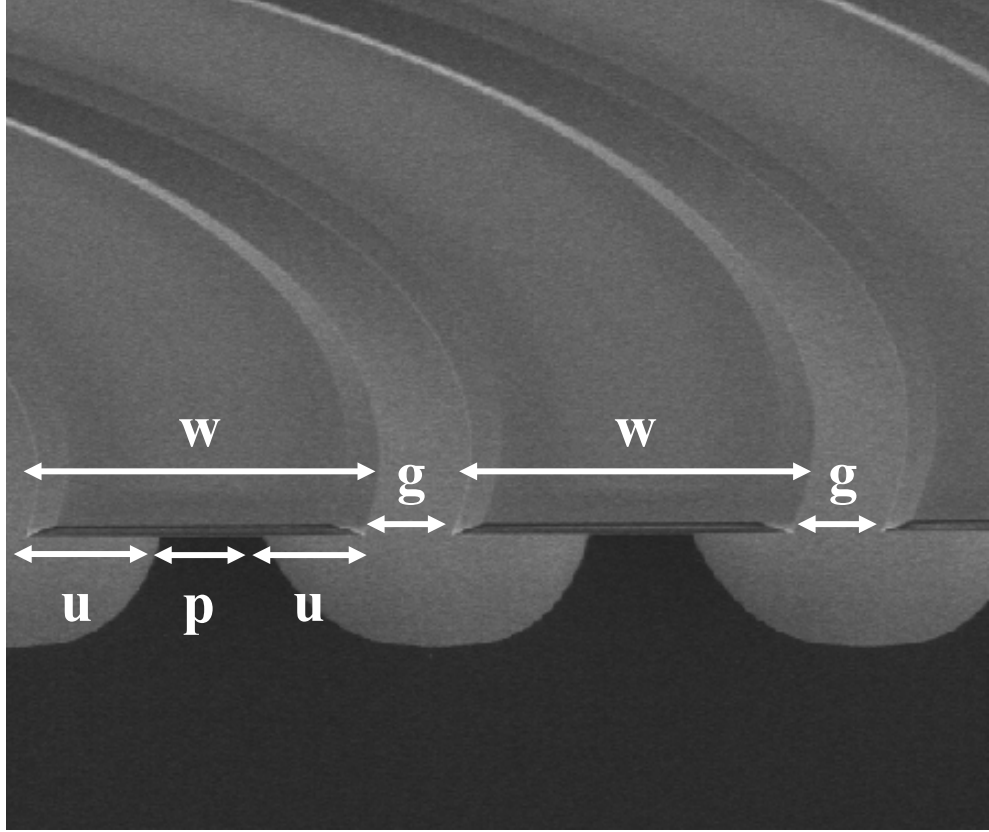


Figure 7.2: An SEM image showing a cross section of the Archimedean part of a spiral waveguide.  $w$  is the width of the waveguide;  $g$  is the separation between two neighbor waveguides;  $u$  is the silicon undercut; and  $p$  is the width of the supporting silicon pillar.

parallel lines  $((x_{in}, y_{in}),$  and  $(x_{out}, y_{out}))$  that define boundaries are found by

$$\begin{cases} x_{in}(\theta) = x_c(\theta) - n_x(\theta) \cdot w_{in}(\theta) \\ y_{in}(\theta) = y_c(\theta) - n_y(\theta) \cdot w_{in}(\theta) \end{cases} \quad (7.2)$$

$$\begin{cases} x_{out}(\theta) = x_c(\theta) + n_x(\theta) \cdot w_{out}(\theta) \\ y_{out}(\theta) = y_c(\theta) + n_y(\theta) \cdot w_{out}(\theta) \end{cases} \quad (7.3)$$

where  $(n_x(\theta), n_y(\theta))$  defines the normal vector of the curve in Eq.(7.1) and  $w(\theta) = w_{in}(\theta) + w_{out}(\theta)$  gives the width of waveguide.

The Archimedean part of spiral typically has a constant width and thus is characterized by three parameters: the starting size of the spiral ( $R_0$ ), the width of waveguide ( $w$ ) and separation between two neighbor waveguides ( $g$ ).  $R_0$  actually controls the size of the S-

Bend in the center, whereas  $w$  and  $g$  decide the parameter  $A$  in the Archimedean spiral via  $A = \frac{w+g}{\pi}$  (see Fig. 7.2). Figure 7.3 shows the total time delay achieved by a single-spiral waveguide with different outer radius and pitch sizes ( $w+g$ ). For example, spiral waveguide with 20 mm radius and 200  $\mu\text{m}$  generates about 30 ns delay which is equivalent to about 6.2 m physical length.

To achieve longer waveguide length in a given footprint, narrow waveguide is favorable.

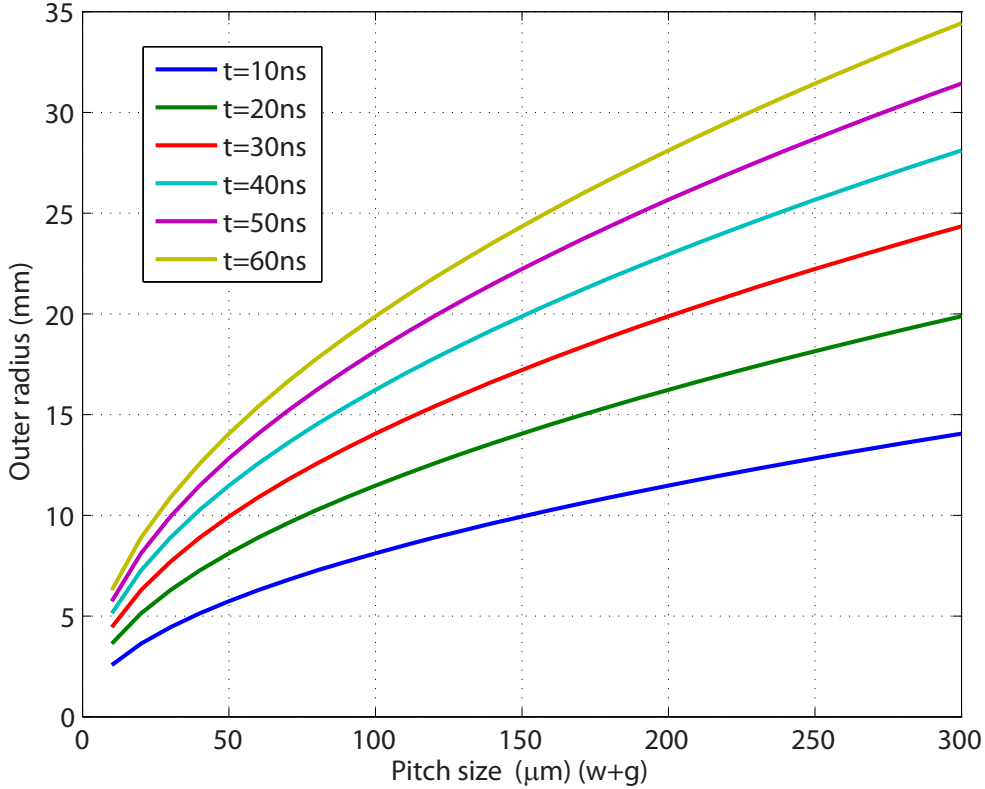


Figure 7.3: The total time delay achieved by a single-spiral waveguide with different outer radius and pitch sizes ( $w+g$ )

Yet, the minimum width of the waveguide ( $w$ ) is determined by required undercut ( $u$ ) and etching uniformity (see Fig. 7.2). Firstly, ultralow-loss operation requires sufficient silicon undercut to avoid interaction between lightwave in silica and silicon substrate. Take the cascade spiral shown in Fig. 5.3(c) as an example. Figure 7.4 summarizes the results of desired undercut for various waveguide structures based on finite element simulation. Basically, thicker oxide layer with smaller wedge-angle waveguide requires larger undercut

to preserve low-loss propagation. Also, larger undercut is required for waveguide with larger curvature radius. In practice,  $8 - 10 \mu\text{m}$  thick oxide is chosen for fabricating device with 27 degree wedge angle and the maximum curvature radius which occurs at the connections between spirals is around 20 cm.  $60-70 \mu\text{m}$  silicon undercut consequently becomes a typical requirement in fabrication. Secondly, the etching uniformity reflects itself by its impact of and the realized undercut and subsequently the width of supporting silicon pillar ( $p$ ). For example, if the xenon etching is not uniform, the wider supporting pillars are generally desirable as buffering to compensate the non-uniform etching. During the experiments, we typically have 5 – 10% etching non-uniformity across the entire pattern and it results in about  $5 \mu\text{m}$  difference in undercut among various locations of the chip. Therefore, designed width of the supporting pillar is set to be  $20 \mu\text{m}$ . In total, the minimum required width of the waveguide is  $140-160 \mu\text{m}$ .

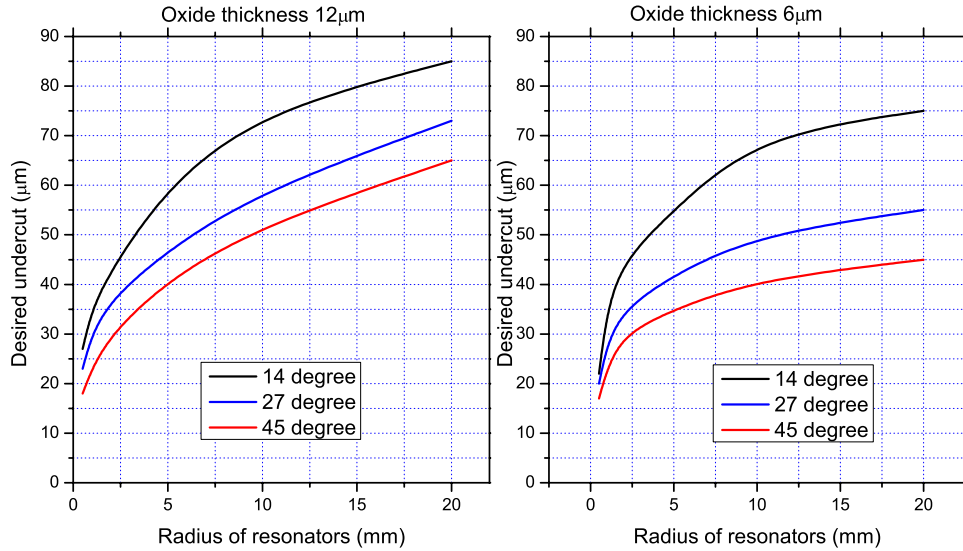


Figure 7.4: Desired undercut to avoid interaction between optical field and silicon pillar for oxide thickness  $6 \mu\text{m}$  and  $12 \mu\text{m}$  and wedge angle  $14^\circ$ ,  $27^\circ$ ,  $45^\circ$

### 7.2.2 S-bend connection waveguide

S-bend connection occurs in spiral waveguides wherein two interlaced Archimedean spirals (one clockwise and one counter clockwise) must be joined near the center of either spiral. In previous research [22, 23], the S-bend waveguide paths are normally constructed from sinusoidal curves, ellipses or other families of curves that are not necessarily the optimal choice.

With the algorithm describe in **Chapter 6** [25], we can design an optimal S-bend so as to minimize excitation of higher-order modes and smoothly connect to outside Archimedean spiral. A micrograph of the S-bend connection is shown in Fig.7.9(a).

S-bend connection waveguide is fully defined by two parameters  $R_0$  and  $A$  of the outside Archimedean spiral to which it connects [25]. As discussed above, parameter  $A$  is determined by the width of waveguide ( $w$ ) and separation between adjacent waveguides ( $g$ ). The only free parameter left here is  $R_0$  which will determine the size of the S-bend connection. Practically, there are both optical and mechanical concerns in optimizing the S-bend connection design. On one hand, the minimal optical insertion loss is favorable. On the other hand, since the S-bend connection design is completely undercut upon xenon difluoride etching, the thermal stress may bring serious impacts to the silica waveguide [40–42]. Specifically, the silica waveguide may suffer from cracks or even break completely (Fig. 7.5). Therefore, the size of S-bend connection deserves a careful investigation. Herein, we characterize the optical and mechanical properties of S-bend connection with various parameter  $A$  from  $50\ \mu\text{m}$  to  $600\ \mu\text{m}$  and provide guidance in optimizing its design.

Measurement of S-bend connection loss in waveguides is complicated by the insertion loss associated with coupling light into the waveguide. The resonator Q characterization provides one of the most reliable approaches [21]. We exploited closed-loop resonators consisting of two couplers (see Fig. 6.7) to extract the insertion loss of S-bend connection. By measuring its quality (Q) factor, the insertion loss can be extracted. The resonators consisting of two S-bend connection are fabricated. The dominated loss in these resonators is attributed to the two connections and it provides us that the insertion loss is given by

$$\alpha = \frac{\pi n L}{\lambda} \left( \frac{1}{Q_0} - \frac{1}{Q_{disk}} \right) \approx \frac{\pi n L}{\lambda Q_0} \quad (7.4)$$

where  $Q_0$  and  $Q_{disk}$  are the quality factor of our resonator and normal disk resonator with similar curvature,  $L$  and  $n$  is round trip and effect index of resonator. This value provides an upper bounded of connectors insertion loss. The optical performances of these structures are summarized in Fig. 7.6. Briefly, the large ( $A > 200\ \mu\text{m}$ ) S-bend connection designs suffer higher loss. It is because, in this regime, the dominate loss comes from surface scattering which will rise in S-bend connection since it has relative narrower waveguide compared to its Archimedean counterpart [25, 26]. The longer waveguide physical lengths

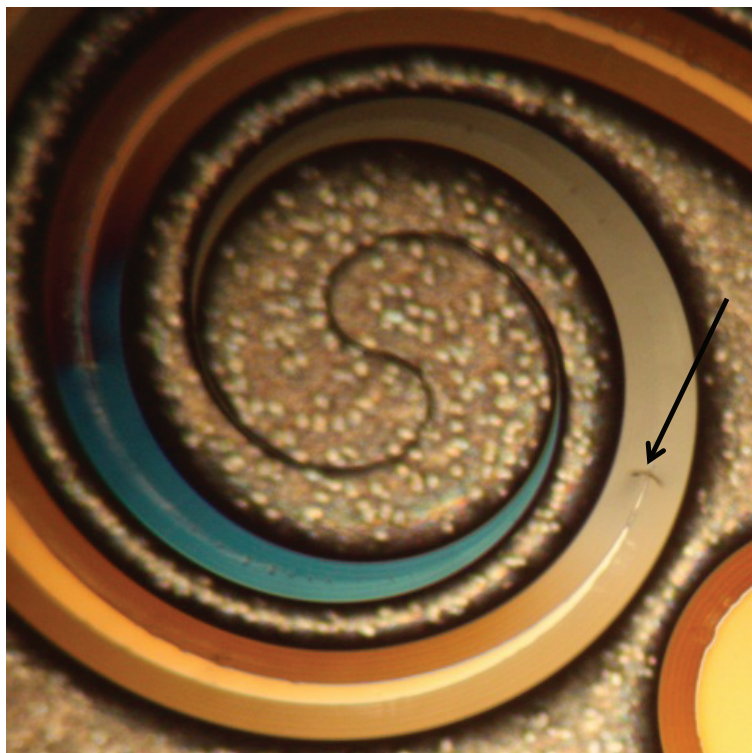


Figure 7.5: A microscope image of S-bend connection suffered from cracks. The black arrow indicates the position of crack.

of these designs bring higher insertion loss. The very small hand-offs ( $A < 100 \mu\text{m}$ ) S-bend connection designs are not satisfactory either. The rapid change of curvature brings inter-mode coupling and consequently higher optical loss [25]. Regarding to optical performance, the optimal value of size parameter  $A$  is between  $100 \mu\text{m}$  and  $200 \mu\text{m}$  and it will provide less than 0.02 dB insertion loss.

To evaluate the mechanical properties of these designs, we characterize the chance of presenting cracks in the S-bend connection waveguide after varied time of dry etching. As the time of etching changes, so does the deepness of undercut, which has significant impact on the mechanical stability of the S-bend connection. In particular, the S-bend connection design is completely undercut upon xenon difluoride etching. As the silicon undercut increase, the length of waveguide which is completely undercut will increase and it may intensify the cracking. Figure 7.7 shows the chance of having cracks for the S-bend connection with different size ( $A$ ) and silicon undercut. The size parameter  $A$  of  $125 \mu\text{m}$  turns out to be a good candidate considering its reasonable optical and mechanical

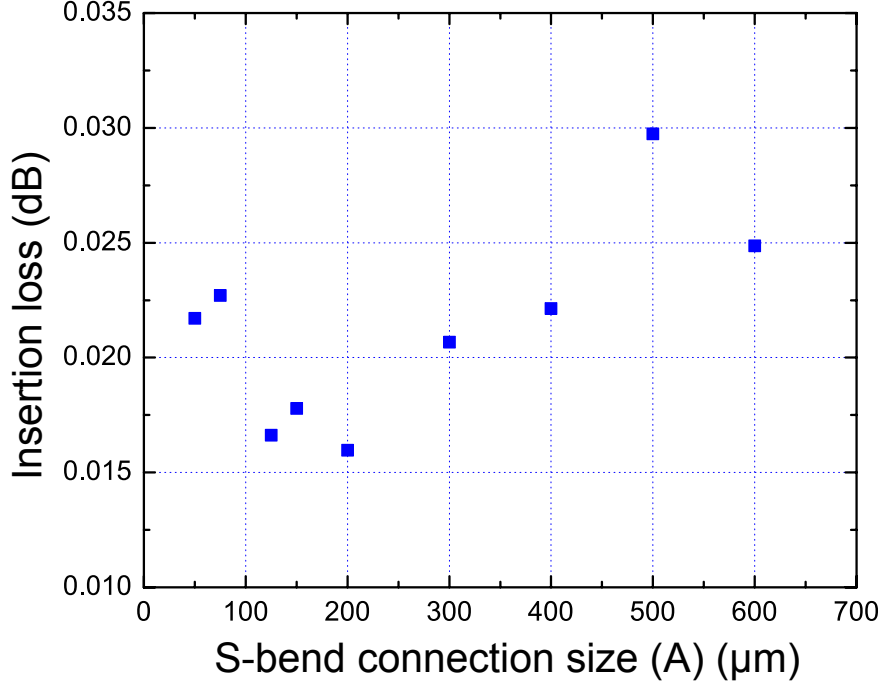


Figure 7.6: Loss measurements results of S-bend connection with various sizes ( $A$ )

performance.

### 7.2.3 Tapering of waveguide

As mentioned in **Chapter 6**, the narrow waveguide ( $10 - 20 \mu\text{m}$ ) is desirable in the S-bend region to avoid intermode coupling, whereas the Archimedean part of spiral requires wide width ( $\sim 150 \mu\text{m}$ ) to create sufficient undercut upon dry etching. To achieve a smooth connection between outside Archimedean spiral and inner S-bend connection, the width of waveguide need to be changed adiabatically. Mathematically, we are looking for a function  $f(x)$  such as

$$\begin{aligned}
 f(0) &= w_1 \\
 f(x) &\rightarrow w_2 \quad \text{as } x \rightarrow \infty \\
 f'(0) &= f''(0) = 0
 \end{aligned} \tag{7.5}$$

where  $w_1$  and  $w_2$  are the desired waveguide width of the S-bend and Archimedean spiral. The third condition in Eq.(7.5) will guarantee that the tapering will not disturb the contin-

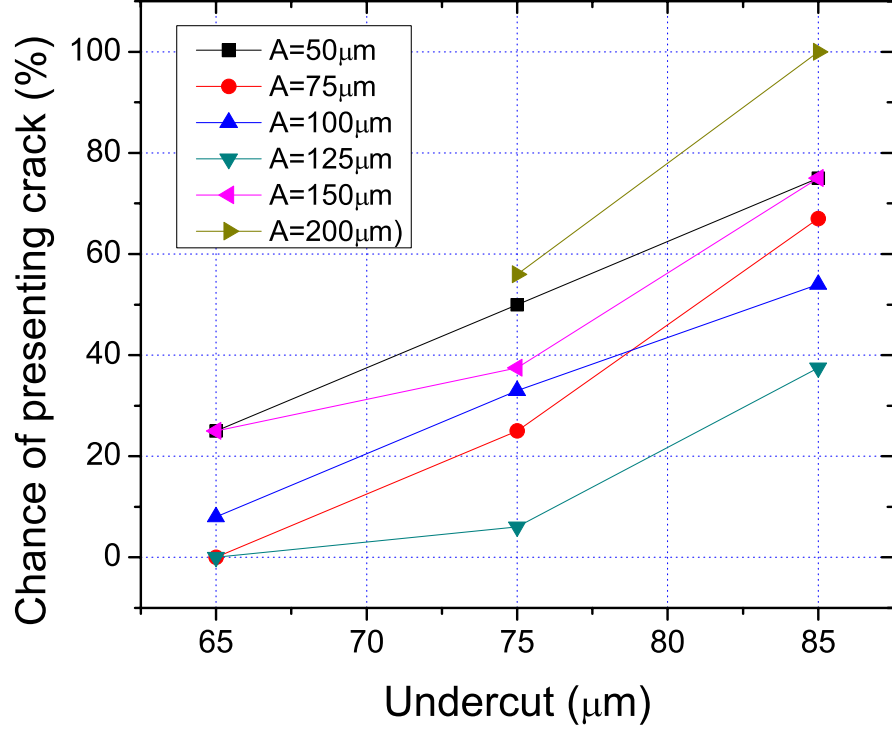


Figure 7.7: Chance of presenting cracks of S-bend connection with various sizes ( $A$ )

uous property of waveguide's tangential angle and curvature at this connection. A family of Hill functions satisfies these requirements becomes an ideal candidate of the tapering function.

$$H_{n,d}(x) = \frac{\left(\frac{x}{d}\right)^n}{1 + \left(\frac{x}{d}\right)^n} \quad (7.6)$$

where  $n$  and  $d$  are controllable parameters and  $n \geq 3$  is required for the third condition in Eq.(7.5). Specifically,  $n$  defines the steepness the tapering function and  $d$  gives the scale of the tapering region. Figure 7.8 gives a few realizations of  $H(n, d)$  function. The required function is then given by

$$f(x) = w_1 + (w_2 - w_1) \cdot H_{n,d}(x) = w_1 + (w_2 - w_1) \cdot \frac{\left(\frac{x}{d}\right)^n}{1 + \left(\frac{x}{d}\right)^n} \quad (7.7)$$

the width of waveguide in the Archimedean part that parameterized as in Eq.(7.1) is then

$$w(\theta) = w_1 + (w_2 - w_1) \cdot \frac{\left(\frac{\theta}{d}\right)^n}{1 + \left(\frac{\theta}{d}\right)^n} \quad (7.8)$$

Figure 7.9 shows an illustration of the tapering waveguide near the center of the spi-

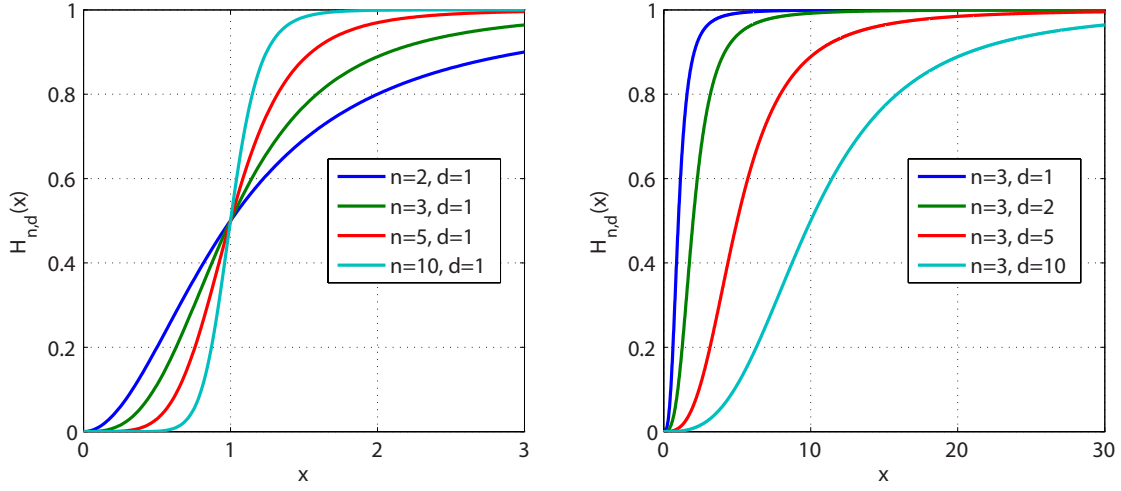


Figure 7.8: Examples of Hill function  $H_{n,d}(x)$

ral. The designed waveguide width of the S-bend connection region is  $20 \mu m$  whereas the Archimedean part of the spiral has the width of  $160 \mu m$ . A Hill function with  $n = 3$  and  $d = \pi$  is employed here to taper the waveguide and Archimedean spiral is parameterized as in Eq.(7.1).

With the same approach as in Section 7.2.2, we measure the insertion loss of designs

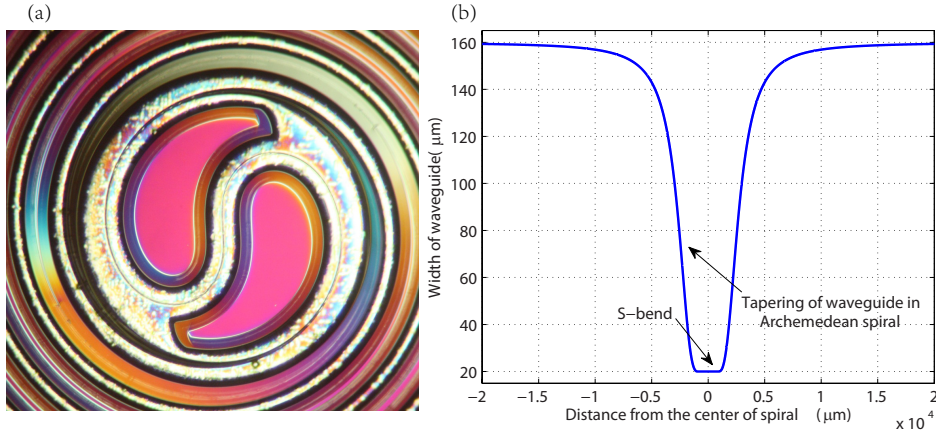


Figure 7.9: An example of tapered waveguide design. (a) A microscope image of tapering waveguide near the center of spiral. (b) A plot shows the width of waveguide in the tapering region

with various tapering rate. For the same S-bend connection with  $A = 500 \mu m$ , we varied

the  $d$  parameter in Hill function from (c.f. Eq.(7.8))  $0.5\pi$  to  $\pi$ . Figure 7.10 shows that slower tapering rate (larger value of  $d$ ) tends to provide less optical insertion loss. It may be attributed to the adiabatic requirement in varying the waveguide width.

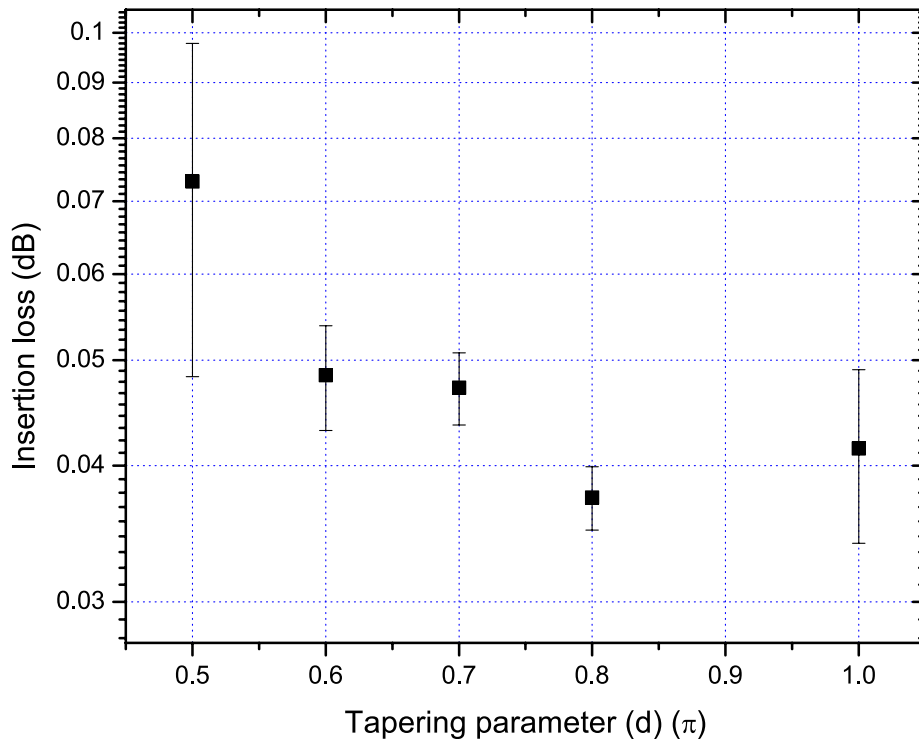


Figure 7.10: Loss measurement results of S-bend connection with various tapering rates ( $d$ ). The structure measured here has the same S-bend connection design with  $A = 500 \mu m$ .

#### 7.2.4 Connection and input/output waveguide

Besides the Archimedean spiral and S-bend connection, a complete design of spiral waveguides also requires linking two given points with minimal loss. Specifically, we are looking for the connection waveguide between individual spirals as well as the waveguide path guiding the lightwave in and out of the spiral waveguide (c.f. Fig. 7.1). The current design strategy is normally based on piecewise construction from a certain family of curves, such as ellipses and sinusoidal curves [84, 86, 87]. However, it is not clear that these families will always provide the best possible solution to the general problem of linking two points in an arbitrary optical circuit. In **Chapter 6** [25], we have introduced a general algorithm that minimizes the transition loss by avoiding excitation of higher-order optical modes. It can

be applied readily in establishing the connection between individual spirals.

As an illustration, we aim to connect two identical individual spirals with minimal loss (see the blue curves in Fig. 7.11). The starting point is at the end of Archimedean spiral with position  $(x_0, y_0)$ , tangential angle  $\theta_0$  and curvature  $\kappa_0$ . By symmetry, the end point  $(x_1, y_1)$  with tangential angle  $\theta_1$  and curvature  $\kappa_1$  may be chosen to be the middle point of this connection waveguide (see Fig. 7.11) and the other part of connection waveguide is then generated by a reflection as long as  $\theta_1 = \pi$ . We consider a family of curves with curvature given in terms of a cubic polynomial of arc length “ $s$ ” [25].

$$\kappa(s) = a_0 + a_1s + a_2s^2 + a_3s^3. \quad (7.9)$$

The coefficients of the polynomial ( $a_i$ ) and length of connection waveguide  $s_1$  are determined by matching the endpoint positions, endpoint tangents and the curvature between start and end points.

$$\begin{cases} a_0 = \theta_0 \\ \theta_1 = a_0 + \int_0^{s_1} \kappa(s) ds = \theta_0 + \int_0^{s_1} a_0 + a_1s + a_2s^2 + a_3s^3 ds \\ \kappa_1 = a_0 + a_1s + a_2s^2 + a_3s^3|_{s=s_1} \\ (x_1, iy_1) = (x_0, iy_0) + \int_0^{s_1} \exp(i\theta(s)) ds \end{cases} \quad (7.10)$$

By solving Eq.(7.10), a curve for the adiabatic connection is successfully defined as shown in Fig. 7.11.

### 7.2.5 Buffering patterns

In the most portion of spiral waveguide, the Archimedean topology offers the uniform loading upon the xenon difluoride etching. Nevertheless, since the cleaved samples typically have rectangular shapes and the waveguide pattern only covers part of the entire chip, the waveguide pattern will be surrounded by exposed silicon upon hydrofluoride etching. It creates extra loading during the xenon difluoride etching. Consequently, the etching rate at the outer of the pattern will be slower than its counterpart at the center and may fail to create enough undercut. Meanwhile, the S-bend connection also brings non-uniform loading during dry etching and deserves special treatment. To address this issue,

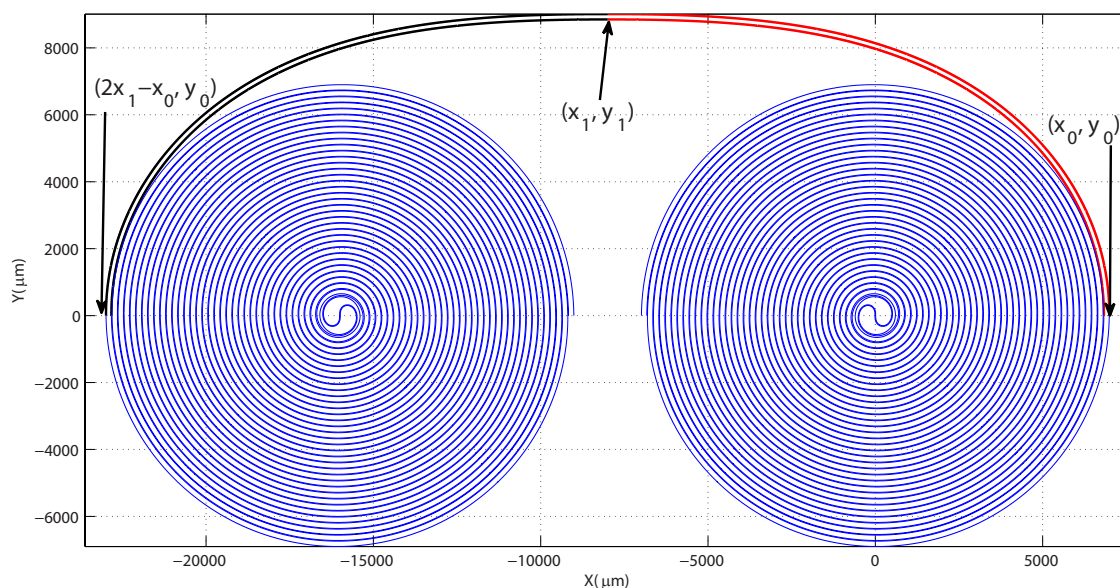


Figure 7.11: An example of establishing connections between two individual spirals. The blue curves outline two identical individual spirals to be connected. The red waveguide starts at  $(x_0, y_0)$  and ends at  $(x_1, y_1)$ . The black curve starts at and ends  $(2x_1 - x_0, y_0)$  at  $(x_1, y_1)$ .

the buffering patterns are introduced to improve the etching uniformity across the entire chip by maintaining uniform loading in the etching. Specifically, the buffering pattern aims to offer uniform loading across the entire sample. It can be achieved by keeping the ratio between the area of exposed silicon area and silica mask the same with buffering patterns. In the case of spiral waveguides, this ratio is determined by the width of waveguides ( $w$ ) and the gap between adjacent waveguides ( $g$ ). Therefore, the parallel rectangular patterns with width ( $2 \times w$ ) and gap ( $2 \times g$ ) are added to the area surrounding the waveguide (see Fig. 7.1). Herein, the width and gap of rectangular buffer is intentionally chosen to be  $2w$  and  $2g$  instead of  $w$  and  $g$  to avoid possible complete undercut of buffering patterns due to etching non-uniformity. At the same time, the complete undercut of S-bend connection is desired. To achieve this goal, two buffering patterns are introduced near the S-bend connection (Fig. 7.1(b) and Fig. 7.9(a)) to reduce the loading of dry etching. With the help of these patterning patterns, the etching rate difference can be reduced to as low as 5 – 10% across the entire chip.

### 7.3 Summary

In this chapter, we have demonstrated the design principles of ultralow-loss whisper-gallery spiral waveguides. The generation of Archimedean spirals, S-bend connection, connection and input/output waveguides and buffering patterns are presented with examples. The optical loss is carefully controlled across the entire chip. In particular, for the S-bend and the connection waveguide, adiabatic conditions are applied to minimize the transition loss by avoiding excitation of higher-order optical modes. In addition, the etching uniformity is address via the introduction of buffering pattern. The design guidance in this chapter provides great flexibility in designing of various waveguide structures.

## Chapter 8

# High-Sensitivity Nanoparticle Detection Using Optical Microcavities

### 8.1 Introduction

Generally, there are two detection approaches of nanoparticles: fluorescence-based detection and label-free detection. Although very sensitive, the fluorescence-based approach suffers from laborious labeling process [104]. In contrast, label-free detection is relatively easy to perform and has been an active research area with applications to biomolecular interactions as well as early-stage disease diagnosis. Several techniques have been explored [6,6,105–110], and among these, microcavity sensors in the form of whispering gallery resonators have received considerable attention. In this method, a particle or molecule binding on the surface of the microcavity perturbs its optical properties, causing a resonant wavelength shift with magnitude that depends upon the particles polarizability (proportional to volume for macroscopic particles). Measurement of the shift enables observation of binding events in real time and can also be used to assess particle size. Silica microspheres [111] or silica microtoroids [4,10] provide an easily functionalized detection surface that directly interacts with a high-quality-factor ( $Q$ ) whispering gallery mode. The combination of small size and high  $Q$  endows these devices with excellent detection sensitivity. Based on this platform, there are two distinct mechanisms of label-free detection: the reactive mechanism and therm-optic mechanism. We will discuss them in the following sections.

## 8.2 Reactive mechanism wavelength shift

The binding of nanoparticles to the surface of microresonator will interact with its evanescent field. It slightly perturbs the optical path length of the resonance, and consequently shift the resonance towards longer wavelength [6, 106, 112, 113]. Specifically, Individual binding events will then produce discrete step in the time trace of the resonance wavelength signal.

### 8.2.1 Perturbation theory

There are a few different ways to calculate the “reactive” shift due to the attachment of nanoparticle [6, 106, 112, 113]. One of the simplest approach is to use quantum argument. The particles that attached to the resonator will interact with a whispering-gallery mode. The evanescent field will polarize the nanoparticle and consequently reduce its own energy. With the number of cavity photon unchanged, the frequency of each one is shifted by  $\Delta\omega$ . If we assume that the particle is small compared to the wavelength, with a nano-particle at position, we have  $\vec{r}_i$

$$\hbar\Delta\omega \approx \frac{\alpha}{2} \langle |\vec{E}(\vec{r}, t_i)|^2 \rangle \quad (8.1)$$

where  $\alpha$  is the excess polarizability of the nanoparticle,  $\langle |\vec{E}(\vec{r}, t_i)|^2 \rangle$  is the time average of the square of the fields at  $\vec{r}_i$ . By dividing by the single photon energy, the reactive shift due to a single particle attachment to cavity at  $r_i$  is given by

$$\frac{\Delta\omega}{\omega} \approx \frac{\Delta\lambda}{\lambda} = \frac{-\Delta\alpha |\vec{E}(\vec{r}_i)|^2}{2 \int \epsilon(\vec{r}) |\vec{E}(\vec{r})|^2 dV} \quad (8.2)$$

Or equivalently

$$\frac{\Delta\omega}{\omega} \approx \frac{\Delta\lambda}{\lambda} = \frac{-\frac{\Delta\alpha}{\epsilon_0} |\vec{E}(\vec{r}_i)|^2}{2 \int \epsilon_r(\vec{r}) |\vec{E}(\vec{r})|^2 dV} \quad (8.3)$$

where  $\epsilon(\vec{r})$  ( $\epsilon_r(\vec{r})$ ) is the dielectric (relative) constant at position  $\vec{r}$ . From this expression, the shift in resonant frequency can be readily calculated if the field of the whisper-gallery mode and the excess polarizability are known.

Substance	Mass	$\frac{\Delta\alpha}{\epsilon_0}$	Max. possible frequency shift
Protein G	26.1 kDa	20.59 nm <sup>3</sup>	1.33 kHz
IL2 antibody	~ 150 kDa	118.3 nm <sup>3</sup>	7.65 kHz
BSA	66.4 kDa	52.38 nm <sup>3</sup>	3.39 kHz
Streptavidin	60 kDa	47.33 nm <sup>3</sup>	3.06 kHz

Table 8.1: Perturbation brought by proteins. The frequency shifts are estimated based on a microtoroid with major diameter 80  $\mu\text{m}$  and minor diameter 6  $\mu\text{m}$  with a fundamental whispering gallery mode at 680 nm wavelength.

### 8.2.2 Estimation of the reactive shift by proteins or virus

Protein has the convenient property of raising the refractive index of an aqueous solution by nearly the same amount for the same mass concentration. The differential refractive index of protein in an aqueous buffer is given by  $dn/dc \approx 0.18 \text{ cm}^3/\text{g}$  (at visible wavelength) [113]. The excess polarizability is related to  $dn/dc$  and the molecular mass  $m$  via

$$\frac{\Delta\alpha}{\epsilon_0} = 2n_s \frac{dn}{dc} m \quad (8.4)$$

where  $n_s$  is the refractive index of surrounding solution. Table 8.1 gives a few examples of perturbation brought by single proteins attaching to the surface. As for the virus, we can not assume that the size of particle is so small that the variation of electrical field within its volume will be negligible. Instead, the field within the virus has been numerically averaged based on the spherical assumption of the virions shape. The maximum shift (*i.e.*, equatorial) associated with a single bio-particle interaction is

$$\frac{\Delta\omega}{\omega} \approx \frac{-\frac{\Delta\alpha}{\epsilon_0} \int_{virus} |\vec{E}(\vec{r})|^2 dV}{2 \int \epsilon_r(\vec{r}) |\vec{E}(\vec{r})|^2 dV} \quad (8.5)$$

In particular, InfA virions have an average radius 50 nm [114]. To estimate its reactive shift, the mass  $m$  can be found from the sedimentation in density gradients based on a statistical number of viruses to be 0.5 fg [115]. Thus, the perturbation of polarizability is supposed to be  $\frac{\Delta\alpha}{\epsilon_0} = 2.38 \times 10^5 \text{ nm}^3$ . Table.8.2 lists the estimated shift by the attachment of infA at for microtoroids with different structures.

Major Diameter	Minor Diameter	Max. Possible $\Delta f$	Max. possible $\Delta\lambda$
97 $\mu\text{m}$	13 $\mu\text{m}$	7.00 MHz	10.36 fm
86 $\mu\text{m}$	15 $\mu\text{m}$	9.03 MHz	13.25 fm

Table 8.2: The estimated frequency (wavelength) shift caused by an InfA viron ( $\lambda \approx 680\text{ nm}$ ).

### 8.3 Experimental results: reactive shift

Typically, measurements proceed by monitoring the transmission spectrum of a selected microcavity resonance. Wavelength shifts of the resonance, caused by particle binding, are measured by interpreting the scan voltage used to repetitively sweep the wavelength of a probe laser. Although the ultimate precision in measuring a shift depends upon the microcavity linewidth (and hence its Q factor), the conversion of the scan voltage to wavelength provides a significant source of error even greater than the microcavity linewidth when Q factor is in the range of 10–100 million. Indeed, the long-term frequency jitter associated with many commercial tunable lasers exceeds the linewidth of high-Q resonators such as microtoroids [4,10]. The stability of the mechanical scanning mechanism can also introduce error. Each of these sources of error are uncorrelated with the scan voltage.

#### 8.3.1 Experiment setup

We introduce a reference interferometer into the detection system to minimize the error contributions from frequency jitter and laser scan-voltage control. With this approach, a wavelength shift as small as several 10ths of a femtometer can be detected. No feedback control or stabilization of the laser system is provided (although this could be added). The experimental setup is shown in Fig. 8.1. A 680 nm tunable laser (Newport Velocity 6304) is driven by a voltage ramp signal, and the output of the laser is split into two branches by a directional coupler. In one branch the laser power is used to monitor the resonance of a microtoroid immersed in an aqueous bath containing nanoparticles or biomolecules. Optical coupling to the microtoroid proceeds using a fiber taper [35, 36, 45], before the signal is photodetected. Typically, the coupled power was kept in the range of 10  $\mu\text{W}$ . In the other branch, the laser frequency is monitored using a reference interferometer. The interferometer features two fiber optic paths of differing lengths, and is immersed in an ice-water bath within a 1 ft<sup>3</sup> thermally and mechanically insulated Styrofoam enclosure.

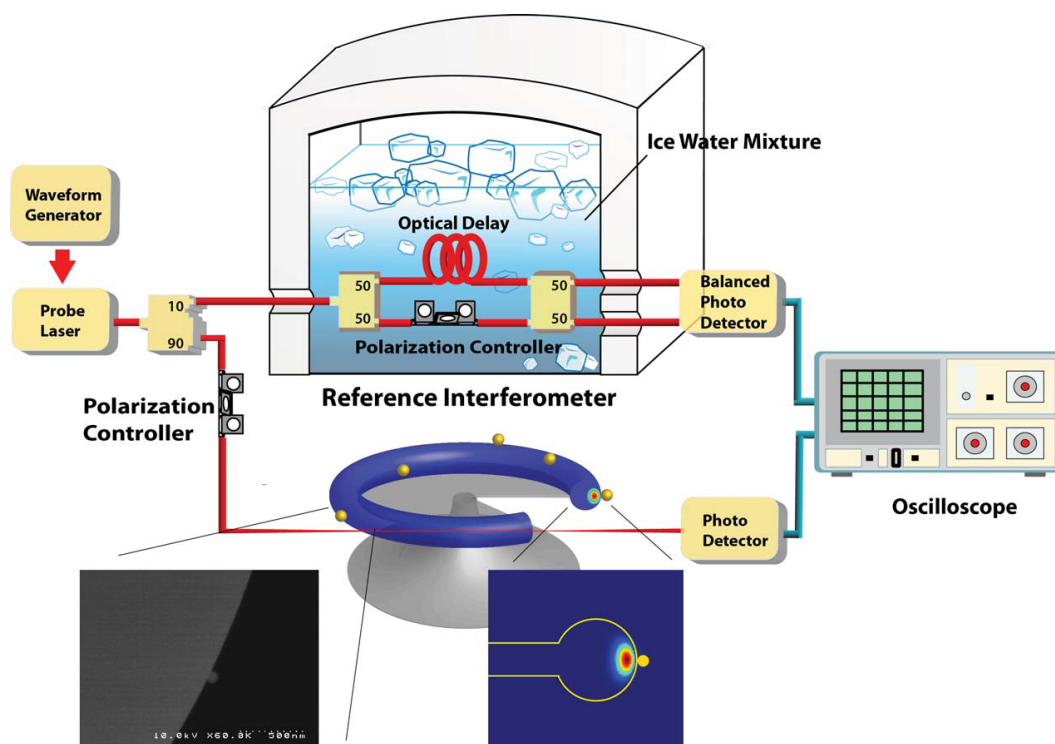
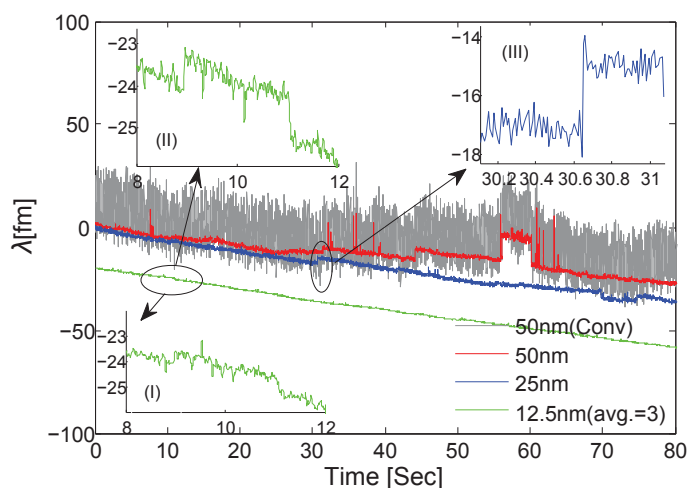


Figure 8.1: Experimental setup for nanoparticle and biomolecule detection using a temperature-stabilized reference interferometer. The output of a tunable laser is split into two branches by a 90/10 coupler. One branch is coupled into/out of a microtoroid resonator in an aqueous environment. The other branch is coupled into a reference interferometer to monitor the laser optical frequency in real time. Immersion of the reference interferometer in an ice-water bath provides long-term frequency stability. (Inset) SEM micrograph of a  $R = 25$  nm bead binding on the surface of a microtoroid

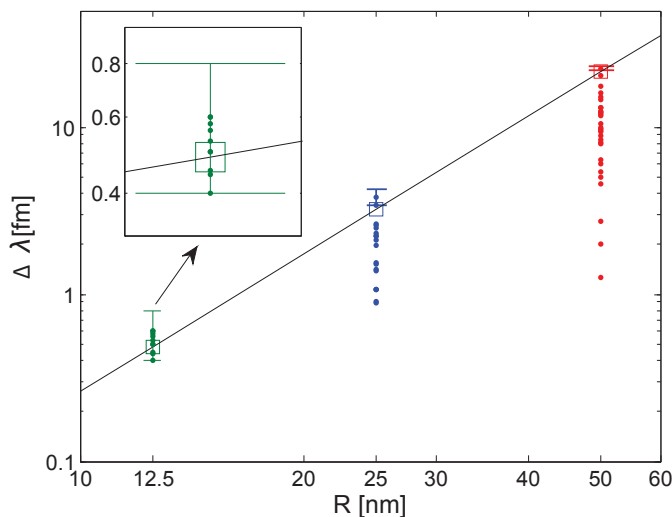
The interferometer is allowed to thermally stabilize for several hours before use. The free spectral range (FSR) of the interferometer was 40.8 MHz (corresponding to a 4.9 m differential length in the two fiber optic paths) for measurement of 12.5 and 25 nm radius bead binding. This FSR value was sufficiently wide so as to minimize the likelihood of the laser jittering beyond one FSR during typical measurement intervals. In 50 nm radius bead measurements, an FSR of 235 MHz (equivalent 0.9 m differential length) was used to ensure the maximum step size caused by bead binding events would be smaller than the FSR. The dual outputs of the interferometer were detected using a balanced homodyne detector (Thorlabs PDB120A, noise equivalent power 6 pW/pHz) to reduce contributions from laser power noise. Polarization was adjusted using a polarization controller (shown in Fig. 8.1). Because the photodetected output of the reference interferometer depends sinusoidally on the frequency of the laser (period set by interferometer FSR), the laser frequency (relative to an initial value) can be accurately measured (as opposed to being inferred by the scan voltage) at the moment when the microcavity resonance is excited in the other branch, which greatly reduces measurement noise, as demonstrated below.

### 8.3.2 Polystyrene nanobeads detection

To test the system, measurements were first performed using polystyrene beads at three distinct sizes. Beads in solution were obtained from Polyscience except for the 12.5 nm beads which were obtained from Phosphorex. A syringe pump was used to inject a solution into a microaquarium containing a fiber-taper-coupled, microtoroid resonator. After the solution containing beads was introduced into the aquarium, the syringe pump was turned off for the actual measurement to reduce fluctuations that are believed to be associated with hydrodynamic-induced instabilities in the taper-microtoroid coupling. Fig 8.2a displays representative resonance wavelength versus time traces (sampled at a 10 ms interval) for solutions of polystyrene beads of radius  $R = 50$  nm (red line),  $R = 25$  nm (blue line), and  $R = 12.5$  nm (green line). The corresponding in-solution quality factors of the microtoroids used in these measurements were  $8 \times 10^6$ ,  $3 \times 10^7$ , and  $1 \times 10^8$ , respectively. The higher values here should be taken as approximate. Even though coupled power levels were maintained low in the range of  $10 \mu\text{W}$  to minimize thermal effects, some thermal effects were nonetheless present in the higher-Q devices. The 50 and 25 nm nanobeads were diluted in Dulbeccos Phosphate Buffered Saline (DPBS) to achieve a concentration of 1 pM. To enhance the



a)



b)

Figure 8.2: Resonant wavelength data from nanobead detection measurements. **(a)** Resonance wavelength shift vs. time for binding of  $R = 50$  nm (red),  $R = 25$  nm (blue), and  $R = 12.5$  nm (green) polystyrene nanobeads. In  $R = 12.5$  nm bead experiments, the shift of the split-resonance center wavelength (Inset I) as well as the shift of longer-wavelength resonance (Inset II) are presented. For comparison, the gray trace is the same data run as the red trace, but using the conventional sweep voltage method. **(b)** Histogram of measured binding-induced step sizes for beads of radius  $R = 12.5$  nm (green), 25 nm (blue), and 50 nm (red). The squares are the predicted maximum shift from a finite element calculation. Error bars give  $\sqrt{2}\sigma$  where  $\sigma$  is the standard deviation of 10 measured points before the measured step. Inset shows a magnified view for the 12.5 nm bead data.

probability of observing a maximum resonance shift, a 100 pM solution was used for  $R = 12.5$  nm bead detection, and the shift was measured with a three-point moving average to reduce noise.

In Fig. 8.2A, steps of 2.7, 6.4, and 12.3 fm at 31.4, 44.2, and 56.2 s, respectively, are present in the  $R = 50$  nm scan (red trace), suggesting individual particle binding events. At 60.2 s, there is also a step down in the red trace suggesting that a bead has desorbed. The standard deviation for this measurement is 0.6 fm. For comparison purposes, the gray trace in the figure shows the same data scan except using the conventional scan-voltage method (i.e., without jitter compensation provided by the reference interferometer).

For the  $R = 25$  nm beads, a step of  $2.6 \pm 0.5$  fm is observed at 30.6 s as displayed in the upper right inset, and steps of 1.5 and 2.2 fm are observed at 41.8 and 74.7 s, respectively. Finally, a step of  $0.4 \pm 0.2$  fm for the case of  $R = 12.5$  nm beads is observable in the green trace at 11 s with an SNR of 2. Here, the step amplitude can be enhanced by measuring on the longer-wavelength resonance (see Fig. 8.2A, Inset II) as both the average resonance wavelength and the split frequency increase upon binding. Indeed, this useful mechanism boosts the observed amplitude by over a factor of 2 ( $1.0 \pm 0.2$  fm). The step sizes appearing in the blue and green traces should be contrasted with the noise level of the gray trace.

Measured wavelength-shift step sizes from many measurements using different microtoroids and bead sizes are compiled in Fig. 8.2b. The data presented were compiled from 51, 11, and 15 distinct runs in which 10, 25, and 43 identifiable binding events were observed using  $R = 12.5$  nm (green cross),  $R = 25$  nm (blue cross), and  $R = 50$  nm (red cross) beads, respectively. Various particle concentrations ranging from 0.1 to 100 pM were also tested during the measurements. For the smallest beads, femtomolar-range concentrations were insufficient to produce binding events of sufficient frequency and amplitude to observe. The amplitude of a binding/unbinding-induced wavelength step is determined by both the particle size and its proximity to the optical whispering gallery mode. Maximum shift occurs when the particle binds at the equator of the microtoroid where the optical field is maximum. This maximum value (computed using COMSOL [27]) is provided in Fig. 8.2. For the largest particle size, we found it necessary to account for the actual field variation within the particle. Error bars were obtained by computing the variance of 10 data points in the vicinity of the measured step. In addition to the measurement uncertainty, there is also a variation in toroid major diameter and bead diameter, both approximately 15%.

### 8.3.3 Influenza A virion detection

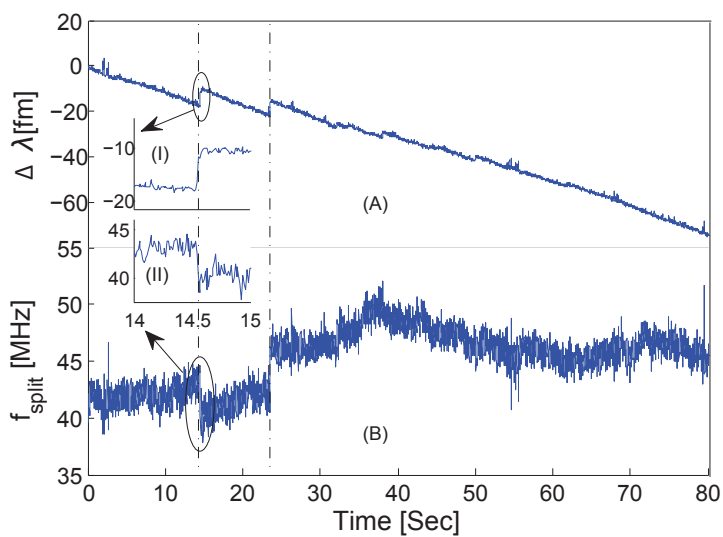
To test the method for bio-sensing, binding of InfA virion diluted in DPBS was measured. Fig. 8.3a (trace A) provides a typical data scan in which virus binding is observed at a concentration of 1 pM. At 14.5 s, an  $8.4 \pm 0.3$  fm step is observed (also magnified in Fig. 8.3a, Inset I). Steps are also observed at (23.6 s:6.0 fm), (32.1 s:2.2 fm), (33.5 s:2.3 fm), and (38.1 s:2.4 fm), to indicate a few. Fig. 8.3B provides the histogram of binding counts and the corresponding step size over eight runs. In contrast to the bead experiments, unbinding events were less frequent, indicating a much stronger affinity force between InfA and the toroid surface. A maximum shift of  $11.3 \pm 0.3$  fm was observed in Fig. 8.3(b), Inset, yielding an SNR of 38 and representing an improvement over the previously reported SNR of 3 [6]. This result also agrees with the simulation.

## 8.4 Thermo-optic effect wavelength shift

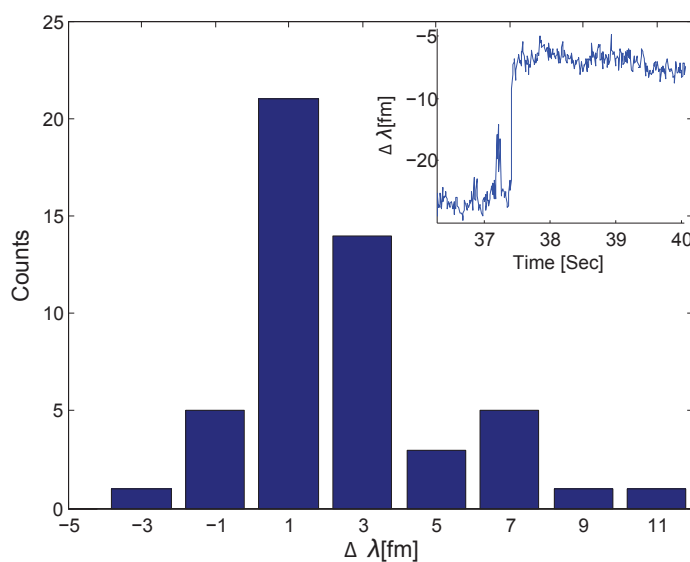
Besides the reactive mechanism discussed above, it is recently reported experimentally thermo-optic mechanism will bring protein frequency shifts more than 1000 times the reactive projections [105]. Yet, this result is challenged later on [116]. Herein, we discussed the physics of thermo-optic effect and its experimental implications.

### 8.4.1 Derivation of thermo-optic wavelength shift

The thermo-optic mechanism works by heating the protein/nanoparticle through its absorption. Local heating of the resonator is then caused by the heat transfer from the attached protein/nanoparticle and it introduced an additional change in local refractive index as characterized by the thermo-optic coefficient. The change of refractive index will induce an enhanced thermo-optic resonance wavelength shift. We adapt a derivation outlined in Ref. [116] which starts by estimating the heat  $h$  generated by the absorption of the energy from the whispering-gallery mode by the attachment of polystyrene beads at position  $\vec{r}_a$ .



a)



b)

Figure 8.3: (a) Resonance wavelength shift (scan A) and splitting frequency shift (scan B) of a microtoroid immersed in a 1 pM InfA solution. Many steps are visible in scan A, including a step of  $8.4 \pm 0.3$  fm (magnified within Inset I). The same event is detected as a split frequency shift in scan B (magnified within Inset II). A histogram of measured, resonance wavelength-shift steps is provided in (b) and includes a maximum wavelength step of 11.3 fm (displayed within the inset of (b)).

The heat produced by a beads with absorption cross section  $\sigma$  is given by

$$\begin{aligned}
h &= \sigma \langle |\vec{S}(\vec{r}_0)| \rangle = \sigma \langle |\vec{E}(\vec{r}_0) \times \vec{H}(\vec{r}_0)| \rangle \\
&= \frac{1}{2} \sigma \sqrt{\frac{\epsilon(\vec{r}_0)}{\mu(\vec{r}_0)}} |\vec{E}(\vec{r}_0)|^2 \\
&= \frac{\epsilon(\vec{r}_0)c}{2n} |\vec{E}(\vec{r}_0)|^2 \sigma
\end{aligned} \tag{8.6}$$

where  $\langle \dots \rangle$  is the time average,  $n$  is the effective mode index. Then, we relate  $\vec{E}(\vec{r}_0)$  to the circulating power in the whispering-gallery mode (WGM), which, at steady state, is given as

$$W = \frac{PQ}{\omega} = \frac{1}{2} \int_c \epsilon(\vec{r}) |\vec{E}(\vec{r})|^2 dV \tag{8.7}$$

where  $Q$  is the total quality factor of the resonator and  $P$  is the power that coupled into the WGM. Meanwhile, the integral contains the volume the cavity. If we introduce the optical mode volume of WGM, which is defined as

$$V = \frac{\int_c \epsilon(\vec{r}) |\vec{E}(\vec{r})|^2 dV}{\max[\epsilon(\vec{r}) |\vec{E}(\vec{r})|^2]} \tag{8.8}$$

and normalized the electrical field  $\vec{E}(\vec{r})$  as

$$|\vec{u}(\vec{r})|^2 = \frac{\epsilon(\vec{r}) |\vec{E}(\vec{r})|^2}{\max[\epsilon(\vec{r}) |\vec{E}(\vec{r})|^2]} \tag{8.9}$$

The heat generation at  $\vec{r}_0$  could be written as

$$\begin{aligned}
h &= \frac{c}{2n} \sigma |\vec{u}(\vec{r}_0)|^2 \max[\epsilon(\vec{r}) |\vec{E}(\vec{r})|^2] \\
&= \frac{c}{2nV} \sigma |\vec{u}(\vec{r}_0)|^2 \int_c \epsilon(\vec{r}) |\vec{E}(\vec{r})|^2 dV \\
&= \frac{c}{nV\omega} \sigma PQ |\vec{u}(\vec{r}_0)|^2 = \frac{\sigma \lambda PQ}{2\pi nV} |\vec{u}(\vec{r}_0)|^2
\end{aligned} \tag{8.10}$$

Then, we calculate the temperature increase caused by the heat source above. Since the sensing experiment are carried out over seconds and the thermal relaxation time of the toroid is microseconds. We may assume that the induced temperature change is in steady state. The temperature elevation distribution can be found from the solution to the Green's

function

$$\kappa(\vec{r})\nabla^2 T(\vec{r}) = -h\delta(\vec{r} - \vec{r}_0) \quad (8.11)$$

where  $\kappa(\vec{r})$  is the thermal conductivity. The majority of the optical field intensity (over 90%) resides within the toroidal boundary [105]. This fact and the similar magnitudes of the thermal conductivity of water and silica (0.6 and 1.38 W/mK) make it possible to attribute all thermal tuning in (and, indeed, the shape of the thermal plume) to the silica. We basically treat the thermal conductivity as a constant ( $\kappa$ ) over all the space and it yields

$$\delta T(\vec{r}) = \frac{h}{4\pi\kappa|\vec{r} - \vec{r}_0|} \quad (8.12)$$

The temperature increase causes a change in refractive index in the toroid through the thermo-optic effect (*i.e.*,  $\delta n = (dn/dT)\delta T$ ). The refractive index change is

$$\delta n(\vec{r}) = \frac{\sigma\lambda dn/dT}{8\pi^2 n\kappa V} PQ \frac{|\vec{u}(\vec{r}_0)|^2}{|\vec{r} - \vec{r}_0|} \quad (8.13)$$

based on which we could estimate the wavelength shift  $\delta\lambda$  due to the thermo-optic effect. From the standard first-order perturbation theory [106]

$$\frac{\delta\lambda}{\lambda} = \frac{\int \Delta\alpha(\vec{r})|E(\vec{r})|^2 dV}{2 \int_c \epsilon(\vec{r})|E(\vec{r})|^2 dV} = \frac{\int \delta(n(\vec{r})^2)|E(\vec{r})|^2 dV}{2 \int_c n(\vec{r})^2|E(\vec{r})|^2 dV} \quad (8.14)$$

Again, if we attribute all thermal tuning in to the silica and using the fact the principal energy is inside the toroid, the integral could be restricted to the toroid.

$$\frac{\delta\lambda}{\lambda} = \frac{\int \delta(n(\vec{r}))|\vec{E}(\vec{r})|^2 dV}{n_s \int_{toroid} |\vec{E}(\vec{r})|^2 dV} \approx \frac{\int \delta(n(\vec{r}))|\vec{u}(\vec{r})|^2 dV}{nV} \quad (8.15)$$

We finally arrived at the thermo-optic wavelength shift induced by a polystyrene beads at  $\vec{r}_0$

$$\frac{\delta\lambda}{\lambda} = \frac{\sigma\lambda \frac{dn}{dT}}{8\pi^2 n^2 \kappa V} PQ \frac{|\vec{u}(\vec{r}_0)|^2}{V} \int \frac{|\vec{u}(\vec{r})|^2}{|\vec{r} - \vec{r}_0| + \epsilon} dV \quad (8.16)$$

Or equivalently

$$\delta f = \frac{\sigma c \frac{dn}{dT}}{8\pi^2 n^2 \kappa V} PQ \frac{|\vec{u}(\vec{r}_0)|^2}{V} \int \frac{|\vec{u}(\vec{r})|^2}{|\vec{r} - \vec{r}_0| + \epsilon} dV \quad (8.17)$$

Here we introduce a parameter  $\epsilon$ , which is on the order of the physical radius of the nanobeads/protein and has a negligible role in determining the magnitude of predicted shifts. The actual form of the temperature profile around the molecular is very complicate and may be modeled by an empirical parameter  $\epsilon$  [105]. With this parameter, we avoid the singularity of the temperature profile at the location of nanoparticle/molecule by combing the contribution of the temperature profile near the source into this parameter. In fact, the temperature profile should rise steadily until reaching some radius on the order of the molecular size. This approximation is justified, first, because the thermal transport process itself rapidly smooths nanoscale spatial variations created by molecular shape and, second, because the ensuing temperature field created by the molecular hot spot is long-range (*i.e.*,  $l/r$ ) dependence. Therefore, the tuning shift is only a weak function of the parameter  $\epsilon$ . Actually, instead of parameter  $\epsilon$ , the optical cross section  $\sigma$  is the major aspect that determine the magnitude of thermal-optic effect.

#### 8.4.2 Estimation of absorption cross section

To calculate the wavelength shift due to thermo-optic effect, we need to estimate or measure the absorption cross section of micro/nano-beads. In the case of an individual dielectric sphere suspended in a homogeneous medium, the light scattered and absorbed can be expressed with Mie's theory [117]

$$\sigma_s = \frac{\lambda_1^2}{2\pi} \sum_{n=1}^{\infty} (2n+1) (|a_n|^2 + |b_n|^2) \quad (8.18)$$

$$\sigma_a = \frac{\lambda_1^2}{2\pi} \sum_{n=1}^{\infty} (2n+1) \Im(a_n + b_n) \quad (8.19)$$

$\Im(z)$  gives the imaginary part of complex variable  $z$ ;  $a_n$  and  $b_n$  are complex and defined by

$$a_n = \frac{m\psi_n(mx)\psi'_n(x) - \psi_n(x)\psi'_n(mx)}{m\psi_n(mx)\zeta'_n(x) - \zeta_n(x)\psi'_n(mx)} \quad (8.20)$$

$$b_n = \frac{\psi_n(mx)\psi'_n(x) - m\psi_n(x)\psi'_n(mx)}{\psi_n(mx)\zeta'_n(x) - m\zeta_n(x)\psi'_n(mx)} \quad (8.21)$$

where  $m = n_1/n_m$ ,  $n_m$  and  $n_1$  are the refractive indices of the surrounding medium and the sphere, respectively;  $x = k_m r = \frac{2\pi r}{\lambda_m} = \frac{2\pi n_m r}{\lambda_0}$  and the *Riccati-Bessel functions* is given by

$$\psi_n(\rho) = \rho j_n(\rho), \quad \zeta_n(\rho) = \rho h_n^{(1)}(\rho) \quad (8.22)$$

where  $j_n(\rho)$  is the spherical Bessel function and  $h_n^{(1)}(\rho)$  is the spherical Hankel function of the first kind. In the small particle approximation, where  $r/\lambda_0 \ll 1$ , the Taylor expansion of spherical Bessel function leads to

$$a_1 = -\frac{i2x^3}{3} \frac{m^2 - 1}{m^2 + 2} + O(x^5) \quad (8.23)$$

$$b_1 = O(x^5), \quad a_2 = O(x^5) \quad (8.24)$$

The scattering and absorption cross section can be expressed as

$$\sigma_s = \frac{8\pi}{3} k_m^4 r^6 \left| \frac{n_1^2 - n_m^2}{n_1^2 + 2n_m^2} \right|^2 \quad (8.25)$$

$$\sigma_a = 4\pi k_m r^3 \Im \left| \frac{n_1^2 - n_m^2}{n_1^2 + 2n_m^2} \right| \quad (8.26)$$

where  $k_m$  is the wave number is surrounding medium. If the the particle and buffer are weakly dispersed, *i.e.*,  $\frac{n_1^2 - n_m^2}{n_1^2 + 2n_m^2}$  could be approximated as a constant over the wavelength of interest, then for sufficiently small particles, we have

$$\sigma_s \propto \frac{1}{\lambda_0^4}, \quad \sigma_a \propto \frac{1}{\lambda_0} \quad (8.27)$$

which signify the character of Rayleigh scattering. These expression could be obtained by treating the sphere as an ideal dipole with moment given by the electrostatics theory. Actually, the shape of the particle may not be relevant for this consideration; for an arbitrary particle the characteristic length would serve the same function as  $r$  here. We also noticed that the dependence of scattering and absorption cross section on the radius of beads are

$$\sigma_s \propto r^6, \quad \sigma_a \propto r^3 \quad (8.28)$$

At wavelength  $\lambda_0 = 680 \text{ nm}$ , the complex refractive index of polystyrene and water could be found in literatures [118]. The results are summarized in Tab. 8.3. Unfortunately, the

Substance	Real part of RI	Imaginary part of RI
Water	1.334	$2.4 \times 10^{-8}$
Polystyrene	1.579	$5 \times 10^{-4}$

Table 8.3: Complex refractive index (RI) of polystyrene and water at  $\lambda_0 = 680 \text{ nm}$ 

Radius (nm)	Absorption( $\sigma_a, \text{cm}^2$ )	Scattering( $\sigma_s, \text{cm}^2$ )	Total( $\sigma_t, \text{cm}^2$ )
12.5	$5.87 \times 10^{-16}$	$6.87 \times 10^{-17}$	$6.56 \times 10^{-16}$
25	$4.70 \times 10^{-15}$	$4.40 \times 10^{-15}$	$9.09 \times 10^{-15}$
50	$3.76 \times 10^{-14}$	$2.81 \times 10^{-13}$	$3.19 \times 10^{-13}$

Table 8.4: The scattering and absorption cross section of polystyrene beads suspended in water at  $\lambda_0 = 680 \text{ nm}$ .

imaginary part of refractive index of DPBS seems not available. The below calculations are based on the polystyrene beads suspended in water. The theoretical estimation are shown in Tab. 8.4.

To test the validity of this theory about thermo-optic shift, we propose an experiment of nanoparticle detection with high coupled power. In contrast to polystyrene beads, silica beads has negligible absorption cross sections, and we do not expect observable thermo-optic effect in the sensing experiment of silica beads. Here, we estimate thermo-optic shift induced by polystyrene (PS) and silica beads attaching to the surface of microtoroids (Tab. 8.5). In the calculation, we assume loaded Q factor of 100 million and coupled power of  $1 \mu\text{W}$ . The dimension of toroid is set to have major diameter  $85 \mu\text{m}$  and minor diameter  $15 \mu\text{m}$ . In this low-power regime, there is no distinguishable contribution of thermo-optic shift.

As a comparison, the estimated shift with 1 mW coupled power is summarized in

Material	Radius (nm)	Reactive shift (MHz)	Thermo-optic shift (MHz)	Total shift (MHz)
Polystyrene	12.5	0.3	0.005	0.3
Polystyrene	25	2.4	0.05	2.45
Silica	10	0.08	$7 \times 10^{-6}$	0.08
Silica	30	2.2	$1.9 \times 10^{-4}$	2.2

Table 8.5: The reactive and thermo-optic shift induced by polystyrene and silica beads attaching to the surface of microtoroids ( $\lambda_0 = 680 \text{ nm}$ ). In the calculation, we assume loaded Q factor of 100 million and coupled power of  $1 \mu\text{W}$ . The dimension of toroid is set to have major diameter  $85 \mu\text{m}$  and minor diameter  $15 \mu\text{m}$ .

Material	Radius (nm)	Reactive shift (MHz)	Thermo-optic shift (MHz)	Total shift (MHz)
Polystyrene	12.5	0.3	5.2	5.5
Polystyrene	25	2.4	46	48.4
Silica	10	0.08	0.007	0.09
Silica	30	2.2	0.19	2.4

Table 8.6: The reactive and thermo-optic shift induced by polystyrene and silica beads attaching to the surface of microtoroids ( $\lambda_0 = 680 \text{ nm}$ ). In the calculation, we assume loaded Q factor of 100 million and coupled power of 1 mW. The dimension of toroid is set to have major diameter  $85 \mu\text{m}$  and minor diameter  $15 \mu\text{m}$ .

Tab. 8.6. There would be significant increase in the induced shift for polystyrene beads but not for silica beads.

## 8.5 Summary

By employing a thermal-stabilized, reference interferometer to monitor wavelength shift in real time, we have achieved a record sensitivity for nanodetection using a microcavity biosensor. Sensing of  $12.5 \text{ nm}$  radius polystyrene nanobeads was demonstrated; shift distribution data were measured for detection of beads having three different diameters and agreed well with theory. Greatly enhanced SNR detection of individual InfA virion was also demonstrated. Although our detection experiment was based on a silica microtoroid platform, the reference-interferometer method can be readily applied to other platforms such as microsphere and microdisk sensors and requires no feedback control of the probe laser source. Further improvement of detection sensitivity is possible by adopting a feedback control loop to stabilize the probe laser. Finally, we note that a mechanism in which both path length and backscatter effects enhance step shift has been observed and is used to improve detection signal-to-noise. In the end, thermal-optic effect in nano/bio-sensing is theoretically investigated and discussed.

# Bibliography

- [1] B. Soller, D. Gifford, M. Wolfe, and M. Froggatt. High resolution optical frequency domain reflectometry for characterization of components and assemblies. *Opt. Express*, 13:666–674, 2005.
- [2] J. Bauters, M Heck, D John, J Barton, C Bruinink, A Leinse, R Heideman, D Blumenthal, and J Bowers. Planar waveguides with less than 0.1 dB/m propagation loss fabricated with wafer bonding. *Opt. Express*, 19:24090–24101, 2011.
- [3] H. Lee, T. Chen, J. Li, O. Painter, and K. Vahala. Ultra-low-loss optical delay line on a silicon chip. *Nature Communications*, 3:doi:10.1038/ncomms1876, 2012.
- [4] K. J. Vahala. Optical microcavities. *Nature*, 424:839–846, 2003.
- [5] T. J. Kippenberg, R. Holzwarth, and S. A. Diddams. Microresonator-based optical frequency combs. *Science*, 332:555–559, 2011.
- [6] F. Vollmer and S. Arnold. Whispering-gallery-mode biosensing: label-free detection down to single molecules. *Nature Method*, 5:591–596, 2008.
- [7] T. Lu, H. Lee, T. Chen, S. Herchak, J. H. Kim, S. E. Fraser, R. C. Flagan, and K. J. Vahala. High sensitivity nanoparticle detection using optical microcavities. *Proc. Natl. Acad. Sci. U.S.A.*, 108:5976–5979, 2011.
- [8] T Aoki, B Dayan, E Wilcut, W. P. Bowen, A. S. Parkins, T. J. Kippenberg, K. J. Vahala, and H. J Kimble. Observation of strong coupling between one atom and a monolithic microresonator. *Nature*, 442:671–674, 2006.
- [9] T. J. Kippenberg, J. Kalkman, A. Polman, and K. J. Vahala. Demonstration of an erbium-doped microdisk laser on a silicon chip. *Phys. Rev. A*, 74:051802, 2006.

- [10] D. K. Armani, T. J. Kippenberg, S. M. Spillane, and K. J. Vahala. Ultra-high-Q toroid microcavity on a chip. *Nature (London)*, 421:925–929, 2003.
- [11] V. Braginsky, M. Gorodetsky, and V. Ilchenko. Quality-factor and nonlinear properties of optical whispering-gallery modes. *Phys. Rev. A*, 137:7–8, 1989.
- [12] M. Gorodetsky, A. Savchenkov, and V. Ilchenko. Ultimate Q of optical microsphere resonators. *Opt. Express*, 21:453–455, 1996.
- [13] D. W. Vernooy, V. S. Ilchenko, H. Mabuchi, E. W. Streed, and H. J. Kimble. High-Q measurements of fused-silica microspheres in the near infrared. *Opt. Lett.*, 23:247–249, 1998.
- [14] C. Ciminelli, F. Dell’Olio, C. Campanella, and M. Armenise. Photonic technologies for angular velocity sensing. *Adv. Opt. Photon.*, 2:370–404, 2010.
- [15] R. Ulrich. Fiber-optic rotation sensing with low drift. *Opt. Express*, 5:173–175, 1980.
- [16] W. Chang, editor. *RF Photonic Technology in Optical Fiber Links*. Cambridge University Press, 2002.
- [17] C. Koos, P. Vorreau, T. Vallaitis, P. Dumon, W. Bogaerts, R. Baets, B. Esembeson, I. Biaggio, T. Michinobu, F. Diederich, W. Freude, and J. Leuthold. All-optical high-speed signal processing with silicon-organic hybrid slot waveguides. *Nature Photonics*, 3:216–219, 2009.
- [18] X. Yao and L. Maleki. Optoelectronic microwave oscillator. *J. Opt. Soc. Am. B*, 13:1725–1735, 1996.
- [19] J. K. Ranka, R. S. Windeler, and A. J. Stentz. Visible continuum generation in air-silica microstructure optical fibers with anomalous dispersion at 800 nm. *Opt. Lett.*, 25:25–27, 2000.
- [20] H. Dorren, M. Hill, Y. Liu, N. Calabretta, F. Srivatsa, Huijskens, H. de Waardt, and G. Khoe. Optical packet switching and buffering by using all-optical signal processing methods. *J. Lightw. Technol.*, 21:2–13, 2003.

- [21] R. Adar, M. Serbin, and V. Mizrahi. Less than 1 dB per meter propagation loss of silica waveguides measured using a ring resonator. *J. Lightw. Technol.*, 12:1369–1372, 1994.
- [22] J. F. Bauters, M. Heck, D. John, D. Dai, M. Tien, J. S. Barton, A. Leinse, R. G. Heideman, D. J. Blumenthal, and J. E. Bowers. Ultra-low-loss high-aspect-ratio Si<sub>3</sub>N<sub>4</sub> waveguides. *Opt. Express*, 19:3163–3174, 2011.
- [23] K. Takada, H. Yamada, Y. Hida, Y. Ohmori, and S. Mitachi. Rayleigh backscattering measurement of 10 m long silica-based waveguides. *Electronic Letters*, 32:1665–1667, 1996.
- [24] T. Chen, H. Lee, and K. J. Vahala. Thermal stress in silica-on-silicon disk resonators. *Appl. Phys. Lett.*, 102:031113, 2013.
- [25] T. Chen, H. Lee, J. Li, and K. J. Vahala. A general design algorithm for low optical loss adiabatic connections in waveguides. *Opt. Express*, 20:22819–22829, 2012.
- [26] H. Lee, T. Chen, J. Li, O. Painter, and K. Vahala. Chemically etched ultrahigh-Q wedge-resonator on a silicon chip. *Nature Photonics*, 6:369–373, 2012.
- [27] M. Oxborrow. Traceable 2D finite-element simulation of the whispering-gallery modes of axisymmetric electromagnetic resonators. *IEEE Trans. Microw. Theory Tech*, 55:1209–1218, 2007.
- [28] T. Carmon, L. Yang, and K. J. Vahala. Dynamical thermal behavior and thermal self-stability of microcavities. *Opt. Express*, 12:4742–4750, 2004.
- [29] C. Ciminelli, V. Passaro, F. Dell’Olio, and M. Armenise. Three-dimensional modelling of scattering loss in InGaAsP/InP and silica-on-silicon bent waveguides. *J. Eur. Opt. Soc. Rapid Publ.*, 4:1–6, 2009.
- [30] T. Barwicz and H. Haus. Three-dimensional analysis of scattering losses due to side-wall roughness in microphotonic waveguides. *J. Lightw. Technol.*, 23:2719–2732, 2005.
- [31] M. Borselli, T. J. Johnson, and O. Painter. Beyond the Rayleigh scattering limit in high-Q silicon microdisks: theory and experiment. *Opt. Express*, 13:1515–1530, 2005.

- [32] F. Payne and J. Lacey. A theoretical analysis of scattering loss from planar optical waveguides. *Opt. Quantum. Electron.*, 26:977–986, 1994.
- [33] A. Ashkin and J. M. Dziedzic. Observation of resonances in radiation pressure on dielectric spheres. *Phys. Rev. Lett.*, 38:1351–1354, 1977.
- [34] M. Gorodetsky, A. Pryamikov, and V. Ilchenko. Rayleigh scattering in high-Q microspheres. *J. Opt. Soc. Am. B*, 17:1051–1057, 2000.
- [35] M. Cai, O. Painter, and K. J. Vahala. Observation of critical coupling in a fiber taper to silica-microsphere whispering gallery mode system. *Phys. Rev. Lett.*, 85:1430–1432, 2000.
- [36] H. Rokhsari and K. J. Vahala. Ultralow loss, high Q, four port resonant couplers for quantum optics and photonics. *Phys. Rev. Lett.*, 92:253905, 2004.
- [37] J. Laine, B. Little, D. Lim, H. Tapalian, L. Kimerling, and H. Haus. Microsphere resonator mode characterization by pedestal anti-resonant reflecting waveguide coupler. *IEEE Phot. Tech. Lett.*, 12:1004–1006, 2000.
- [38] M. L. Gorodetsky and V. S. Ilchenko. Optical microsphere resonators: optical coupling to high-Q whispering-gallery modes. *J. Opt. Soc. Am. B*, 16(1):147–154, 1999.
- [39] D. R. Rowland and J. D. Love. Evanescent wave coupling of whispering gallery modes of a dielectric cylinder. *Proc. Inst. Electr. Eng. Part J.*, 140:177–188, 1993.
- [40] N. J. Hoff. Buckling at high temperature. *Journal of the Royal Aeronautical Society*, 61:756–774, 1957.
- [41] E. I. Grigolyuk and L. A. Magerramova. Stability of circular homogeneous and inhomogeneous plates. *Izv An SSSR. Mekhanika Tverdogo Tela*, 16:111–138, 1981.
- [42] T. R. Tauchert. Thermally induced flexure, buckling, and vibration of plates. *Appl. Mech. Rev.*, 44:347–360, 1991.
- [43] L. Starman, J. Busbee, J. Reber, J. Lott, W. Cowan, and N. Vandelli. Stress measurement in MEMS devices. *Nanotech*, 1:398–401, 2001.

- [44] W. Spengen. MEMS reliability from a failure mechanisms perspective. *Microelectronics Reliability*, 43:1049–1060, 2003.
- [45] S. Spillane, T. Kippenberg, O. Painter, and K. Vahala. Ideality in a fiber-taper-coupled microresonator system for application to cavity quantum electrodynamics. *Phys. Rev. Lett.*, 91:043902, 2003.
- [46] S. M. Spillane, T. J. Kippenberg, O. J. Painter, and K. J. Vahala. Ideality in a fiber-taper-coupled microresonator system for application to cavity quantum electrodynamics. *Phys. Rev. Lett.*, 91:043902, 2003.
- [47] S. P. Timoshenko and J. Gere. *Theory of Elastic Stability*. McGraw-Hill Book Company, 1961.
- [48] E. H. Mansfield. On the buckling of an annular plate. *J. Mech. and Applied Math.*, 13:16–23, 1960.
- [49] K. K. Raju and G. V. Rao. Thermal post-buckling of circular plates. *Computers & Structures*, 18:1179–1182, 1984.
- [50] T. X. Yu and W. Johnson. The buckling of annular plates in relation to the deep-drawing process. *Int. J. Mech. Sci.*, 24:175–188, 1982.
- [51] C. Y. Wang. On the buckling of a circular plate on an elastic foundation. *Journal of Applied Mechanics*, 72:795–796, 2005.
- [52] T. Tang, C. Y. Hui, H. G. Retsos, and E. J. Kramer. Characterization of a fracture specimen for crack growth in epoxy due to thermal fatigue. *Engineering Fracture Mechanics*, 72:791–805, 2005.
- [53] I. S. Grudinin, A. B. Matsko, and L. Maleki. On the fundamental limits of Q factor of crystalline dielectric resonators. *Opt. Express*, 15:3390–3395, 2007.
- [54] I. S. Grudinin, V. S. Ilchenko, and L. Maleki. Ultrahigh optical Q factors of crystalline resonators in the linear regime. *Phys. Rev. A*, 74:063806, 2006.
- [55] A. A. Savchenkov, A. B. Matsko, V. S. Ilchenko, and L. Maleki. Optical resonators with ten million finesse. *Opt. Express*, 15:6768–6773, 2007.

- [56] P. E. Barclay, K. Srinivasan, O. Painter, B. Lev, and H. Mabuchi. Integration of fiber coupled high-Q  $\sin_x$  microdisks with atom chips. *Appl. Phys. Lett.*, 89:131108, 2006.
- [57] M. Tomes and T. Carmon. Photonic micro-electromechanical systems vibrating at X-band (11 GHz) rates. *Phys. Rev. Lett.*, 102:113601, 2009.
- [58] I. S. Grudinin, N. Yu, and L. Maleki. Brillouin lasing with a  $\text{CaF}_2$  whispering gallery mode resonator. *Phys. Rev. Lett.*, 102:043902, 2009.
- [59] R. Pant, E. Li, D. Y. Choi, C. G. Poulton, S. J. Madden, B. Luther-Davies, and B. J. Eggleton. Cavity enhanced stimulated Brillouin scattering in an optical chip for multiorder Stokes generation. *Opt. Lett.*, 36:3687–3689, 2011.
- [60] S. P. Smith, F. Zarinetchi, and S. Ezekiel. Narrow-linewidth stimulated Brillouin fiber laser and applications. *Opt. Lett.*, 16:393–395, 1991.
- [61] Y. Okawachi, M. Bigelow, J. Sharping, Z. Zhu, A. Schweinsberg, D. Gauthier, R. Boyd, and A. Gaeta. Tunable all-optical delays via Brillouin slow light in an optical fiber. *Phys. Rev. Lett.*, 94:153902, 2005.
- [62] Z. Zhu, A. Dawes, D. Gauthier, L. Zhang, and A. Willner. Broadband SBS slow light in an optical fiber. *J. Lightw. Technol.*, 25:201–206, 2007.
- [63] Z. Zhu, D. Gauthier, and R. Boyd. Stored light in an optical fiber via stimulated Brillouin scattering. *Science*, 318:1748–1750, 2007.
- [64] T.W. Hänsch and B. Couillaud. Laser frequency stabilization by polarization spectroscopy of a reflecting reference cavity. *Opt. Commun.*, 35:441–444, 1980.
- [65] A. Schliesser, R. Riviere, G. Anetsberger, O. Arcizet, and T. J. Kippenberg. Resolved-sideband cooling of a micromechanical oscillator. *Nature Physics*, 4:415–419, 2008.
- [66] R. W. Tkach, A. R. Chraplyvy, and R. M. Derosier. Spontaneous Brillouin scattering for single-mode optical-fibre characterisation. *Electron. Lett.*, 22:1011–1013, 1986.
- [67] P. Del’Haye, O. Arcizet, A. Schliesser, R. Holzwarth, and T. J. Kippenberg. Full stabilization of a microresonator frequency comb. *Phys. Rev. Lett.*, 101:053903, 2008.

- [68] T. J. Kippenberg, S. M. Spillane, and K. J. Vahala. Kerr-nonlinearity optical parametric oscillation in an ultrahigh-Q toroid microcavity. *Phys. Rev. Lett.*, 93:083904, 2004.
- [69] A. B. Matsko, A. A. Savchenkov, N. Yu, and L. Maleki. Whispering-gallery-mode resonators as frequency references. I. fundamental limitations. *J. Opt. Soc. Am. B*, 24:1324–1335, 2007.
- [70] A. A. Savchenkov, A. B. Matsko, V. S. Ilchenko, N. Yu, and L. Maleki. Whispering-gallery-mode resonators as frequency references. II. stabilization. *J. Opt. Soc. Am. B*, 24:2988–2997, 2007.
- [71] M. L. Gorodetsky and I. S. Grudinin. Fundamental thermal fluctuations in microspheres. *J. Opt. Soc. Am. B*, 21:697–705, 2004.
- [72] T. J. Kippenberg and K. J. Vahala. Cavity optomechanics: Back-action at the mesoscale. *Science*, 321:1172–1176, 2008.
- [73] T. J. Kippenberg and K. J. Vahala. Cavity opto-mechanics. *Opt. Express*, 15(25):17172–17205, 2007.
- [74] G. Anetsberger, A. Riviere. R., Schliesser, O. Arcizet, and J. Kippenberg, T. Ultralow-dissipation optomechanical resonators on a chip. *Nature Photonics*, 2:627 – 633, 2011.
- [75] M. C. Tien, J. F. Bauters, M. Heck, D. Spencer, D. Blumenthal, and J. E. Bowers. Ultra-high quality factor planar  $\text{Si}_3\text{N}_4$  ring resonators on Si substrates. *Opt. Express*, 19:13551–13556, 2011.
- [76] A. Maker and A. M. Armani. Low loss silica on silicon waveguides. *Opt. Lett.*, 36:3729–3731, 2011.
- [77] F Tosco, editor. *Fiber Optic Communication Handbook*. Tab Professional & Reference, 1990.
- [78] M. C. Tien, J. F. Bauters, M. J. R. Heck, D. T. Spencer, R. G. Heideman, D. J. Blumenthal, and J. E. Bowers. Ultra-high quality factor planar  $\text{Si}_3\text{N}_4$  ring resonators on Si substrates. *Opt. Express*, 19:13551–13556, 2011.

- [79] T Kominato, Y Hida, M Itoh, H Takahashi, S. Sohma, T Kitoh, and Y Hibino. Extremely low-loss (0.3 dB/m) and long silica-based waveguides with large width and clothoid curve connection. *In Proceedings of ECOC*, Stockholm, Sweden, 2004.
- [80] D. Liang, A. W. Fang, H. Park, T. E. Reynolds, K. Warner, D. C. Oakley, and J. E. Bowers. Low-temperature, strong SiO<sub>2</sub>-SiO<sub>2</sub> covalent wafer bonding for III-V compound semiconductors-to-silicon photonic integrated circuits. *J. Electron. Mater.*, 37:1552–1559, 2008.
- [81] F. P. Kapron, D. B. Keck, and R. D. Maurer. Radiation losses in glass optical waveguides. *Appl. Phys. Lett.*, 17:423–425, 1970.
- [82] G. P. Agrawal. *Nonlinear Fiber Optics*. Academic Press, 1995.
- [83] R. H. Stolen and C. Lin. Self-phase-modulation in silica optical fibers. *Phys. Rev. A*, 17:1448–1453, 1978.
- [84] F. Ladouceur and P. Labeye. A new general approach to optical waveguide path design. *J. Lightw. Technol.*, 13:481–491, 1995.
- [85] J. F. Bauters, M. Heck, D. D. John, J. S. Barton, C. M. Bruinink, A. Leinse, R. Heide-man, D. J. Blumenthal, and J. E. Bowers. Planar waveguides with less than 0.1dB/m propagation loss fabricated with wafer bonding. *Opt. Express*, 19:24090–24101, 2011.
- [86] E. Marcatilli. Bends in optical dielectric guides. *Bell Syst. Tech. J.*, page 2103, 1969.
- [87] R. Baets and P. Lagasse. Loss calculation and design of arbitrarily curved integrated-optic waveguides. *J. Opt. Soc. Am.*, 73:177–182, 1983.
- [88] V. Subramaniam, G. De Brabander, D. Naghski, and J. Boyd. Measurement of mode field profiles and bending and transition losses in curved optical channel waveguides. *J. Lightw. Technol.*, 15:990–997, 1997.
- [89] W. Gambling, H. Matsumura, and C. Ragdale. Field deformation in a curved single-mode fiber. *Electron. Lett.*, 14:130–132, 1978.
- [90] T. Kitoh, N. Takato, M. Yasu, and M. Kawachi. Bending loss reduction in silica-based waveguide by using lateral offsets. *J. Lightw. Technol.*, 13:555–562, 1995.

- [91] A. Melloni, P. Monguzzi, R. Costa, and M. Martinelli. Design of curved waveguide: the matched bend. *J. Opt. Soc. Am. A*, 20:130–137, 2003.
- [92] T. Kominato, Y. Hida, M. Itoh, H. Takahashi, S. Sohma, T. Kitoh, and Y. Hibino. Extremely low-loss (0.3 dB/m) and long silica-based waveguides with large width and clothoid curve connection. *In Proceedings of ECOC*, page TuI.4.3, 2004.
- [93] D. Meek and J. Harris. Clothoid spline transition spirals. *Mathematics of Computation*, 59:117–133, 1992.
- [94] D. J. Walton. Spiral spline curves for highway design. *Microcomputers in Civil Engineering*, 4:99–106, 1989.
- [95] K. G. Bass. The use of clothoid templates in highway design. *Transportation Forum*, 1:47–52, 1984.
- [96] S. Fleury, P. Soueres, J. P. Laumond, and R. Chatila. Primitives for smoothing mobile robot trajectories. *IEEE Transactions on Robotics and Automation*, 11:441–448, 1995.
- [97] J. McCrae and K. Singh. Sketching piecewise clothoid curves. *Computers & Graphics*, 33:452–461, 2008.
- [98] K. Takada, H. Yamada, Y. Hida, Y. Ohmori, and S. Mitachi. New waveguide fabrication techniques for next-generation plcs. *NTT Technical Review*, 3, 2005.
- [99] A. W. Snyder. Radiation losses due to variations of radius on dielectric or optical fibers. *IEEE Trans. Microwave Theory Tech.*, 18:608–615, 1970.
- [100] A. W. Snyder. Excitation and scattering of modes on a dielectric or optical fiber. *IEEE Trans. Microwave Theory Tech.*, 17:1138–1144, 1969.
- [101] M. Heiblum and J. Harris. Analysis of curved optical waveguides by conformal transformation. *IEEE J. Quantum Electron.*, 11:75–83, 1975.
- [102] R. L. Levien. *From Spiral to Spline: Optimal Techniques in Interactive Curve Design*. PhD thesis, UC Berkeley, 2009.
- [103] S. Ohlin. *Splines for engineers*. Eurographics Association, 1987.

- [104] X. Fan, I. M. White, S. Shopova, H. Zhu, J. Suter, and Y. Sun. Sensitive optical biosensors for unlabeled targets: A review. *Analytica Chimica Acta*, 620:8–26, 2008.
- [105] A. M. Armani, R. P. Kulkarni, S. E. Fraser, R. C. Flagan, and K. J. Vahala. Label-free, single-molecule detection with optical microcavities. *Science*, 317:783–787, 2007.
- [106] S. Arnold, M. Khoshshima, I. Teraoka, S. Holler, and F. Vollmer. Shift of whispering-gallery mode in microspheres by protein absorption. *Opt. Lett.*, 28:272–274, 2003.
- [107] S. M. Nie and S. R. Emery. Probing single molecules and single nanoparticles by surface enhanced Raman scattering. *Science*, 275:1102–1106, 1997.
- [108] D. Monzon-Hernandez, V. P. Minkovich, M. P. Villatoro, J. Kreuzer, and G. Badenes. Photonic crystal fiber microtaper supporting two selective higher-order modes with high sensitivity to gas molecules. *Appl. Phys. Lett.*, 93:081106, 2008.
- [109] A. Naik, M. Hanay, Hiebert W., X. Feng, and M Roukes. Towards single-molecule nanomechanical mass spectrometry. *Nature Nanotechnology*, 4:445–450, 2009.
- [110] R. Macovez, M. Mariano, S. Finizio, and J. Martorell. Measurement of the dispersion of air and of refractive index anomalies by wavelength-dependent nonlinear interferometry. *Opt. Express*, 17:13881–13888, 2009.
- [111] F. Vollmer, D. Braun, A. Libchaber, M. Khoshshima, I. Teraoka, and S. Arnold. Protein detection by optical shift of a resonant microcavity. *Opt. Express*, 80:4057–4059, 2002.
- [112] F. Vollmer, S. Arnold, and D. Keng. Single virus detection from the reactive shift of a whispering-gallery mode. *Proc. Natl. Acad. Sci. U.S.A.*, 105:20701–20704, 2008.
- [113] S. Arnold, R. Ramjit, D. Keng, V. Kolchenko, and I. Teraoka. Microparticle photo-physics illuminates viral bio-sensing. *Faraday Discuss.*, 137:65–83, 2008.
- [114] R. Lamb and R. Krug. *Fundamental Virology*. Lippincott Williams & Wilkins, Philadelphia, 2001.
- [115] C. Reimer, R. Baker, T. Newlin, and M. Havens. Influenza virus purification with the zonal ultracentrifuge. *Science*, 3:1379–1381, 1966.

- [116] S. Arnold, S. I. Shopova, and S. Holler. Whispering gallery mode bio-sensor for label-free detection of single molecules: thermo-optic vs. reactive mechanism. *Opt. Express*, 18:281–287, 2010.
- [117] C. F. Bohren. *Absorption and scattering of light by small particles*. New York : John Wiley & Sons, 2003.
- [118] X. Ma, J. Lu, R. Brock, Jacobs. K., P. Yang, and X. Hu. Determination of complex refractive index of polystyrene microspheres from 370 to 1610 nm. *Physics in Medicine and Biology*, 48:4165–4172, 2010.